

Department of Physics
Indian Institute of Technology Guwahati
Ph.D. Thesis



Interaction and disorder effects on topology in one-dimensional lattices

Ashirbad Padhan

Thesis Supervisor: **Prof. Kanhaiya Pandey**
External Supervisor: **Dr. Tapan Mishra**
February, 2024



Interaction and disorder effects on topology in one-dimensional lattices

A

Thesis Submitted

in Fulfillment of the Requirements

for the Degree of

PhD

By

ASHIRBAD PADHAN

Under the Supervision of

Prof. KANHAIYA PANDEY and Dr. TAPAN MISHRA



Department of Physics

Indian Institute of Technology Guwahati

February, 2024



Declaration

This is to certify that the thesis entitled “**Interaction and disorder effects on topology in one-dimensional lattices**”, submitted by me to the *Indian Institute of Technology Guwahati*, for the award of the degree of PhD, is a bonafide work carried out by me under the supervision of Prof. Kanhaiya Pandey and Dr. Tapan Mishra. The content of this thesis, in full or in parts, have not been submitted to any other University or Institute for the award of any degree or diploma. I also wish to state that to the best of my knowledge and understanding nothing in this report amounts to plagiarism.

Signed: _____

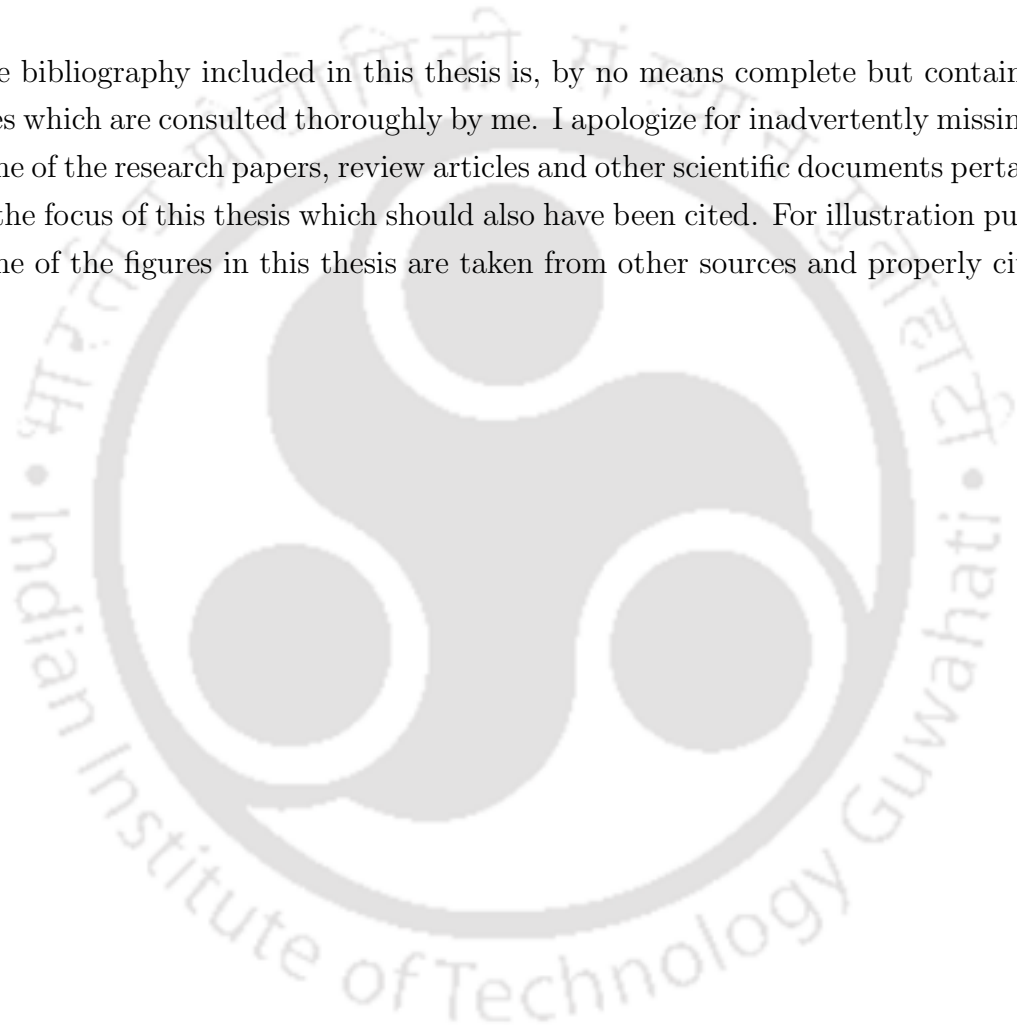
Ashirbad Padhan
Department of Physics,
Indian Institute of Technology Guwahati,
Guwahati-781039, Assam, India.

Date: _____



Disclaimer

The bibliography included in this thesis is, by no means complete but contains the ones which are consulted thoroughly by me. I apologize for inadvertently missing out some of the research papers, review articles and other scientific documents pertaining to the focus of this thesis which should also have been cited. For illustration purpose some of the figures in this thesis are taken from other sources and properly cited.





Certificate

This is to certify that the thesis entitled “**Interaction and disorder effects on topology in one-dimensional lattices**”, submitted by Ashirbad Padhan (196121004), a research scholar in the *Department of Physics, Indian Institute of Technology Guwahati*, for the award of the degree of PhD, is a record of an original research work carried out by him under my supervision and guidance. The thesis has fulfilled all requirements as per the regulations of the institute and in my opinion has reached the standard needed for submission. The results embodied in this thesis have not been submitted to any other University or Institute for the award of any degree or diploma.

Signed: _____

Supervisor: Prof. Kanhaiya Pandey
External Supervisor: Dr. Tapan Mishra
Department of Physics,
Indian Institute of Technology Guwahati,
Guwahati-781039, Assam, India.

Date: _____



Dedicated to my family...





Acknowledgement

As a kid when I came across the life story of John Logie Baird through an Odia text book, I immediately envisioned to jump into the field of research. Until 10th standard my journey as an upcoming researcher went well. However, my interest shifted towards technology from science as soon as I touched a Samsung mobile. I was curious to understand the operating system deeply and created a deep interest in tech gadgets like smartphones, cameras and PCs etc. My interest got inclined towards science again when I could understand a few important concepts of Quantum Mechanics during my BSc. It was 2018 when my MSc project instructor, Dr. Ashok Kumar, introduced me to the 2016 Nobel prize awarded topic, the concept of “topological insulators”. After completing a moderately successful project on the same, I was confident enough to build my career out of research. Then I never looked back and joined as a PhD scholar at IIT Guwahati under the supervision of Prof. Tapan Mishra in 2019.

“Understanding a theory and actually proposing one; using a ready made gadget and actually creating one from scratch” - the two things that kept me hooked since the beginning of my PhD. There were joyful moments when I felt nothing can be better than research, and there were miserable situations when I cursed myself for choosing this career. However, I was able to withstand all the perturbations, and now I have successfully completed my PhD with handful of publications and adequate skill sets. To fight with all the odds and to face all kinds of circumstances, several people came in my life either as saviours or mentors. Although all of them deserve a fair share of credit for this thesis, here I would like to mention a few of them, without whom it was almost impossible to complete the same.

First and foremost, I express my deepest gratitude towards my former supervisor (who later became my co-supervisor), Dr. Tapan Mishra. I still remember those initial days of my PhD when I was in severe dilemma to choose a supervisor as per my research interests and abilities; he was the one who cleared all the confusions within just a few minutes of one-to-one discussion. The way he explained the concepts of

“ultracold atoms in optical lattices”, and numerical methods like “exact diagonalization” and “DMRG”, I right away decided to join his research group. Gradually, as I was able to learn coding, numerical methods and many-body physics, I realized that this is exactly what I was looking for my research journey. Moreover, when Prof. Mishra asked me to learn the DMRG method and implement the same to study topology in interacting systems, I felt elated since the topic exactly aligned with my research interest. Because of him only I could develop enough coding skills and learn various concepts in physics which I could not do so before joining PhD. Although I still need to learn many things, currently I feel confident enough to compete with my peers and contemporaries, something which I never imagined before joining under him. Apart from all the help regarding research, he has always been a supporter in all kinds of situations. I feel really blessed to not only have a competent supervisor like him, but also to have him found as one of my family members. All in all, I am not just a student of Prof. Mishra, rather a true fanboy of his dedication in work, his charming personality and his kind nature.

Words are inadequate in offering my thanks to Prof. Kanhaiya Pandey, who became my supervisor after Prof. Mishra resigned from IITG and joined NISER Bhubaneswar. Although I did not have a chance to work on research problems with him, I can never forget the support he provided during the last one and half year of my PhD. I was really worried about how things would go after Prof. Mishra left, but he made everything so smooth and easy for me. Initially, when he used to be the chairman of my doctoral committee, he provided valuable suggestions to improve my knowledge in physics as well as my presentation skills. He will always remain as a special person in my life.

I would also like to share my gratitude towards the HoDs, Prof. Subhradip Ghosh and Prof. Perumal Algarswamy, the doctoral committee members - Prof. Pankaj Kumar Mishra, Prof. Amarendra Kumar Sarma and Prof. Aditya Narayan Panda for their involved participation during my presentations and for their kind suggestions to improve my research methodology.

Also, a special thanks to Prof. Saurabh Basu, Prof. Pankaj Kumar Mishra and Prof. Padmakumar Padmanabhan for their instructions during the course work which turned out to be really helpful throughout my PhD.

I want to thank my collaborator Prof. Smitha Vishveshwara for her suggestions and motivation during the one project which I worked with her. I would also like to acknowledge with much appreciation her support for my presentation at the prestigious APS March Meeting.

I wish to express my gratitude towards my group members Dr. Suman Mondal, Dr. Sayan Lahiri, Dr. Mrinal Kanti Giri, Soumya Ranjan Padhi, Rajashri Parida and Biwajit Paul for maintaining a friendly and productive environment in the group; my friends from IITG, especially Sunil Moharana and Alok Sahu, my juniors Himanshu Murari and Sanu Gangwar for all the emotional and moral support during my PhD career. Apart from the pandemic period, I never visited my home in several years but these guys made the campus feel more than just a work place for me.

My warm thanks to all the teaching and non-teaching staff at IITG for the help in academic and non-academic activities. I would also like to acknowledge the people from NISER Bhubaneswar and ICTS Bangalore for all the support during my academic visits there.

I would like to thank everyone who has always motivated me to reach the stage where I am right now (be it my teachers, my elders, my friends or my juniors). A special mention goes to a brother-cum-friend from my village, Akash Khamari, who stood by me to tackle every odd situations.

Finally, I owe my deepest gratitude to my family members for their constant support even after leading such miserable lives themselves. This thesis, or rather everything I achieve, is completely dedicated to them. With these means, I make a promise that unlike the unsolicited and terrible past, the future would be unimaginably delightful. And yes, the doctoral degree is the turning point!

February, 2024

Ashirbad Padhan



Abstract

The topological phases and phase transitions in condensed matter is subject of great interest in the field of condensed matter physics. Starting from the first observation of the quantum Hall effect in two dimensional electron systems, study of topological phases has attracted a great deal of attention in the last several decades. Topological phases are characterised by gapped bulk spectrum and gapless or localized edge states, non-local correlations and well defined topological invariants. A class of topological phases which is known as the symmetry protected topological phases where the bulk-boundary correspondence is protected by some underlying symmetries. In general the topological character is robust to perturbation although strong perturbation such as interaction and disorder breaks down the topological nature. However, in certain cases, these perturbations can drive a topological phase transition or may induce a topological character in the system. Due to the rapid progress in the field of quantum simulations of such systems in artificial experimental setups and their relevance as effective models to some of the real materials, these systems are explored in various different contexts. Motivated by this development, we focus on the study of interaction and disorder effects on the topological character of low dimensional lattice systems in this thesis.

The content of the thesis is two-fold. In the first half we discuss the interaction mediated topological phases and transition in low dimensional lattices. In the second part we discuss the effect of quasiperiodic disorder in the system. First, we propose that in a one dimensional lattice of spinless fermions, a dimerized nearest neighbour interaction can stabilise a well-defined topological phase transition even though the system is a gapless liquid in the non-interacting limit. We then show that in a system of two-component spinless fermions, the topological character in one of the components can be induced by the density dependent hopping of the other component. We then study the topological properties of bosons on a two-leg ladder coupled by inter-leg hopping and interaction. By considering two different types of dimerizations on the legs, we have shown how interaction can mediate

topological phase transitions in the many-body system. In the rest of the thesis we discuss the effect of quasiperiodic disorder on a one dimensional lattice. Before studying the effect of quasiperiodic disorder on the topological phases, we study the localization properties as a function of disorder. In this context, we obtain an interesting re-entrant localization transition in the presence of quasiperiodic disorder and a staggered local potential. Subsequently, we study the effect of disorder on the topological properties of the system. In this context we propose a model where we have shown that a well defined topological phase transition can be established as a function of disorder and we quantify this behaviour in the context of Thouless charge pumping. All the studies in the thesis are performed using numerical methods such as the exact diagonalization and the density matrix renormalization group (DMRG) methods.



List of Publications

Publications included in the thesis

1. **Ashirbad Padhan**, Mrinal Kanti Giri, Suman Mondal and Tapan Mishra, *Emergence of multiple localization transitions in a one-dimensional quasiperiodic lattice*, Phys. Rev. B **105**, L220201 (2022).
2. Suman Mondal, **Ashirbad Padhan** and Tapan Mishra, *Realizing a symmetry protected topological phase through dimerized interactions*, Phys. Rev. B **106**, L201106 (2022).
3. **Ashirbad Padhan**, Suman Mondal, Smitha Vishveshwara and Tapan Mishra, *Interacting bosons on a Su-Schrieffer-Heeger ladder: Topological phases and Thouless pumping*, Phys. Rev. B **109**, 085120 (2024).
4. **Ashirbad Padhan** and Tapan Mishra, *Disorder driven Thouless charge pump in a quasiperiodic lattice*, Under review, arXiv:2312.16568.

Publications outside thesis

5. **Ashirbad Padhan**, Rajashri Parida, Sayan Lahiri, Mrinal Kanti Giri and Tapan Mishra, *Quantum phases of constrained bosons on a two-leg Bose-Hubbard ladder*, Phys. Rev. A **108**, 013316 (2023).
6. **Ashirbad Padhan**, Soumya Ranjan Padhi and Tapan Mishra, *Complete delocalization and reentrant topological transition in a non-Hermitian quasiperiodic lattice*, Phys. Rev. B **109**, L020203 (2024).

Schools/Workshops/Conferences attended

1. Presented online poster at *Young Investigators Meet on Quantum Condensed Matter Theory*, organised by NISER Bhubaneswar, India, November 2021.
2. Presented online poster at *QMAT*, organised by TIFR Mumbai, India, December 2021.
3. Delivered online talk at *QMAT*, organised by TIFR Mumbai, India, December 2021.
4. Delivered online talk at *Research and Industrial Conclave*, organised by IIT Guwahati, January 2022.
5. Delivered online talk at *March Meeting*, organised by American Physical Society, March 2023.
6. Attended *Physics of Quantum Matter School*, organised by NISER Bhubaneswar, India, June 2023.

Contents

List of publications	xv
1 Introduction	1
1.1 Quantum phase transitions (QPT)	1
1.1.1 Description of QPT	2
1.1.2 Quantum versus classical phase transitions	4
1.2 Topology in condensed matter physics	4
1.3 Topological phase transitions	6
1.3.1 The Su-Schrieffer-Heeger (SSH) model	7
1.4 Effect of interaction on topology	11
1.5 Localization transition	15
1.5.1 Anderson localization	16
1.5.2 Scaling theory of localization	16
1.5.3 Aubry-André model	18
1.6 Effect of disorder on topology	23
1.6.1 Effect of hopping disorder	23
1.6.2 Effect of onsite disorder	24
1.7 Chapterwise outline of the thesis	26
2 Numerical methods	29
2.1 Exact Diagonalization (ED)	29
2.1.1 Lanczos algorithm	30
2.2 Matrix product states (MPS)	32
2.2.1 Singular value decomposition	33
2.2.2 Canonical form	33
2.2.3 Matrix product operator (MPO)	36
2.3 Density matrix renormalization group (DMRG)	37

3	Symmetry protected topological phase through dimerized interactions	41
3.1	Introduction	41
3.2	Model and approach	42
3.3	Results	43
3.3.1	Phase diagram	43
3.3.2	Topological character	45
3.3.3	Experimental realization	48
3.4	Topological phase transition induced via density dependent hopping .	50
3.5	Conclusions	54
4	Interacting bosons on a Su-Schrieffer-Heeger ladder	55
4.1	Introduction	55
4.2	Model and approach	57
4.3	Results	58
4.3.1	Many-body phases	60
4.3.1.1	Uniform dimerization	60
4.3.1.2	Staggered dimerization	64
4.4	Conclusions	74
5	Multiple localization transitions in a quasiperiodic lattice	77
5.1	Introduction	77
5.2	Model and approach	78
5.3	Results	78
5.3.1	Multiple localization transitions	79
5.3.2	Expansion dynamics	83
5.3.3	Experimental scheme	85
5.4	Conclusions	87
6	Disorder driven topological phase transition	89
6.1	Introduction	89
6.2	Model and approach	90
6.3	Results	91
6.4	Disorder driven Thouless charge pumping (dTCP)	94
6.5	Localization properties	98
6.6	Conclusions	100

7 Conclusions and Future Directions	101
7.1 Future Directions	102
Bibliography	105





List of Figures

1.1	Low energy eigenvalues E of the Hamiltonian $H(g)$ for a finite size system. (a) shows a proper level-crossing and (b) shows an avoided level-crossing at $g = g_c$	2
1.2	Phase diagram in the $g - T$ plane near a quantum phase transition. The shaded region is where classical theory of phase transition can be applied and quantum description is required in the region enclosed by the dashed lines.	3
1.3	Deformation of a coffee cup into a doughnut which shows the topological equivalence between the two.	5
1.4	The upper panel shows a double-well lattice potential representing the SSH model with staggered hopping amplitudes (t_1 and t_2). The lower panel shows the same in terms of lattice sites. Here A and B denote the two sublattice sites of a unit cell.	8
1.5	(a), (b) and (c) show the band structure for $t_1 < t_2$, $t_1 = t_2$ and $t_1 > t_2$, respectively, and (d), (e) and (f) show the variation of $\mathbf{h}(k)$ in the $h_x - h_y$ plane for $t_1 < t_2$, $t_1 = t_2$ and $t_1 > t_2$, respectively. (g) shows the winding number ν in the $t_1 - t_2$ plane.	9
1.6	Figure (a) shows the single-particle energy spectrum of the model (1.9) as a function of t_1 with fixed $t_2 = 1$ for $L = 40$. Figure (b) shows the wave amplitude of the two states marked by red circle and black plus in (a). Figure (c) shows the wave amplitude of the two states marked by red square and black cross in (a).	10
1.7	Phase diagram of the model 1.17 as a function of t_2 in the non-interacting limit ($U = V = 0$) for fixed $t_1 = 1$. Here the bosons are considered to be of hardcore in nature. The figure is taken from [1].	12
1.8	Phase diagram of the model 1.17 with hardcore bosons as a function of V for fixed $t_1 = 1$ and $t_2 = 0.2$. The figure is taken from [2].	13

LIST OF FIGURES

1.9 Phase diagram of the model 1.17 in the $U/t_{1,2} - t_1/t_2, t_2/t_1$ plane for $V = 0$. Here three-body constrained bosons at unit filling ($\rho = 1$) are considered. The figure is taken from [3]. 14

1.10 Phase diagram of the model 1.17 in the $U - V$ plane for vanishing dimerization ($t_1 = t_2 = t$). Here the maximum number of bosons per site is considered to be two. The figure is taken from [4]. 15

1.11 Scaling theory of localization which shows the variation of the scaling function for $d = 1, 2$ and 3-dimensions. Here the yellow dot marks the critical point g_c corresponding to $d = 3$ 18

1.12 The figure shows a main lattice, a disorder lattice and the quasiperiodically disordered lattice resulting from the two. 19

1.13 The IPR as a function of eigenstate index and disorder strength λ in the (a) real space and (b) momentum space. 20

1.14 (a) shows $\langle \text{IPR} \rangle$ and $\langle \text{NPR} \rangle$ as a function of disorder strength λ . (b-d) show the probability density $|\psi_i|^2$ of the ground state with respect to lattice sites i for $\lambda = 1, 2$ and 3, respectively. 21

1.15 Energy spectrum as a function of β for (a) $\lambda = 1$, (b) $\lambda = 2$ and (c) $\lambda = 3$ 22

1.16 (a) shows $\langle \text{IPR} \rangle$ and $\langle \text{NPR} \rangle$ as a function of disorder potential depth V_d . (b) shows the IPR values as a function of energy eigenvalues and V_d . The shaded yellow area in (a) denotes the intermediate phase. This figure is taken from [5]. 23

1.17 (a) Shows the single-particle energy spectrum as a function of hopping disorder strength W for $L = 40$ sites for fixed $t_1 = 0.2$ and $t_2 = 1$. (b) shows the wave amplitudes for the states marked by the red circle and black plus in (a). (c) shows the wave amplitudes for the states marked by the red square and black cross in (a). 24

1.18 (a) Shows the single-particle energy spectrum as a function of onsite disorder strength W for $L = 40$ sites for fixed $t_1 = 0.2$ and $t_2 = 1$. (b) shows the wave amplitudes for the states marked by the red circle and black plus in (a). (c) shows the wave amplitudes for the states marked by the red square and black cross in (a). 25

2.1	Top row from left to right shows the coefficient of the wavefunction of a two-site lattice, A matrix in the left end, A matrix in the bulk and A matrix in the right end of the lattice of L sites. The middle figure represents an L -index coefficient tensor and the bottom figure shows the matrix product representation.	34
2.2	The iterative construction of a matrix product state from an arbitrary state is represented graphically.	35
2.3	The top figure shows a singular matrix corresponding to l th lattice site. An MPS in mixed-canonical form is shown in the bottom figure.	35
2.4	The top row from left shows the W matrices for the left end, bulk and the right end. The bottom figure shows the graphical representation of a matrix product operator.	36
2.5	The graphical representation of the DMRG method using MPS formalism. Here (a-d) represent the infinite DMRG algorithm and (e-l) represent the finite DMRG algorithm. The arrow sign shows the direction of the sweeping process.	38
3.1	(a) The phase diagram of model (3.1) in $V_1 - V_2$ plane. The red dashed (blue dotted) line represents the gapless SF (gapped CDW) phase at $V_1 = V_2$. The SF-CDW critical point is marked by the solid red square. The black solid circles represents the boundary between the BO and the CDW phases. The arrow directions in (a) show the pumping protocols. Here θ in BO_θ is the associated Berry phase. (b) and (c) show the extrapolated gap at $V_1 = 1.0$ and 3.5 respectively with varying V_2 . The thin dotted line in (c) marks the BO-CDW transition point.	43
3.2	(a) and (b) show the behavior of $S_{BO}(\pi)$ (black circles) and $S(\pi)$ (red squares) with varying V_2 for cuts through $V_1 = 1.0$ and 3.5 respectively in the phase diagram. (c) The finite-size scaling of $S(\pi)$ is shown for different values of L at $V_1 = 3.5$ with varying V_2 . The crossing of the curves for different L at a point represents the BO-CDW transition. (d) Scaled $S(\pi)$ is plotted against the scaled V_2 showing the collapse of all points onto a single curve and thus confirming $V_2^c = 3.09$ as the transition point.	46

3.3	(a) Onsite particle densities $\langle n_i \rangle$ vs i are plotted in the BO_0 (black circle) and BO_π (red squares) phases. (b) The Berry phase γ/π for different lengths $L = 8, 10, 12$ obtained using the ED method is plotted as a function of V_2 across the topological phase transition at $V_1 = 1.0$. (c) O_{str} vs V_2 for $V_1 = 1.0$ are plotted for $L = 500$ (red squares) and $L = 200$ (black plus) where the effective topological phase transition is valid. (d) The extrapolated values of Δ (black circles) and O_{str} for $L = 400$ are plotted as a function of V_2 for $V_1 = 3.0$. The finite (vanishing) values of O_{str} (Δ) after $V_2 = 3.3$ indicate a transition to the BO_π phase.	47
3.4	(a) Shows the evolution of polarization following a pumping cycle across three different critical points such as $V_c = 0.5$ (black circles), 1.0 (red squares) and $V_c = 5.0$ (blue diamonds) of the phase diagram in Fig. 3.1 obtained using the DMRG simulations. The density correlation matrix Γ obtained using the ED method is plotted for $L = 16$ sites in (b) for the BO_0 phase ($V_1 = 10.0, V_2 = 1.0$) and in (c) for the BO_π phase ($V_1 = 1.0, V_2 = 10.0$).	49
3.5	Single and two particle excitation energy gap for both the components as a function of Δ_\uparrow	51
3.6	CDW and BO structure factors for both the components as a function of Δ_\uparrow	52
3.7	Onsite density and bond energy, respectively, for $\Delta_\uparrow = -1.0$ in (a) and (c) and $\Delta_\uparrow = 1.0$ in (b) and (d).	53
4.1	Two-leg ladder with different hopping dimerization patterns: (a) the uniform dimerization pattern, and (b) the staggered dimerization pattern. t_a, t_b and t_p are the hoppings along the leg-a, leg-b and along the rungs of the ladder. α_a and α_b decide the dimerization along leg-a and leg-b respectively. The circles represent the sites, and the thick (thin) bonds along the legs represent the strong (weak) hopping strengths. The dashed vertical lines illustrate the rung hopping. We allow inter-particle interaction V only along the rungs which is marked by the arrow.	56

- 4.2 The single particle energy spectrum of a system of 40 sites ($L = 20$) with varying t_p for (a) uniform dimerization pattern ($t_a = t_b = 0.6t_1$ and $\alpha_a = \alpha_b = 0.4t_1$) and (b) staggered dimerization pattern ($t_a = t_b = 0.6t_1$ and $\alpha_a = -\alpha_b = 0.4t_1$) along the legs. (c) and (d) show the on-site probability $|\psi_j|^2$ of states marked by the red plus signs in (a) and (b) respectively. Note that, the on-site probability for all the states marked in (a) are identical as that of in (c). This clearly indicates that the edge states are crossing the band from one gapped phase to another. 58
- 4.3 Phase diagram of Model(5.1) with $V = 0$, $t_a = t_b = 0.6t_1$ and $\alpha_a = \alpha_b = 0.4t_1$ plotted in the t_p - μ plane. The solid black lines show the phase boundaries of gapped phases, such as the plaquette order (PO), the bond order (BO), and the rung-Mott insulator (RMI) phases. The dashed red lines denote the mid-gap states. The gapless superfluid (SF) phase is represented by the grey shaded area. 61
- 4.4 The figure displays the bulk and edge densities of the system represented by ρ_b and ρ_e respectively as a function of μ . (a), (b) and (c) show the ρ_b (solid lines) and ρ_e (dashed lines) with varying chemical potential μ for $t_p = 0.2t_1$, $0.75t_1$ and $1.5t_1$, respectively, corresponding to three cuts in the phase diagram shown in Fig 4.3. This shows the nature of the bulk phases (gapped or gapless) when the edge states are being filled in different parameter regimes. 62

4.5 The figure shows the bond energies (B_j) of all the bonds defined in Eq. 4.5 and the onsite particle number ($\langle n_j \rangle$) for different phases corresponding to Fig. 4.3 with a system consisting of 40 sites ($L = 20$ rungs). In the figures, the thickness of a bond is proportional to the respective strength of B_j , and the face colour of the circles represents the values of $\langle n_j \rangle$. This captures different dimerization patterns and the existence of edge states in different phases. (a) shows B_j and $\langle n_j \rangle$ corresponding to the bond order (BO) phase at 1/2-filling ($N = L$) for $t_p = 0.2t_1$, which has two filled edge states (localized at each edge). The parameters in (b) are the same as (a) but with $N = L + 1$, which has three occupied edge states (two localized on the left edge and one on the right edge). (c) and (d) show the same quantities for $t_p = 0.2t_1$, $0.75t_1$ and $1.5t_1$ respectively at 1/2-filling ($N = L$). The change in bond order pattern can be seen going from the bond order (BO) (a) to the rung-Mott insulator (RMI) (d) phase. (e) and (f) correspond to the 1/4-filling plaquette order (PO) phases for parameters $t_p = 0.5t_1$ with $N = L/2 - 1$ and $t_p = 1.5t_1$ with $N = L/2$, respectively. The edge state appears (localized on the left edge) in (f). Note that in all the cases, we have used a small onsite potential of $-0.001t_1$ in one edge to break the degeneracy of the edge-state pair. 64

4.6 Phase diagram of Model(5.1) with $V = 0$, $t_a = t_b = 0.6t_1$ and $\alpha_a = -\alpha_b = 0.4t_1$ is plotted in t_p - μ plane. The solid black lines show the phase boundaries of gapped phases and the dashed lines denote the mid-gap states. The gapless superfluid (SF) phase is represented by the shaded grey area. A topological phase transition happens through a gap-closing point for $\rho = 1/2$ from a non-trivial bond order (BO) to a trivial rung-Mott insulator (RMI) phase. 65

- 4.7 The figure shows the bond energy (B_j) of all the bonds defined in Eq. 4.5 and the onsite particle number ($\langle n_j \rangle$) for different phases of a system consisting of 40 sites ($L = 20$). (a) and (b) represent two gapped phases at the 1/2-filling ($N = L$), which are topological bond order (BO) and trivial rung-Mott insulator (RMI) phases corresponding to the parameter value $t_p = 0.25t_1$ and $1.5t_1$ respectively in Fig. 4.6. Here the thickness of a bond is proportional to the corresponding value of B_j , and the face color of the circles represents the onsite particle number. We can see the change in dimerization pattern between (a), which also has an occupied edge state (localized at the left edge), and (b). Note that in both cases, we have used a small onsite potential of $-0.001t_1$ in one edge to break the degeneracy of the edge-state pair. 66
- 4.8 Phase diagram of Model(5.1) with $t_a = t_b = 0.6t_1$, $\alpha_a = -\alpha_b = 0.4t_1$ and $t_p = 0.2t_1$ is plotted in V - μ plane. The solid black lines show the phase boundaries of gapped phases and the red dashed lines stand for the mid-gap edge states. The gapless superfluid (SF) phase is represented by the shaded grey area. Here, at $\rho = 1/2$, the topological phase transition occurs from a non-trivial bond order (BO) to a trivial rung-Mott insulator (RMI) phase through a gap-closing point with increasing V 67
- 4.9 Bond energies along the legs ($B_{a,b}$) and along the rung (B_r) computed by averaging over all the respective bonds for 240 sites ($L = 120$) at $\rho = 1/2$. (a), (b) and (c) represent the bond energies for $V = 0.0t_1, 1.5t_1$ and $-1.5t_1$, respectively, with varying t_p . The B_r dominates over $B_{a,b}$ after different t_p values for different values of V , implying the onset of a trivial RMI phase with different critical transition points. The green dotted lines in all the plots mark the critical point corresponding to $V = 0.0t_1$ in Fig. 4.6. 68

- 4.10 Phase diagrams of Model(5.1) with (a) $V = 1.5t_1$ and (b) $V = -1.5t_1$ are plotted in t_p - μ plane. The solid black lines show the phase boundaries of the gapped topological bond order (BO) phase, and trivial rung-Mott insulator (RMI) phases. The dashed lines stand for the mid-gap edge states. The gapless superfluid (SF) phase is represented by the shaded grey area. The green dotted line marks the critical point corresponding to $V = 0.0t_1$ in Fig. 4.6. The change in the gapless critical points for finite interaction can be seen by comparing to the non-interacting case at half-filling. 69
- 4.11 (a) Phase diagram at $\rho = 1/2$ corresponding to the Hamiltonian given in Eq. 5.1 for $t_a = t_b = 0.6t_1$ and $\alpha_a = -\alpha_b = 0.4t_1$ (staggered dimerization). Here the topological (trivial) phase is the BO (RMI) phase. The figure shows how the critical point changes with the interaction strength V . (b) Berry phase under twisted phase boundary conditions showing the topological phase transition as a function of t_p/t_1 for $V = 0.0t_1, 1.5t_1$ and $-1.5t_1$ on a system of length $L = 6$ (12 lattice sites). The dotted lines mark the transition points extracted from the phase diagram in (a) corresponding to each V 71
- 4.12 (a) Pictorial representation of the adiabatic variation of parameters are shown for three different pumping cycles with three different origins (t_o 's). The topological phase transition critical point t_p^c is marked with a green circle on the δ -axis. (b) The evolution of the polarization ($P(\tau)$) is plotted for three different t_o 's corresponding to three different pumping cycles shown in (a) for $V = 0$. Here $t_p^c \sim 0.87t_1$. Here only cycle-2, which encloses the t_p^c , shows robust pumping. (c) The evolution of $P(\tau)$ is shown for the same parameters corresponding to cycle-1 and 3 that are considered in (b), but with finite interaction strength $V = 1.5t_1$ and $V = -1.5t_1$ respectively. Unlike the non-interacting case, here a quantized amount of charge is being pumped. We call this phenomenon as the interaction-induced topological charge pumping. Here, for all the cases we consider $\Delta = 0.5t_1$ and a finite system of $L = 200$ rungs. 73

- 5.1 (a) The phase diagram in the $\Delta - \lambda$ plane obtained using the values of η for a system of size $L = 17711$. (b) IPR of all the eigenstates as a function of energies and λ for $\Delta = 1.8$ and a system size of $L = 17711$. (c) Extrapolated values of $\langle \text{IPR} \rangle$ (dashed red), $\langle \text{NPR} \rangle$ (dashed blue) with system sizes $L = 2584, 4181, 6765, 10946, 17711$, $\langle S \rangle / \ln(L)$ (solid green) for $L = 17711$ and $\langle r \rangle$ (dot-dashed black) for $L = 2584$ are plotted as a function of Δ for $\lambda = 1.5$ showing the multiple localization transitions. The $\langle r \rangle$ is computed using PBC with $\beta = 1597/2584$ and an average over 5000 phase offsets ϕ are considered. The intermediate phases are indicated by the grey shaded regions. (d) IPR of all the eigenstates as a function of state index and λ for $\Delta = 1.8$ and $L = 17711$. The white dashed line in (a) indicates the AA critical point at $\lambda = 2$ 80
- 5.2 Even-odd δ^{e-o} (red) and odd-even δ^{o-e} (blue) for $\lambda = 0.75$ and different values of Δ . For (a) $\Delta = 0.0$, (b) $\Delta = 0.9$ and (c) $\Delta = 3.0$ the system lies in the extended, intermediate and localized phase respectively. The results are obtained for a system of size $L = 28657$ and $\beta = 17711/28657$ under PBC. 81
- 5.3 The density distribution during the time evolution of an initial state for different values of Δ (a-h) at a fixed $\lambda = 1.5$ and $L = 2584$ with an average over 500 different values of phase offset ϕ . Only central 201 sites are shown for clarity. 82
- 5.4 (a) $\sigma(t)$ vs t (b) $P_{r=40}(t)$ vs t for $\Delta = 0.0, 0.45, 0.75, 1.05, 1.5, 1.8, 2.0$ and $\lambda = 1.5$. (c) $P_r(t = 10^5(1/J))$ as a function of r/L shows the multiple localization transition (see text). (d) The time evolved values of σ (red dashed) and $P_{r=40}$ (blue solid) to $t = 10^5(1/J)$ are plotted as a function of Δ for $\lambda = 1.5$. The shaded regions indicate the intermediate phases. For all the cases a system size of $L = 4181$ is considered. 84
- 5.5 Scheme for initial state preparation for the experimental observation of the multiple localization transitions. Deep (light) blue regions are the deep (shallow) lattice sites and the green spheres indicate the atoms. Δ denotes the onsite staggered potential. 86
- 5.6 The phase diagram in the $\Delta - \lambda$ plane obtained using the values of η for a system of size $L = 610$ 87

LIST OF FIGURES

5.7 (a) IPR as a function of eigenstate index and Δ , (b) $\langle \text{IPR} \rangle$ (red solid line) and $\langle \text{NPR} \rangle$ (blue dashed line) as a function of Δ for $\lambda = 0.1$ with system size $L = 2584$ showing a sharp localization transitions. 88

6.1 The figure depicts the model given in Eq. 6.1 in terms of lattice sites, hopping strengths t_1 and t_2 , staggered onsite potential strength Δ and the quasiperiodic disorder strength λ . The sublattice sites in a unit cell are denoted by A and B 91

6.2 Phase diagram in the $\alpha_1 - \lambda$ plane as a function of (a) G and (b) P . (c) shows the energy spectrum, and (d) shows the polarization P and local Chern marker C_{LCM} as a function of λ for a cut through $\alpha_1 = 0.4$. The two red dashed lines in (c) denote the variation of edge states under open boundary conditions. The green, orange and red shaded areas in (d) mark the topological, trivial and gapless phases, respectively. Here the system size is considered to be $L = 400$ for C_{LCM} and $L = 2584$ for other parameters. We set $\Delta = 0$ in all the cases. 92

6.3 (a) shows the pumping scheme in the $\Delta - \delta$ plane corresponding to three different pumping cycles. Here $(\lambda_0, 0)$ is the origin of the cycle and λ_c is the gap closing critical point. (b) shows the variation of local Chern marker C_{LCM} as a function of δ_0 for $\alpha_1 = 0.4, \Delta_0 = 0.5$ and $\lambda_0 = 1.4$. (c) and (d) show the energy spectrum as a function of τ/π for $\delta_0 = 0.5$ and 1.2 , respectively. 95

6.4 Polarization as a function of the pumping parameter τ for (a) $\lambda_0 = 0.5$ and (b) $\lambda_0 = 1.2$. The corresponding entanglement spectra using Eq. 6.8. are shown in (c) and (d), respectively. 97

6.5 Phase diagram in the $\alpha_1 - \lambda$ plane as a function of η . The inset shows a zoomed in portion of the phase diagram. 99

6.6 $\langle \text{IPR} \rangle$, $\langle \text{IPR} \rangle$ and $\langle S \rangle / \ln L$ as function are shown for $\alpha_1 = 0.4$ in (a) and $\alpha_1 = 25$ in (b). The corresponding IPR values are plotted as function of λ and eigenstate index in (c) and (d), respectively. The orange shaded areas in (a) and (b) denote the intermediate phases. 100

Chapter 1

Introduction

1.1 Quantum phase transitions (QPT)

Phase transitions are natural phenomena which occur when a tuning parameter is varied in the system. Due to this variation, the system experiences a change in its characteristics and the system is driven from one phase of matter to another. A familiar example of phase transition is the case of ice melting into water with increase in temperature, where the thermal fluctuation (in other words, the temperature) destroys the crystal structure of ice. This is because, below zero temperature the water molecules are closely bound together to form ice. However, when the temperature is above zero, the molecules can move almost freely as the bonding between the molecules is weakened. All such transitions which occur due to thermal fluctuation are commonly known as classical phase transitions.

According to the modern classification scheme, the phase transitions are divided into first order and second order phase transitions. First order phase transitions involve latent heat. During such transitions the system either releases or absorbs an amount of energy and the temperature remains constant on the addition of heat. Here the energy cannot be transferred instantaneously from the system to the environment or vice versa. For example, when water is heated it does not directly turn into gas, rather a mixture of water and vapour bubbles exist simultaneously. On the other hand, second order phase transitions, also known as continuous phase transitions, do not involve any latent heat. Such transitions are characterized by the divergence of susceptibility, infinite correlation lengths and power-law decay behaviour at the critical point. The diverging nature of these quantities are usually described by some critical exponents. Moreover, the Landau theory of phase transition is useful to study the second order phase transitions. According to this

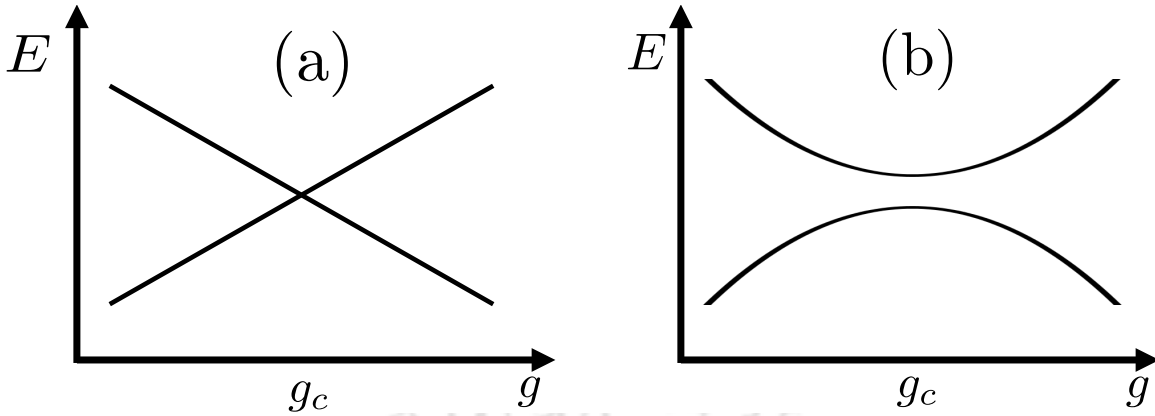


Figure 1.1: Low energy eigenvalues E of the Hamiltonian $H(g)$ for a finite size system. (a) shows a proper level-crossing and (b) shows an avoided level-crossing at $g = g_c$.

theory the order before and after the critical point can be characterized by an order parameter, which is involved in a spontaneous symmetry breaking of the system. Ferromagnetic transition, superconducting transition and superfluid transition are a few examples of second order phase transitions.

Quantum phase transition (QPT) is a transition between phases of matter driven by quantum fluctuation [6]. Unlike classical phase transition, where it is driven by thermal fluctuation, QPT plays its role when a system approaches to zero temperature. At this temperature the effect of thermal fluctuation is suppressed and quantum mechanical effects become more relevant. Often there are attractive or repulsive interactions in a system and their interplay with quantum statistics of the particles and strong correlation result in QPTs.

1.1.1 Description of QPT

Consider the Hamiltonian $H(g)$ of a lattice system with a dimensionless coupling parameter g . For finite system sizes, the corresponding ground state energy is usually a smooth and analytic function of g . However, when g couples only to a conserved quantity (i.e., $H(g) = H_0 + gH_1$ where H_0 and H_1 commute), it is not the case. This means that the simultaneous eigenfunctions of H_0 and H_1 are independent of g even though the eigenvalues depend on g . This leads to a level crossing at a non-analytic point $g = g_c$ where an excited level becomes the ground state (Fig. 1.1 (a)).

On the other hand, an avoided level-crossing between the ground and an excited state for a finite system could become progressively sharper with increasing system size, which leads to a non-analyticity at $g = g_c$ at the infinite size limit (Fig. 1.1 (b)).

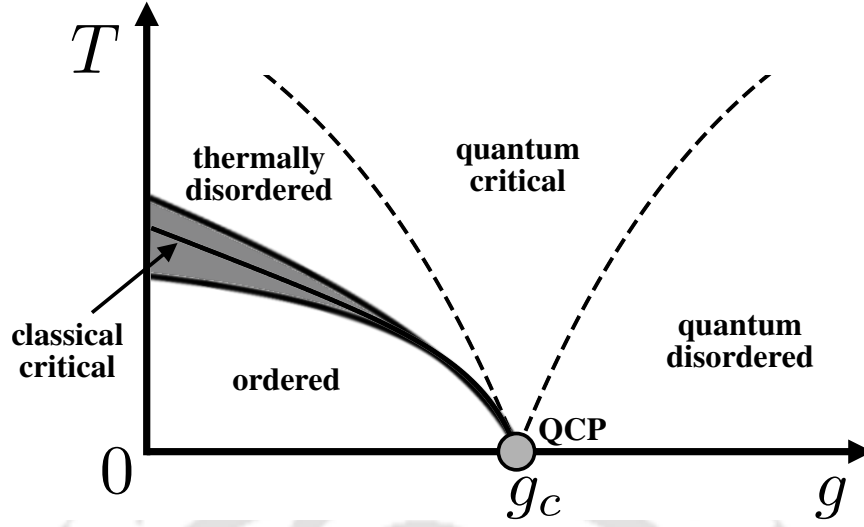


Figure 1.2: Phase diagram in the $g - T$ plane near a quantum phase transition. The shaded region is where classical theory of phase transition can be applied and quantum description is required in the region enclosed by the dashed lines.

Such a point of non-analyticity can be identified as a quantum phase transition point. The non-analyticity could be either the limiting case of an avoided level crossing, or a proper level crossing between the lowest two states.

Now let us focus on second order quantum phase transitions, at which the characteristic energy scale of fluctuations above the ground state vanishes as g approaches g_c . Let D be the energy scale for some significant spectral density of fluctuations at zero temperature ($T = 0$) for $g \rightarrow g_c$. Thus, D could be the gap of the first excited state from the ground state and in most cases, as g approaches g_c , D vanishes as

$$D \sim J|g - g_c|^{z\nu}, \quad (1.1)$$

where J is the energy scale of a characteristic microscopic coupling, ν is a critical exponent and z is a dynamical critical exponent. Additionally, the characteristic length scale ξ also diverges as

$$\xi^{-1} \sim L|g - g_c|^\nu, \quad (1.2)$$

where L denotes an inverse length scale of order the inverse lattice spacing. From the above two equations D and ξ can be related as

$$D \sim \xi^{-z}. \quad (1.3)$$

1.1.2 Quantum versus classical phase transitions

Moving away from the quantum critical point at $g = g_c$ and $T = 0$ can be helpful in understanding and describing the thermodynamic and dynamic properties of numerous systems with different values of $|g - g_c|$ and temperature T . In Fig. 1.2, the thermodynamic singularity is present only at $T = 0$, and above this the $T > 0$ properties are analytic as a function of g near $g = g_c$. The solid line inside the shaded area is the line of finite temperature second order phase transitions, at which the thermodynamic free energy is not analytic. Near such a line, the typical frequency ω_{typ} at which the important long distance degrees of freedom fluctuate is

$$\hbar\omega_{typ} \ll k_B T, \quad (1.4)$$

where k_B is the Boltzmann constant. Under these conditions, a purely classical description can be applied to these important degrees of freedom and it works in the shaded region of Fig. 1.2. Consequently, the theory of second order phase transitions in classical systems describes the ultimate critical singularity along the line of $T > 0$ phase transitions. However, the $T > 0$ region near the quantum critical point g_c (enclosed by the dashed lines in Fig. 1.2) describes an interplay between both quantum and thermal fluctuations.

1.2 Topology in condensed matter physics

Topology is a branch of Mathematics that deals with the different classes of geometries of objects. All the geometries of an object will remain invariant if we deform the object without tearing or gluing it. For example, a coffee cup and doughnut are topologically equivalent since the number of holes in both of them is one and they can be smoothly deformed into each other as shown in Fig. 1.3. However, a coffee cup and a football cannot be placed in the same topological class as per the above argument.

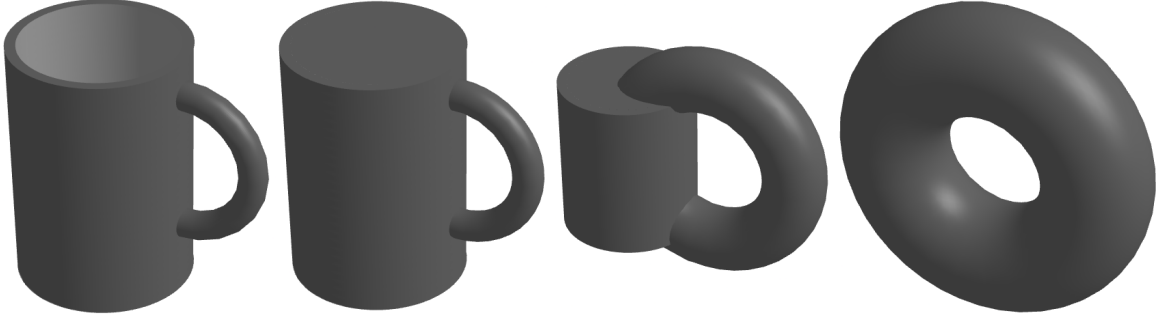


Figure 1.3: Deformation of a coffee cup into a doughnut which shows the topological equivalence between the two.

This analogy in geometry can be quantified by the Gauss-Bonnet theorem in Mathematics which is given by the formula

$$\frac{1}{4\pi} \int_M \kappa dA = (1 - g), \quad (1.5)$$

where κ is the Gaussian curvature of the system under consideration, M . The theorem states that the integration of the Gaussian curvature of an object with its surface, multiplied by $\frac{1}{4\pi}$, will result in $(1 - g)$, where g is the genus or number of holes in the object M . The right side of the equation remains invariant during the deformation of the object because even if the surface changes locally, the integration of the curvature onto the changed surface remains invariant. Therefore, the number ‘ g ’ can be coined as a topological invariant as it remains unchanged throughout the deformation. Similar features can be seen in a new class of insulators, known as topological insulators, where an associated quantity remains invariant under adiabatic change of system parameters.

As described in the previous section, phases of matter can be described by the Landau paradigm based on spontaneous symmetry breaking. An ordered phase appears when the system moves to low temperature regime with one of the symmetries (present at high temperature) getting broken. However, after the discovery of the integer quantum Hall effect, it was realized that an ordered state can appear without breaking any kind of symmetry [7]. If we place a 2D electron gas under strong magnetic field, plateaus can be observed for the Hall conductance, σ_{xy} , with respect to the magnetic field. These plateaus are quantized with the values $n \left(\frac{e^2}{h} \right)$ and can have accuracy up to 10^{-9} ! Such quantizations are results of topological order.

In condensed matter physics, the quantum Hall effect and topological insulators can be connected with the concept of topology, where the Brillouin zone plays the role of the surface and the Berry phase plays the role of the curvature [8]. The Berry

phase is defined as a geometric phase which is acquired by the eigenstate when the system goes through a cyclic change adiabatically. It results from the geometrical properties of the parameter space of the system (for example, the crystal momentum space in crystalline solid). The change in electron wave function ($\Psi(\mathbf{r})$) in the unit cell gives rise to a Berry connection (A) and a Berry curvature (F). The integral of F results in the invariant n , which appears in Hall conductivity. This is known as the first Chern number. The relations between the mentioned parameters can be formulated as

$$\Psi(\mathbf{r}) = e^{i\mathbf{k}\cdot\mathbf{r}} u_k(\mathbf{r}), \quad (1.6)$$

$$A = \langle u_k | -i\nabla_k | u_k \rangle, \quad (1.7)$$

and

$$\mathbf{F} = \nabla \times \mathbf{A}, \quad (1.8)$$

where $|u_k\rangle$ is a Bloch state.

In integer quantum Hall effect, the Landau levels are either filled or empty. This makes them behave like ordinary band insulators with a bulk band gap. However, there is finite conductivity in the Hall plateaus! The reason is the existence of conducting edge states in the system which form the border of the 2D sample. In the likes of quantum spin Hall effect, these conducting edges are known to be chiral, i.e., they act as one-way conductance channel and these states are topologically protected.

1.3 Topological phase transitions

Symmetry protected topological (SPT) phase transition is a new class of QPT that does not belong to the Landau-Ginzburg paradigm associated with the spontaneous symmetry breaking. Under the continuous change of the system parameter, where the energy gap of the system remains finite and the symmetry of the system is preserved, the topological invariant remains unchanged [9]. In such a scenario, if a phase transition to a topologically different phase happens, it happens through a gap closing.

Since the discovery of QH insulators, over the past few decades, the field of topological insulators has flourished rapidly, both experimentally and theoretically [9]. Several materials compounds are found to be topological insulator in one- two- and

three-dimensions in recent years. Besides real materials, much progress has happened in recent years to observe topological phases in artificial systems like the systems of ultracold atoms in optical lattices by generating artificial magnetic fields and spin-orbit coupling in neutral atoms, leading to the characterization and realization of topological Bloch bands. In the following we discuss the topological phase transition in one of the simplest models which has been experimentally realized in artificial systems.

1.3.1 The Su-Schrieffer-Heeger (SSH) model

The connection between the ideas of topology and topological invariant with Condensed Matter Physics can be established by considering a toy model known as the Su-Schrieffer-Heeger (SSH) model [10–12]. This particular model was first used to describe the polyacetylene $((\text{CH})_n)$ molecule which consists of CH-monomers with alternate single- and double-bonds between C and H atoms. In the context of condensed matter the SSH model describes spinless (or spin-polarized) fermions hopping from one site to another with staggered hopping amplitudes in a one-dimensional lattice of two-site unit cells. A diagrammatic representation of the model in terms of a double-well periodic potential and in terms of lattice sites is shown in the upper and lower panel of Fig. 1.4, respectively. The model Hamiltonian of the system reads as

$$H_{SSH} = -t_1 \sum_j (a_j^\dagger b_j + H.c.) - t_2 \sum_j (a_j^\dagger b_{j-1} + H.c.) \quad (1.9)$$

where $a_j^\dagger (b_j^\dagger)$ is the creation operator at A(B) sublattice site of the j -th unit cell. While t_1 denotes the intra-cell hopping amplitude t_2 fixes the inter-cell hopping amplitude. The model becomes dimerized when we set $t_1 \neq t_2$.

In order to examine the bulk properties of the SSH model we first extract the dispersion relation by plugging in periodic boundary conditions. Since the system is translationally invariant we can Fourier transform the real space Hamiltonian into the momentum space Hamiltonian given by

$$H = \sum_k |k\rangle H(k) \langle k|. \quad (1.10)$$

Here, $|k\rangle$ is a quasi-momentum state and $H(k)$ is the Bloch Hamiltonian which can be expressed in matrix form as

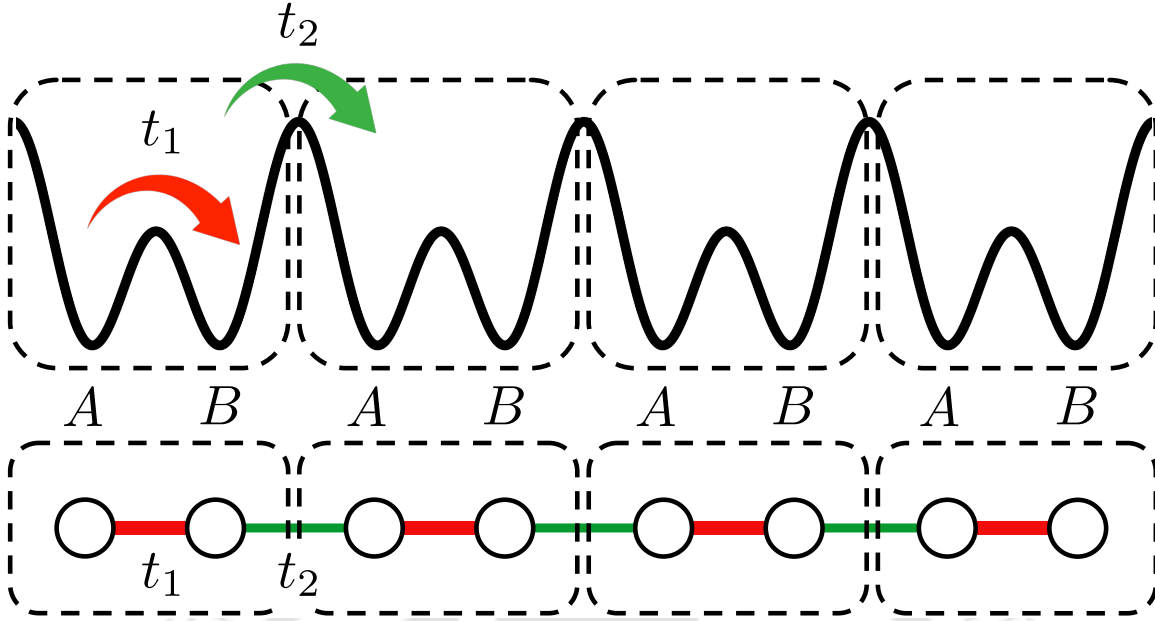


Figure 1.4: The upper panel shows a double-well lattice potential representing the SSH model with staggered hopping amplitudes (t_1 and t_2). The lower panel shows the same in terms of lattice sites. Here A and B denote the two sublattice sites of a unit cell.

$$H(k) = \begin{pmatrix} 0 & t_1 + e^{ik}t_2 \\ t_1 + e^{-ik}t_2 & 0 \end{pmatrix}. \quad (1.11)$$

The full Hamiltonian is now block diagonalized into N such 2×2 band Hamiltonians corresponding to each k . Now the dispersion relation can be obtained as

$$E(k) = \pm \sqrt{t_1^2 + t_2^2 + 2t_1t_2 \cos(k)} \quad (1.12)$$

and the eigenvectors corresponding to the two eigenvalues are

$$|\pm(k)\rangle = \begin{pmatrix} \pm e^{-i\phi(k)} \\ 1 \end{pmatrix}, \quad (1.13)$$

where $\phi = \tan^{-1} \left(\frac{t_2 \sin(k)}{t_1 + t_2 \cos(k)} \right)$.

The band structure of the system for different values of t_1 and t_2 using Eq. 1.12 is shown in Fig. 1.5. The figure shows that there exists a gap when $t_1 \neq t_2$. However, there is band touching at the Brillouin zone boundary, for the $t_1 = t_2$ case. Therefore, this phase can be considered as metallic whereas the phases corresponding to finite dimerization can be regarded as insulating.

At first glance, it seems that both the limits of $t_1 \neq t_2$ share a similar band

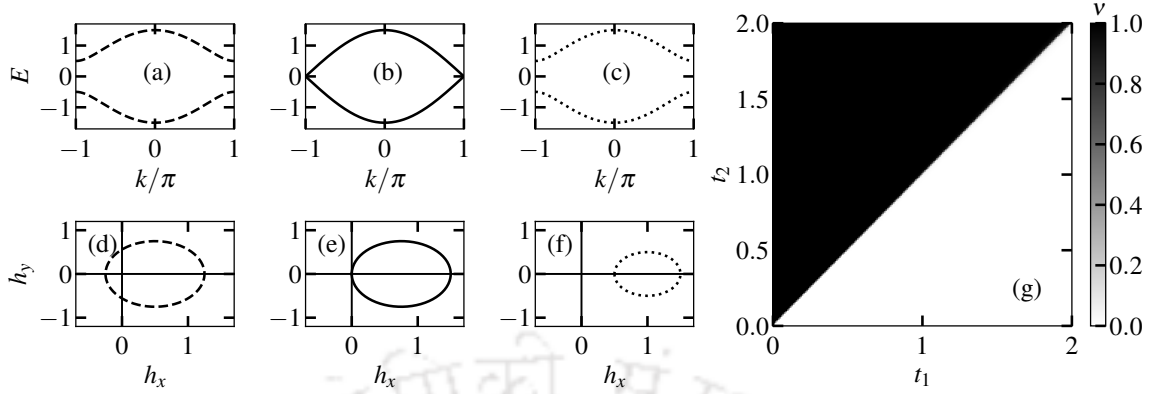


Figure 1.5: (a), (b) and (c) show the band structure for $t_1 < t_2$, $t_1 = t_2$ and $t_1 > t_2$, respectively, and (d), (e) and (f) show the variation of $\mathbf{h}(k)$ in the h_x - h_y plane for $t_1 < t_2$, $t_1 = t_2$ and $t_1 > t_2$, respectively. (g) shows the winding number ν in the t_1 - t_2 plane.

structure. However, to obtain the full information one needs to take the eigenvectors into account as well. Using the Pauli matrices $\{\sigma_i\}$ as basis one can write the band Hamiltonian as

$$H(k) = \mathbf{h}(k) \cdot \boldsymbol{\sigma}. \quad (1.14)$$

Now, the three components of $\mathbf{h}(k)$ can be written as

$$\begin{aligned} h_x(k) &= t_1 + t_2 \cos(k) \\ h_y(k) &= t_2 \sin(k) \\ h_z(k) &= 0. \end{aligned} \quad (1.15)$$

With this the trajectory of $\mathbf{h}(k)$ in the h_x - h_y plane over the first Brillouin zone gives the full set of eigenstates and its magnitude gives the eigenvalues. Now the plot in Fig. 1.5 shows the dissimilarity between the two staggered hopping cases, namely $t_1 > t_2$ and $t_1 < t_2$. Due to the periodicity of the Brillouin zone, the vector $\mathbf{h}(k)$ will form a closed loop. For one of the insulating cases ($t_1 < t_2$) the vector winds around the origin (or the gap-closing critical point) while it does not do so in the other insulating case ($t_1 > t_2$). The number of times the trajectory of $\mathbf{h}(k)$ winds around the critical point can be coined as a winding number. However, the proper way to calculate the winding number is done by integrating the Zak phase, the 1D realization of the Berry phase, over the entire Brillouin zone ($-\pi/a \leq k \leq \pi/a$). So the winding number formula reads as

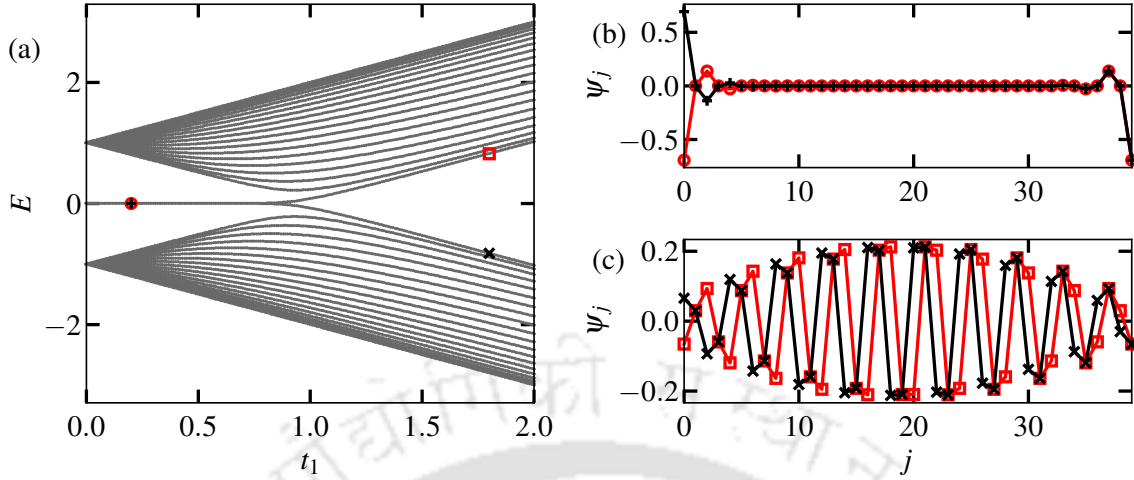


Figure 1.6: Figure (a) shows the single-particle energy spectrum of the model (1.9) as a function of t_1 with fixed $t_2 = 1$ for $L = 40$. Figure (b) shows the wave amplitude of the two states marked by red circle and black plus in (a). Figure (c) shows the wave amplitude of the two states marked by red square and black cross in (a).

$$\nu = \int_{BZ} dk \langle k | i\partial_k | k \rangle. \quad (1.16)$$

Fig. 1.5 (g) shows ν in the $t_1 - t_2$ plane which clearly distinguishes the two gapped phases: $\nu = 1 (= 0)$ for $t_1 < t_2$ ($t_1 > t_2$). Thus, the winding number acts as a non-trivial topological invariant for the SSH model.

Further insights into the SSH model can be achieved by looking at the real space energy spectrum for open boundary conditions. In Fig. 1.6, we plot the eigenvalues of each state for a fixed value of inter-cell hopping and varying intra-cell hopping. When $t_1 < t_2$, gapped states appear in the spectrum with two degenerate zero energy modes lying between them. Interestingly, these zero energy modes are exponentially localized on both the edges of the lattice, hence, we can call them as edge states. On the other hand, no such states are found when $t_1 > t_2$, instead the system behaves as an ordinary band insulator. The winding number, a property of the bulk, is a topological invariant. Contrarily, the number of edge states at the left (or right) edge is a property of the edge. The interplay between the bulk and the edge is known as bulk-boundary correspondence. Moreover, due to the emergence of a finite (zero) winding number along with the pair of (no) edge states the gapped phase for $t_1 < t_2$ ($t_1 > t_2$) can be called as a topological (trivial) insulator. Hence, the gap closing transition occurring at $t_1 = t_2$ is a topological phase transition.

The topology of the SSH model is protected by what is known as the chiral sym-

metry. Since the system is bipartite, no hopping is allowed between same sublattice sites (A and B), and we can define projectors on these sites as $P_A = \sum_{r=2j} |r\rangle\langle r|$ and $P_B = \sum_{r=2j+1} |r\rangle\langle r|$ where j is the unit cell index. Then the chiral operator can be defined as $\Gamma = P_A - P_B$, which is unitary, Hermitian and local. This operator anticommutes with the Hamiltonian, i.e., $\Gamma H_{SSH} \Gamma = -H_{SSH}$. One important consequence of the chiral symmetry is that the energy spectrum is symmetric: an eigenstate $|\psi\rangle$ with energy E has a chiral partner $\Gamma|\psi\rangle$ with energy $-E$. Moreover, the zero energy edge states are their own chiral partner ($\Gamma|\psi_0\rangle = |\psi_0\rangle$). Therefore, these states can be decomposed such that they occupy a single sublattice site only. It is also important to note that the addition of onsite terms breaks the chiral symmetry.

1.4 Effect of interaction on topology

So far we discussed the physics at the single particle level. However, in the presence of interaction the physics cannot be described via single particle picture, rather a many-body prescription is needed for the same. In the following section, we emphasize the effect of various interactions on the SSH model and analyze the emerging ground state phase diagrams. Let's consider the SSH model with a two-body onsite interaction term of strength U and a nearest-neighbour interaction term of strength V which is represented by the Hamiltonian

$$H = -t_1 \sum_{i \in \text{odd}} (a_i^\dagger a_{i+1} + H.c.) - t_2 \sum_{i \in \text{even}} (a_i^\dagger a_{i+1} + H.c.) \quad (1.17)$$

$$+ \frac{U}{2} \sum_i n_i(n_i - 1) + V \sum_i n_i n_{i+1}.$$

This model is the bosonic version of the original SSH model. Therefore, the statistics of bosons gives us the freedom to consider more than one particle per site. However, we first analyze the many-body phases with hardcore constraint, which is achieved when the onsite interaction is very strong, i.e., when $U \rightarrow \infty$. Now due to the constraint imposed, a maximum of one particle per site is allowed ($(a^\dagger)^2 = 0$) and due to this the second term in the Hamiltonian vanishes. In Fig. 1.7, we show the non-interacting phase diagram of the model with hardcore constraint in the $t_2 - \mu$ plane for a fixed $t_1 = 1$. As expected from the single-particle spectrum, due to finite dimerization, the system exhibits a gapped phase at half-filling, i.e., at $\rho = N/L = 1/2$ up to the gap closing point $t_2 = t_1$ where L and N are the number of

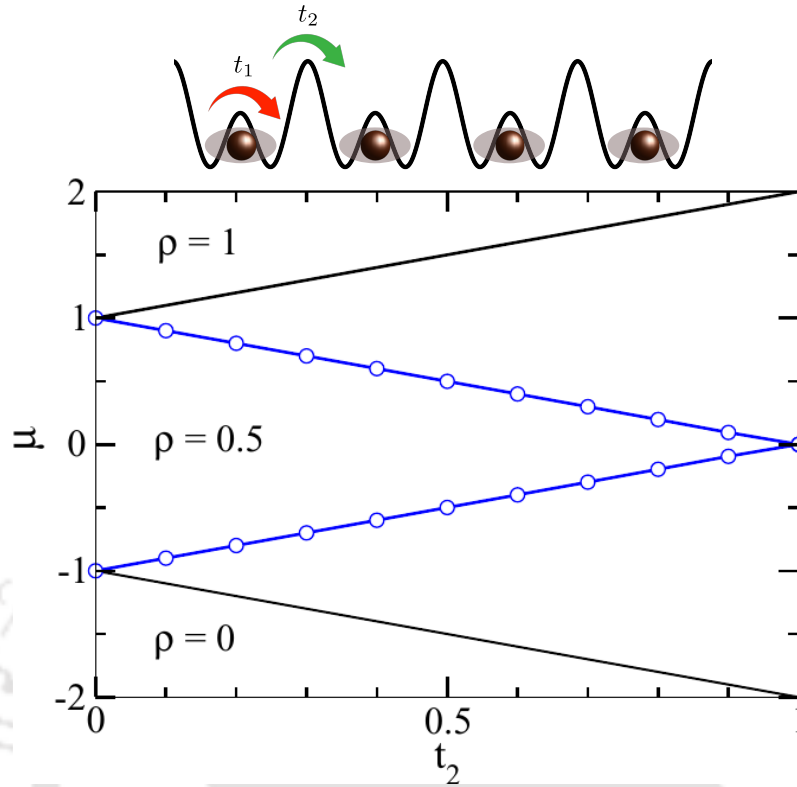


Figure 1.7: Phase diagram of the model 1.17 as a function of t_2 in the non-interacting limit ($U = V = 0$) for fixed $t_1 = 1$. Here the bosons are considered to be of hardcore in nature. The figure is taken from [1].

lattice sites and the number of bosons, respectively. This gapped phase is known as a bond order (BO) phase, which is characterized by the large and small bond energies along the alternating bonds. The gap in the spectrum can be understood via the cartoon diagram shown in Fig. 1.7. For $t_2 < t_1$ a single particle gets localized at each unit cell which can hop within the cell only, and since hardcore constraint is imposed, the addition of another particle to the system costs extra energy. However, for the doped case, i.e. at incommensurate densities, the system is a gapless superfluid (SF).

When the nearest-neighbour interaction V is turned on, for a fixed dimerization, the system exhibits a gapped-gapped phase transition from the BO phase to a density wave (DW) phase at $\rho = 1/2$ (Fig. 1.8). The latter arises due to strong repulsive interaction between the bosons and it is characterized by alternating filled and empty lattice sites. Note that here we consider the trivial BO phase ($t_2 < t_1$). However, if we consider $t_2 > t_1$ and vary V then there occurs a non-trivial BO to DW phase transition (not shown). Therefore, strong nearest neighbour interaction

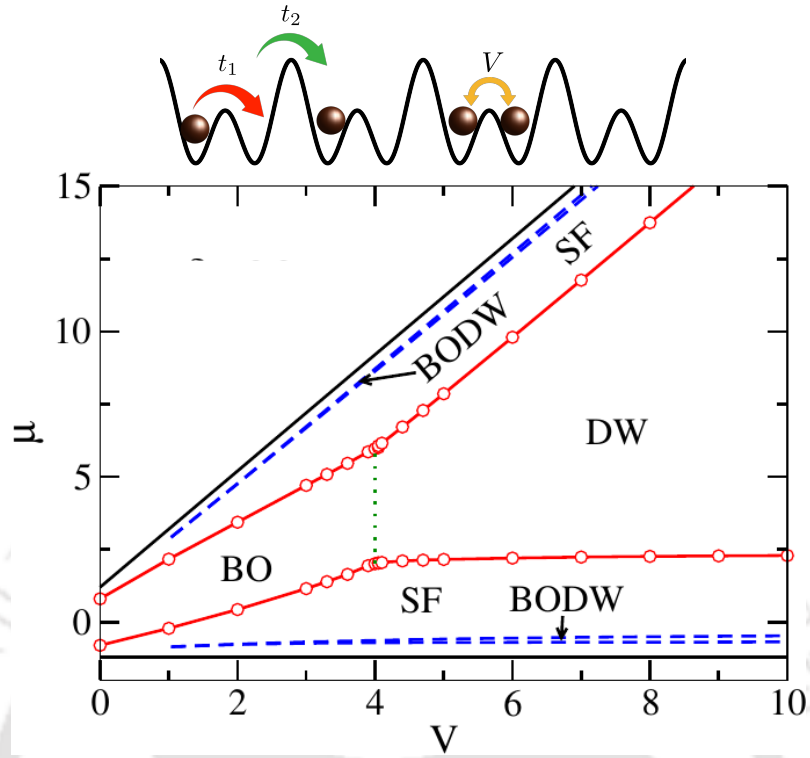


Figure 1.8: Phase diagram of the model 1.17 with hardcore bosons as a function of V for fixed $t_1 = 1$ and $t_2 = 0.2$. The figure is taken from [2].

destroys the topology of the SSH model. From Fig. 1.8 we further notice that at $\rho = 1/4, 3/4$ an interesting phase arises which exhibits the character of both the BO and the DW phases, hence the name bond order density wave (BODW) phase.

Now we move away from the hardcore limit and consider three-body constrained bosons, which allows a maximum of two particles per site ($(a^\dagger)^3 = 0$). Here the two-body interaction becomes finite and the second term in the Hamiltonian comes into play. In Fig. 1.9 the phase diagram in $U/t_{1,2} - t_1/t_2, t_2/t_1$ plane is shown for vanishing nearest-neighbour interaction $V = 0$ at $\rho = 1$. When the onsite interaction U is strongly repulsive, the system exhibits a Mott insulator (MI) phase. However, when the interaction becomes strongly negative, the pair bond order (PBO) phases emerge due to the combined effect of attractive interaction and the hopping dimerization ($t_1 \neq t_2$). Depending on whether t_1 dominates over t_2 or vice versa, the PBO phase is either trivial or topological in nature. The θ in PBO_θ stands for the associated Berry phase, which is finite in the topological phase and vanishes in the trivial phase. For uniform hopping in the attractive interaction regime a pair superfluid phase arises and the area enclosed by the solid black line with diamonds denotes a

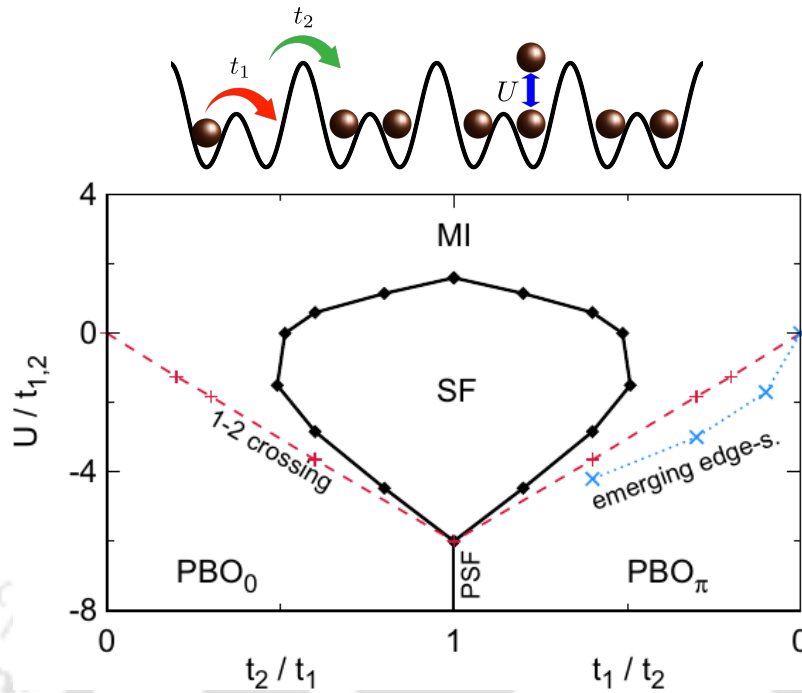


Figure 1.9: Phase diagram of the model 1.17 in the $U/t_{1,2} - t_1/t_2, t_2/t_1$ plane for $V = 0$. Here three-body constrained bosons at unit filling ($\rho = 1$) are considered. The figure is taken from [3].

gapless superfluid phase. It is interesting to note that the topology of the SSH model is favoured by the interaction for specific values of U . Apart from the topological phase at $\rho = 1$ this type of interaction has been found to favour topological phases at other fillings as well. For example in [13], it is shown using the same model that a bond order phase with edge localized zero energy modes emerges at $\rho = 0.5$ for strong repulsive U .

To summarize, interaction can either suppress or favour the topology of the SSH model. In all the above cases the root of the topology lies in the hopping dimerization. However, another class of topological insulators, known as the Haldane insulators (HIs), emerge without any dimerization and arise solely due to competing onsite and nearest-neighbour interactions. The HI was first predicted in the spin-1 XXZ model and subsequently in the extended Bose-Hubbard model (EBHM) in one dimension [14]. Fig. 1.10 shows the phase diagram of the EBHM in the $V - U$ plane for three-body constrained bosons at $\rho = 1$ and for uniform hopping strengths $t_1 = t_2 = t$. The phase diagram reveals that the system is a gapless superfluid when both types of interaction are small. However, for large U (V) a MI (DW) phase is stabilized. Interestingly, for some intermediate values of U and V , an HI phase

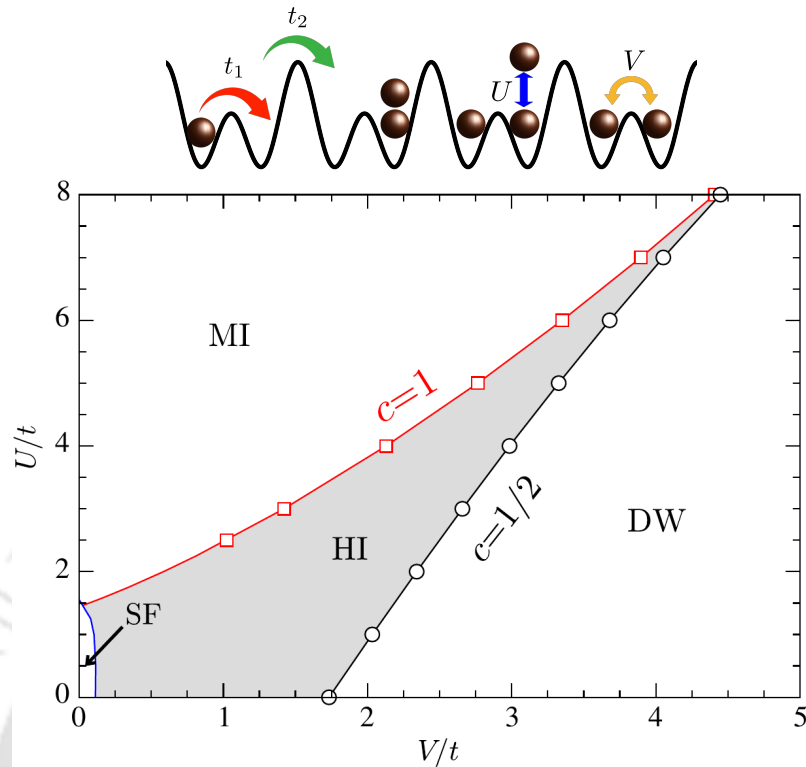


Figure 1.10: Phase diagram of the model 1.17 in the $U - V$ plane for vanishing dimerization ($t_1 = t_2 = t$). Here the maximum number of bosons per site is considered to be two. The figure is taken from [4].

emerges, which is found to possess non-trivial topological character. This phase has a non-local order captured via a string order parameter, as opposed to the local ordering in the MI and DW phases.

1.5 Localization transition

The term localization in the context of condensed matter means that the wavefunction of an electron gets concentrated at a particular lattice site. Localization gives rise to the ceasing of particle motion in the lattice and makes the system insulating. Delocalization, on the other hand, accounts for the uniform distribution of the wave amplitude throughout and the corresponding system shows a metallic behaviour. The delocalization-localization transition or vice versa is termed as localization transition, which has garnered huge attention from the condensed matter physicists post the seminal work by Anderson.

1.5.1 Anderson localization

In condensed matter physics, the transport of electrons in a periodic lattice is described via the Bloch theory. A Bloch wavefunction is extensive in nature (i.e. spans through entire lattice) and results from the product of a plane wave and a periodic potential with the same periodicity as the lattice. Moreover, the Bloch wave associates each state of the single-particle spectrum with a crystal momentum and a band index. Therefore, the system in question can be studied in terms of band theory where the energy is a continuous function of the momentum. Although the band theory has found its success in various systems with negligible to moderate disorder, it fails when the system is highly disordered. In this case, the disorder can no longer be treated as a perturbation and it becomes an integral part of the system's Hamiltonian. In the presence of disorder, the single-particle eigenstates become exponentially localized which was first described by Anderson in his seminal work and thus, the phenomenon is famously known as Anderson localization [15]. This remarkable finding led the foundation of transition from a metallic phase where the electrons move freely, to an insulating phase where the electrons get trapped into small regions of a lattice with irregular potential depths.

1.5.2 Scaling theory of localization

Scaling theories describe how the properties of a system change with system size. These theories are widely used to understand the phase transitions and critical phenomena. After the pioneering work by Anderson on localization transition, the so called “gang of four” (Abrahams, Anderson, Licciardello, and Ramakrishnan) proposed the scaling theory of localization that provided further insights into the disorder induced metal-insulator transition in different dimensions. Their work was a handy extension on a few previous works on disordered systems. Defining a dimensionless conductance of the form $g = G/(e^2/\hbar)$, Thouless had previously argued that the conductance g_0 can measure the amount of disorder present in a system at some characteristic length scale. For extended and localized systems the mean free path l and localization length ξ act as the length scale. He also proved that for a d -dimensional system with side length (or system size) L , the dimensionless conductance g scales with L^d as a function of g_0 . The gang of four, later expanded upon his arguments and defined a universal scaling function β which depends only on g :

$$\beta(g) = \frac{d \ln(g)}{d \ln(L)}. \quad (1.18)$$

This parameter describes the variation of g with the change in system size. If the system is localized then $\beta(g)$ is expected to take negative values. The influence of disorder on the degree of localization can be understood from the behaviour of $\beta(g)$ as follows. In the absence of disorder, the conductance should obey the Ohm's law for $L \gg l$, i.e., $g(L) \sim \sigma L^{(d-1)}$ where σ is the conductivity of the medium. This implies that $\beta(g)$ would scale as

$$\beta(g) = (d - 2). \quad (1.19)$$

In the presence of weak but finite disorder, according to perturbation theory there exists a correction of g^{-1} to the same. Thus, beta varies with g as

$$\beta(g) = (d - 2) - ag^{-1}, \quad (1.20)$$

where a ($= \pi^{-2}$ for an electron gas) takes a constant value. From the formula above, it is evident that $\beta(g)$ acquires a lower values as compared to a disorder-free system. However, when the disorder is strong the conductance sees an exponential fall with $L \gg \xi$ due to localization. Thus, $g(L) \propto \exp(-L/\xi)$ and subsequently,

$$\beta(g) \sim \ln(g/g_c), \quad (1.21)$$

where g_c is a critical value of the conductance which separates the extended regime from the localized regime.

If $\beta(g)$ is continuous and monotonic then from Fig. 1.11 several conclusions about localization transition can be drawn. In one dimension, as expected, $\beta(g)$ is always negative as a function of g which indicates that the system becomes localized for any disorder strength. Therefore, the existence of a metal-insulator transition is ruled out. However, in three dimension the extended and localized phases are well separated by the critical $g(= g_c)$, marked by the yellow dot in Fig. 1.11. At this point, the conductance curve crosses the x -axis ($\beta(g) = 0$ line). On the other hand, the situation of two-dimensional systems is similar to one-dimension but here the localization length increases exponentially with the decrease in disorder strength. This means that a weakly disordered system would appear to be of metallic nature even though all the states are localized, since $\xi > L$ in this case.

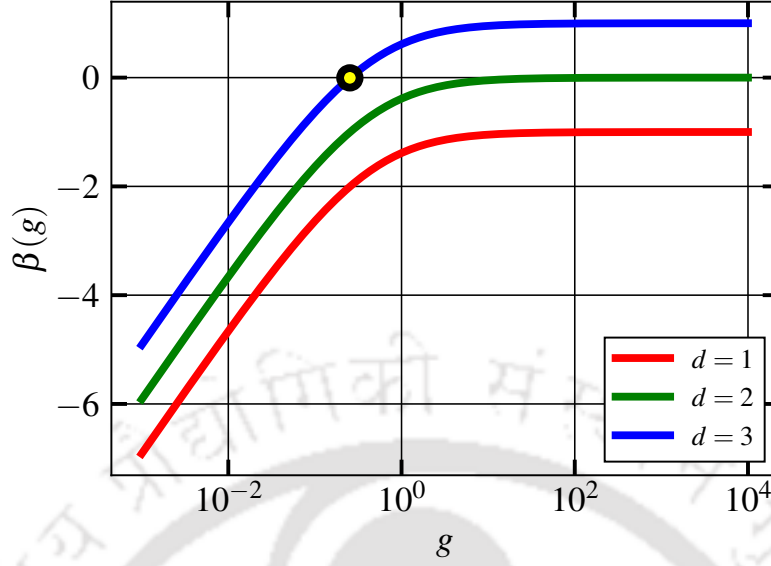


Figure 1.11: Scaling theory of localization which shows the variation of the scaling function for $d = 1, 2$ and 3-dimensions. Here the yellow dot marks the critical point g_c corresponding to $d = 3$.

1.5.3 Aubry-André model

Up to this point we understood that electrons in a 1D periodic lattice can hop freely from one site to another. However, their movement ceases in presence of any finite random disorder due to Anderson localization. Therefore, a metal-insulator transition in 1D is not possible for such uncorrelated disorder. Few years after Anderson's work the Aubry-André (AA) model [16] was proposed which shows a proper delocalization-localization transition even in one dimension. This model can be described by a quasiperiodic lattice which is intermediate to both periodic and random lattices. The tight-binding Hamiltonian of the AA model reads as

$$H = -J \sum_i (c_i^\dagger c_{i+1} + H.c.) + \lambda \sum_i \cos(2\pi\beta i + \phi) n_i, \quad (1.22)$$

where $c_i^\dagger (c_i)$ is the fermionic creation (annihilation) operator and J is the hopping rate between nearest neighbour sites. The onsite disorder term with strength λ is spatially modulated by the wave number $2\pi\beta$ and a phase shift of ϕ . Quasiperiodicity means that the lattice does not repeat itself after a fixed interval and it can be achieved by considering β as an irrational number. Theoretically β can be chosen as the ratio between two consecutive Fibonacci number F_{n-1}/F_n for a lattice of length $L = F_n$. This ratio approximates to $(\sqrt{5} - 1)/2$, the Golden mean, for

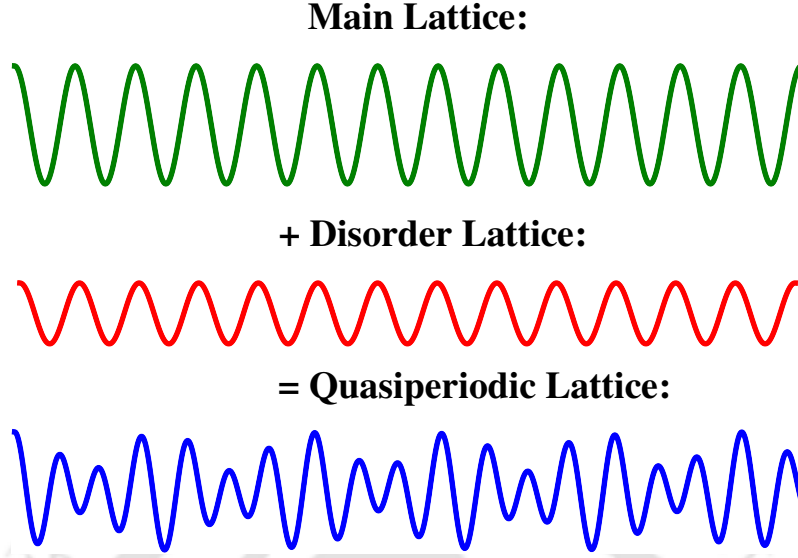


Figure 1.12: The figure shows a main lattice, a disorder lattice and the quasiperiodically disordered lattice resulting from the two.

large enough system size. In experiment, however, quasiperiodicity is accomplished by setting the wavelength of a disorder lattice incommensurate to that of the main lattice. Fig. 1.12 depicts the main lattice, the disorder lattice and the resulting quasiperiodic lattice out of the two.

One of the highlighting properties of the AA model is the self-duality. To understand this we first re-write the Hamiltonian using the Wannier representation as

$$H = -J \sum_j (|w_j\rangle \langle w_{j+1}| + |w_{j+1}\rangle \langle w_j|) + \lambda \sum_j \cos(2\pi\beta j + \phi) |w_j\rangle \langle w_j|. \quad (1.23)$$

On using a special kind of Fourier transformation

$$|k_l\rangle = \sum_j e^{2\pi\beta i k_l j} |w_j\rangle \quad (1.24)$$

the real space Hamiltonian can be transformed into the momentum space Hamiltonian

$$H_k = -\frac{\lambda}{2} \sum_l (|k_l\rangle \langle k_{l+1}| + |k_{l+1}\rangle \langle k_l|) + 2J \sum_l \cos(2\pi\beta l + \phi) |k_l\rangle \langle k_l|. \quad (1.25)$$

Notice that the Hamiltonian in both position and momentum spaces looks similar

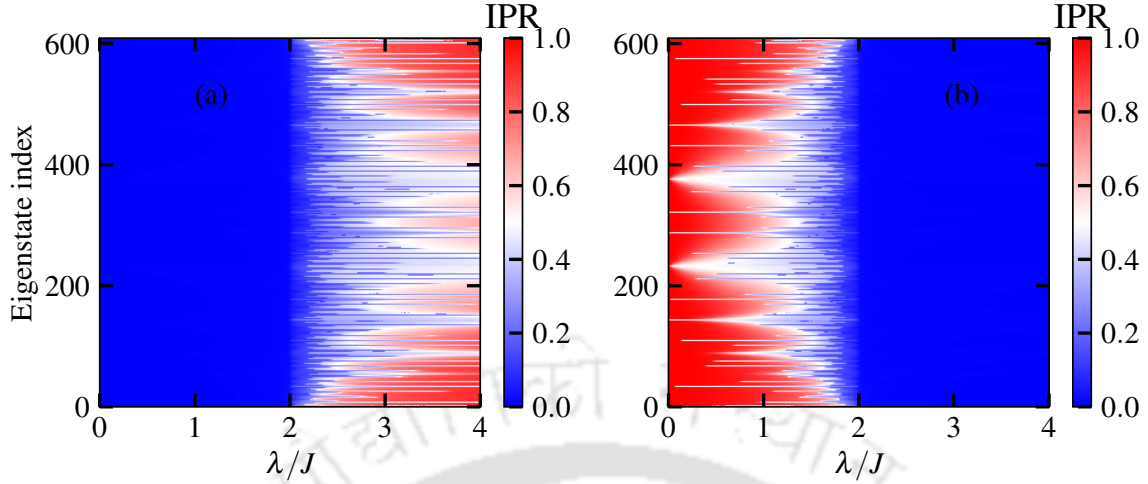


Figure 1.13: The IPR as a function of eigenstate index and disorder strength λ in the (a) real space and (b) momentum space.

except the fact that the hopping rate in the real space becomes the disorder strength in the momentum space and vice versa. This suggests that both the Hamiltonians H and H_k can be transformed exactly into each other by considering $\lambda/J = 2$.

To study the localization transition in the AA model we compute two observables known as the inverse participation ratio (IPR) and the normalized participation ratio (NPR). For the i -th eigenstate of a system IPR and NPR are defined as

$$\text{IPR}_i = \sum_i |\psi_i^n|^4 \quad (1.26)$$

and

$$\text{NPR}_i = \frac{1}{L \sum_i |\psi_i^n|^4}, \quad (1.27)$$

respectively. The IPR goes as $1/L$ for an extended state whereas it approaches to unity for a state localized at a single lattice site. On the other hand, the NPR acts in a reverse fashion, i.e., it becomes finite (vanishes as $\sim 1/L$) for an extended (a localized) state. In Fig. 1.13 we show the IPR as a function of varying disorder strength λ and eigenstate number both in the real space and in the momentum space. The real space plot signifies that all the states are extended up to $\lambda/J = 2$, after which a transition occurs to a phase with all localized states. Contrarily, in the momentum space all the states are localized (extended) for $\lambda/J < 2$ ($\lambda/J > 2$). Therefore, this analysis numerically confirms the self-duality property of the AA model and the critical point $\lambda/J = 2$ can be called as the self-dual point. Further, we plot the $\langle \text{IPR} \rangle$ and $\langle \text{NPR} \rangle$, which are the IPR and NPR values averaged over

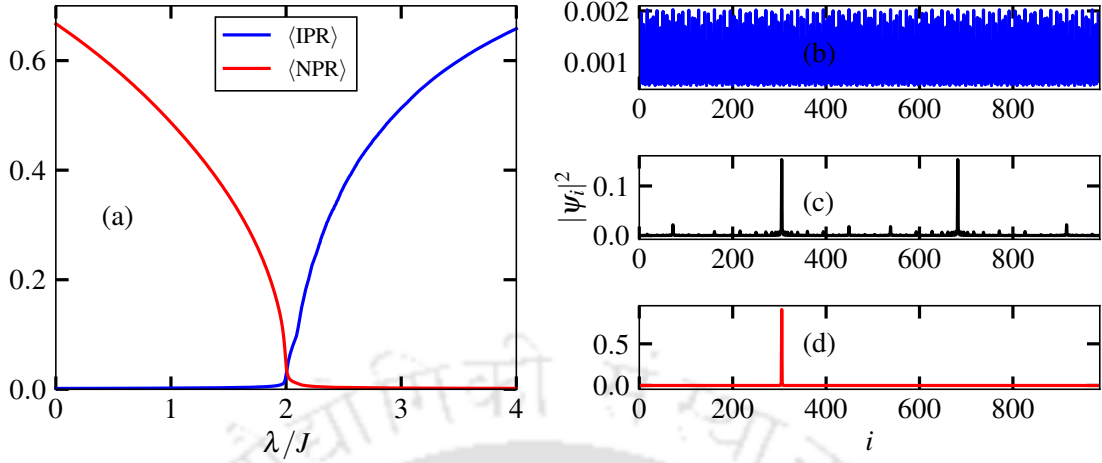


Figure 1.14: (a) shows $\langle \text{IPR} \rangle$ and $\langle \text{NPR} \rangle$ as a function of disorder strength λ . (b-d) show the probability density $|\psi_i|^2$ of the ground state with respect to lattice sites i for $\lambda = 1, 2$ and 3 , respectively.

the entire spectrum, as a function of λ in Fig. 1.14(a). These quantities clearly distinguish the localized phase from the extended one. Both $\langle \text{IPR} \rangle$ and $\langle \text{NPR} \rangle$ become finite from zero or vice versa at the critical point, which signifies a sharp localization transition of the AA model. Now we investigate the nature of individual eigenstates in different phases. Fig. 1.14 (b)-(d) show the probability density $|\psi_i|^2$ of the lowest energy eigenstate at each lattice site for $\lambda = 1, 2$ and 3 . When the system lies in the extended phase ($\lambda = 1$) the probability density has weight on all the lattice sites but in the localized phase ($\lambda = 3$) the eigenstate is localized at one site only. However, the multiple peaks along with the vanishing probability at most of the sites for $\lambda = 2$ signify a critical behaviour of the system. At this point all the states are critical, i.e., neither they are extended nor they are completely localized. These critical states are also known as multifractal states which correspond to the fractal energy spectrum of the system.

The AA model shows a localization transition only when β is incommensurate (or in other words, irrational). However, for other β values the energy spectrum shows interesting behaviour at the transition point. In Fig. 1.15 we plot the eigenvalues with respect to varying β . For $\lambda = 2$ the energy spectrum produces a Hofstadter butterfly, which describes the physics of an electron moving under the influence of a transverse magnetic field in a two dimensional square lattice.

The experimental setup to study the Aubry-André model is based on the following quasiperiodic lattice in the continuum limit:

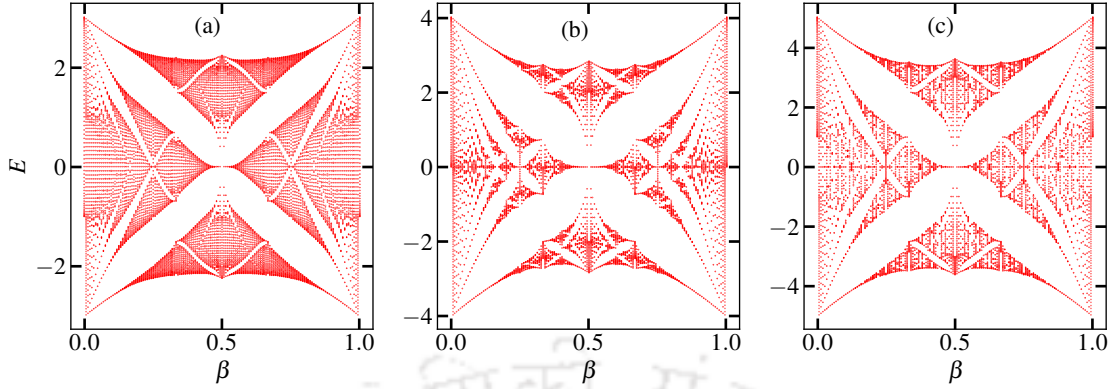


Figure 1.15: Energy spectrum as a function of β for (a) $\lambda = 1$, (b) $\lambda = 2$ and (c) $\lambda = 3$.

$$H_{cont} = \frac{-\hbar^2}{2m} \frac{d^2}{dx^2} + V_p \sin^2(k_p x) + V_d \sin^2(k_d x + \phi). \quad (1.28)$$

Here V_p and V_d are respectively the depth of the primary and detuning lattices, k_p and k_d are the respective wave numbers and ϕ is the phase offset between the two. With proper choices of the parameters the continuum Hamiltonian can be mapped into the AA Hamiltonian by considering the tight-binding approximation. Then one can expect sharp localization transition as a function of the disorder. However, away from the tight-binding limit, we cannot be restricted to the nearest-neighbour approximation, rather we need to consider higher order terms of the Wannier functions as well. Thus, some extra terms appear alongside the Aubry-André model which leads to the breakdown of the self-duality condition. In Fig. 1.16(a) we show the $\langle \text{IPR} \rangle$ and $\langle \text{NPR} \rangle$ values as a function of V_d to investigate the localization properties of H_{cont} . Interestingly, the localization transition in this case is not sharp, rather it occurs via a range of V_d values (marked by the shaded yellow area). Note that in this regime both $\langle \text{IPR} \rangle$ and $\langle \text{NPR} \rangle$ remain finite and the associated phase can be called as an intermediate phase. Now to investigate this phase further we look at the individual IPR values plotted as a function of the energy E and V_d (Fig. 1.16(b)). In the extended phase ($V_d \lesssim 1.4$) all the states are extended, as indicated by the vanishing IPR value, whereas all the states localized in the localized phase ($V_d \gtrsim 1.6$), as indicated by the finite value of IPR. However, in the intermediate phase a mixture of extended and localized phase appears and they are separated by the solid black line. Therefore, we observe a localization transition as a function of eigenstate number for a fixed value of V_d and the corresponding critical energy eigenvalue is known as mobility edge. Note that the appearance of mobility edge in a system is linked to

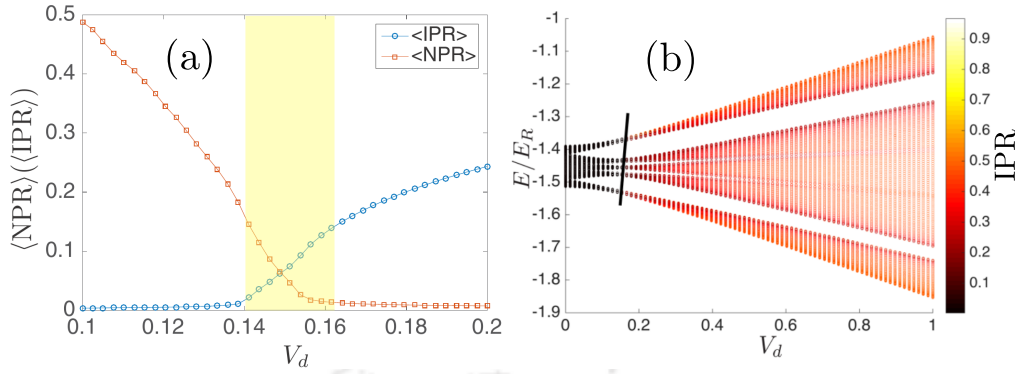


Figure 1.16: (a) shows $\langle \text{IPR} \rangle$ and $\langle \text{NPR} \rangle$ as a function of disorder potential depth V_d . (b) shows the IPR values as a function of energy eigenvalues and V_d . The shaded yellow area in (a) denotes the intermediate phase. This figure is taken from [5].

the breakdown of self-duality property. However, the Pixley-Ganeshan-Das Sarma model, a generalized version of the AA model, is an exception to this theory. This particular model exhibits exact mobility edge even without breaking the self-duality.

1.6 Effect of disorder on topology

The topology of a system is mainly characterized by the bulk-boundary correspondence which connects the existence of edge modes to a bulk topological invariant. Ever since the topological phenomenon was discovered, efforts have been made to study its robustness against various perturbations. The edge states can withstand weak to moderate disorder strength as long as the bulk gap does not vanish. These edge localized states are protected by certain underlying symmetry (ies) which either get completely destroyed or they are respected up to a particular disorder strength. However, the discovery of topological Anderson insulator (TAI) led the foundation of a disorder-induced topological phase, which does not exist in the absence of disorder [17]. TAI has been extensively studied in theory [18–34] as well as in experiments [35–37]. Moreover, it has been revealed that the localization transition is not necessarily tied to the topological phase transition, i.e., both these transitions do not occur at the same critical point [38, 39]. In the following we discuss the effect of disorder on topology in one dimension by taking the SSH model as an example.

1.6.1 Effect of hopping disorder

We first analyze the consequences of hopping disorder on the SSH model. This type of disorder is sometimes called as chiral disorder because it respects the chiral

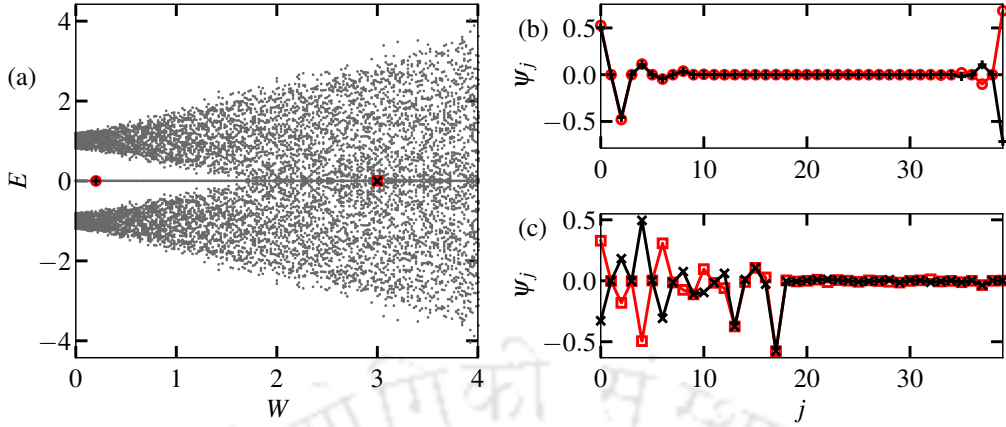


Figure 1.17: (a) Shows the single-particle energy spectrum as a function of hopping disorder strength W for $L = 40$ sites for fixed $t_1 = 0.2$ and $t_2 = 1$. (b) shows the wave amplitudes for the states marked by the red circle and black plus in (a). (c) shows the wave amplitudes for the states marked by the red square and black cross in (a).

symmetry of the model. We consider the following Hamiltonian

$$H' = H_{SSH} - \sum_j \epsilon_j (a_j^\dagger b_j + H.c.) - \sum_j \epsilon_j (a_j^\dagger b_{j-1} + H.c.) \quad (1.29)$$

where H_{SSH} is the SSH Hamiltonian presented in Eq. 1.9 and ϵ_j is a random number drawn from the uniform distribution in $[-W/2, W/2]$. The last two terms of H' basically represent the disorder in the intra-cell and inter-cell hoppings with a strength W . In Fig. 1.17(a) we show the single particle energy spectrum as a function of W for fixed hopping amplitudes ($t_1 = 0.2, t_2 = 1$) and for a single disorder realization. The figure portrays that in the absence of disorder two degenerate zero energy modes lie inside the bulk gap. When the disorder strength increases these states still remain degenerate and edge localized (Fig. 1.17(a)), indicating a robustness of the topology. However, the bulk gap decreases with the decrease in W and after a critical point the bulk gap closes. Once the gap vanishes the two zero energy states are no longer localized on the edges and their wave amplitude has weight even in the bulk of the lattice.

1.6.2 Effect of onsite disorder

Now we discuss the consequences of disorder introduced as an onsite energy to the system. For this purpose we consider the Hamiltonian

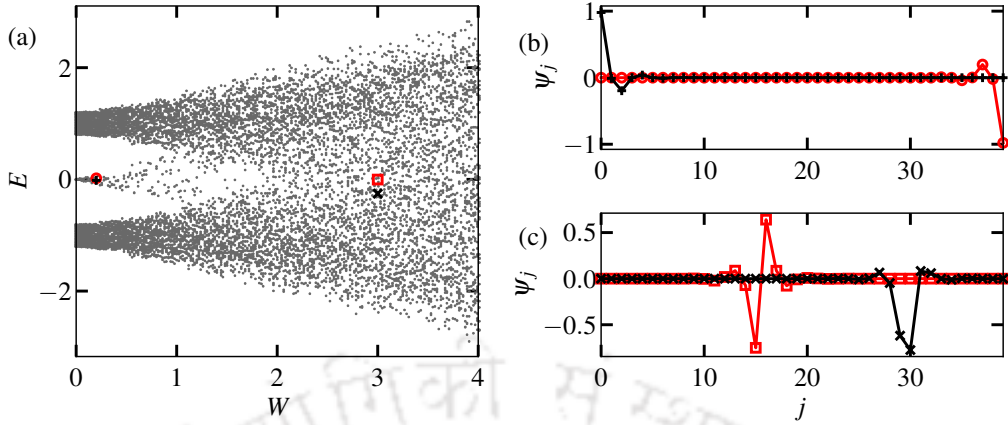


Figure 1.18: (a) Shows the single-particle energy spectrum as a function of onsite disorder strength W for $L = 40$ sites for fixed $t_1 = 0.2$ and $t_2 = 1$. (b) shows the wave amplitudes for the states marked by the red circle and black plus in (a). (c) shows the wave amplitudes for the states marked by the red square and black cross in (a).

$$H' = H_{SSH} + \sum_j \epsilon_j (a_j^\dagger a_j + b_j^\dagger b_j) \quad (1.30)$$

where again ϵ_j is a random number drawn from the uniform distribution in $[-W/2, W/2]$. Notice that the disorder term is added as an onsite term of the Hamiltonian. From the previous section we learned that in one dimension for any finite random disorder the system becomes localized. Therefore, it will be interesting to see the interplay between Anderson localization and topology in the SSH model. In Fig. 1.18(a) we plot the energy spectrum as a function of W for a fixed hopping dimerization ($t_1 = 0.2, t_2 = 1$). The figure shows that the zero energy edge states become energetic as soon as disorder becomes finite. Thus, the degeneracy of these states gets broken and the chiral symmetry is not preserved anymore. However, they remain localized in the edge lattice sites until they merge into the bulk (Fig. 1.18(b)). Another important thing is to be noted that the bulk gap shrinks with increase in W and never opens up again once it is closed. Also, the middle two states after gap closing get localized in the bulk due to Anderson localization.

At this point it is understood that interaction and disorder may impart significant effects on the topological properties of the systems. In recent years a great deal of effort have been made to understand these effects in various systems both theoretically and experimentally. In this thesis we will primarily focus on the interaction induced topological phases in low dimensional lattice models first and then we will study the role of disorder on the topological phases. All the studies are performed

using different numerical methods. This thesis is divided into seven chapters and the chapter wise outline is given in the following.

1.7 Chapterwise outline of the thesis

In **Chapter 1** , we first introduce the concepts of quantum phase transitions. Then we discuss the topological phenomenon in condensed matter with particular focus on one dimension by considering the SSH model as an example. In the next part, starting from the Anderson localization problem, we discuss the role of quasiperiodic disorder to govern localization transitions in one dimensional systems. Then we provide a brief discussion on the interplay between topology and disorder in one dimensional lattices.

After introducing the motivation of our work, we provide the details of the numerical methods used in this thesis in **Chapter 2** . We first discuss the exact diagonalization method and then we have focused on the more sophisticated density matrix renormalization group method based on the matrix product states approach.

In **Chapter 3** , we analyze the ground state properties of a one-dimensional lattice with dimerized nearest neighbour interactions. In this context we show how dimerized interaction can alone stabilises a symmetry protected topological phase in the system. In the initial part of the chapter we discuss the phase diagram and the nature of the emerging quantum phases at half-filling. Then we identify and provide the signatures of a symmetry protected topological phase transition in the system. Further we consider a two-component system where the first component possesses a staggered onsite potential and the hopping of the second component depends on the onsite occupation of the first one. In this case we show that the second component turns topological by varying the staggered potential of the first component.

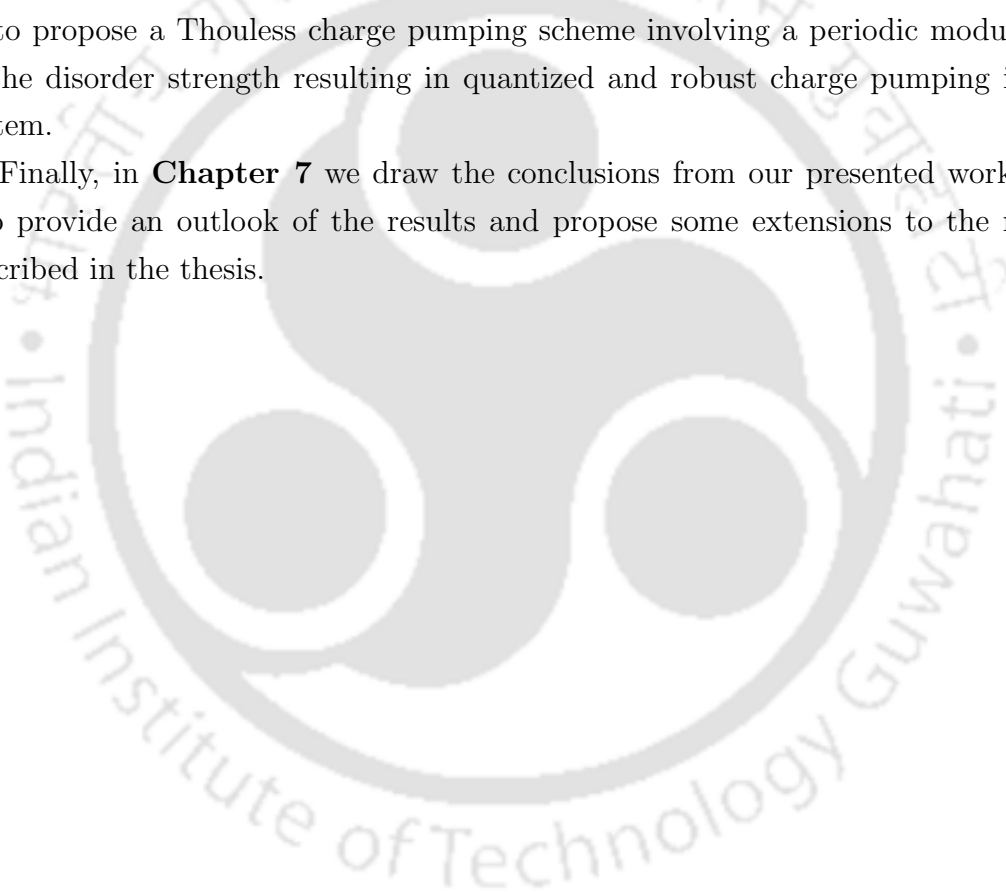
In **Chapter 4** , we consider a system of hardcore bosons on two coupled SSH chains in the form of a two-leg ladder and then study the ground state properties using the DMRG method. Starting from the single particle picture, we study the many-particle problem at half filling in the absence and presence of inter-leg interaction. We perform a detailed study on how interaction affects the topological phase transitions and also induce a topological transition in the system.

In the rest of the thesis our focus is to understand the effect of quasiperiodic disorder on the topological properties of a one dimensional non-interacting system. In this context we first discuss the localization transition in the presence of quasiperiodic disorder in a one dimensional lattice with onsite staggered potential in **Chapter**

5. We show how the combined effect of quasiperiodic disorder and staggered on-site potential leads to the multiple re-entrant localization transition in the system where the system undergoes more than one localization transition as a function of staggered onsite potential for fixed disorder strengths. We further show that in the limit of strong staggered potential, there occurs a sharp localization transition as a function of the disorder strength.

In **Chapter 6**, we study the effect of a modified quasiperiodic disorder term on the topological nature exhibited by the SSH model. We show that for a fixed hopping dimerization, in the topological phase the system undergoes a gapped topological phase to a gapped trivial phase as a function of the disorder strength. This allows us to propose a Thouless charge pumping scheme involving a periodic modulation of the disorder strength resulting in quantized and robust charge pumping in the system.

Finally, in **Chapter 7** we draw the conclusions from our presented work. We also provide an outlook of the results and propose some extensions to the model described in the thesis.





Chapter 2

Numerical methods

In this chapter we provide the details of the numerical methods used in this thesis. In the first part we briefly discuss the exact diagonalization (ED) method and then in the second part we discuss the density matrix renormalization group (DMRG) method based on matrix product states (MPS) approach.

2.1 Exact Diagonalization (ED)

The exact diagonalization method is a straightforward approach to exactly solve quantum many-body systems which begins with the choice of a proper basis set. For example, when a Hamiltonian H is written in the second quantized form, the occupation number basis can be suitable to begin with. A complete orthonormal basis $\{|b_i\rangle\}$ can be formed by placing all the single-particle states in order and then by considering all possible configurations that occupy these states. Now, the Hamiltonian can be represented in matrix form by using the matrix elements of the form

$$H_{ij} = \langle b_i | H | b_j \rangle. \quad (2.1)$$

Note that we do not need to compute all the matrix elements using this formula. Instead, we only need to find the non-zero ones, and for this purpose we first compute $H|b_j\rangle$ and then find the index of H_{ij} with non-vanishing coefficients c_i if $H|b_j\rangle$ is written as a linear combination $H|b_j\rangle = \sum_i c_i |b_i\rangle$. There are mainly three different techniques to look for the indices, namely, Lin table, hash and binary search.

In order to have a clear understanding of this method, we consider the well known Bose-Hubbard model which includes a nearest-neighbour hopping term and an onsite interaction term, represented by the Hamiltonian

$$H = -t \sum_i (a_i^\dagger a_{i+1} + H.c.) + \frac{U}{2} \sum_i n_i (n_i - 1). \quad (2.2)$$

The simplest illustration of this model can be a two-site lattice with two interacting particles. Using all possible configurations of the basis $\{|2, 0\rangle, |1, 1\rangle, |0, 2\rangle\}$ we obtain the Hamiltonian matrix

$$\begin{bmatrix} U & -\sqrt{2}t & 0 \\ -\sqrt{2}t & 0 & -\sqrt{2}t \\ 0 & -\sqrt{2}t & U \end{bmatrix} \quad (2.3)$$

which can be diagonalized by hand because of its small Hilbert space size $D = 3$. However, for a L -site lattice with N number of particles, the Hilbert space size $D = \frac{(N+L-1)!}{N!(L-1)!}$ increases exponentially with the increase in L and N . Thus, the diagonalization becomes a really cumbersome task for the existing classical computers due to high memory requirements. For example, for a system with 20 particles residing on a lattice of 20 sites, D becomes as large as 68923264410 and it requires ~ 514 GB of RAM to store the entire basis set. In the following we discuss a diagonalization method based on the Lanczos algorithm which has been successful in studying the ground state properties with less computing effort as compared to other full matrix diagonalization methods.

2.1.1 Lanczos algorithm

Suppose we have a many-body Hamiltonian matrix H , whose eigenvalues and eigenvectors are to be computed. Our goal is to bring the matrix to a tridiagonal form whose main diagonal and the diagonals above and below it have non-zero elements. Then the ground state is to be obtained by an iterative method. The Lanczos algorithm runs on the variational principle which minimizes the energy by varying the wavefunction. The optimal algorithm is implemented as follows:

Step-1: Pick an arbitrary initial state $|\phi_0\rangle$, made up of random numbers, which has a very small yet finite overlap with the ground state $|\phi_g\rangle$, i.e., $\langle\phi_0|\phi_g\rangle \neq 0$.

Step-2: Construct the second state using

$$|\phi_1\rangle = H|\phi_0\rangle - \frac{\langle\phi_0|H|\phi_0\rangle}{\langle\phi_0|\phi_0\rangle}|\phi_0\rangle. \quad (2.4)$$

Step-3: From $n = 2$ onwards an orthogonal set of states is recursively con-

structed by

$$|\phi_{n+1}\rangle = H|\phi_n\rangle - a_n|\phi_n\rangle - b_n^2|\phi_{n-1}\rangle, \quad (2.5)$$

where the coefficients are given by

$$a_n = \frac{\langle\phi_n|H|\phi_n\rangle}{\langle\phi_n|\phi_n\rangle} \quad (2.6)$$

and

$$b_n^2 = \frac{\langle\phi_n|\phi_n\rangle}{\langle\phi_{n-1}|\phi_{n-1}\rangle}. \quad (2.7)$$

Step-4: Construct the Hamiltonian using a_n and b_n as

$$H = \begin{pmatrix} a_0 & b_1 & 0 & 0 & \dots \\ b_1 & a_1 & b_2 & 0 & \dots \\ 0 & b_2 & a_2 & b_3 & \dots \\ \vdots & \vdots & \vdots & \vdots & \ddots \end{pmatrix}. \quad (2.8)$$

Once the matrix is formed diagonalize the same with a familiar diagonalization scheme and obtain the ground state.

Step-5: If convergence is not achieved then increase n by 1 and repeat step 3-4.

The ground state energy is the smallest eigenvalue of the matrix. However, we can reach to the exact ground state energy only when n equals the Hilbert space dimension. The success of Lanczos algorithm lies in the fact that the computational effort reduces due to the formation of sparse matrix, in which most of the elements are zero.

Part of the exact diagonalization method can be implemented to study the dynamical properties of a system. Once the Hamiltonian matrix H is constructed according to the approach mentioned above, the propagation operator can be calculated using the formula $U(t) = e^{-iHt/\hbar}$, given that the time evolution is unitary. Thus, the evolved state at time t for an initial state $|\Psi(t=0)\rangle$ is

$$|\Psi(t)\rangle = U(t)|\Psi(t=0)\rangle. \quad (2.9)$$

Note that the ED method is a simple yet powerful method to solve quantum many-body system. This method together with the Lanczos algorithm can not only provide the ground state energy and wavefunction, but also the entire eigenspectrum can be computed by employing a suitable diagonalization technique, once the Hamiltonian matrix is formed. However, the exponential growth of the Hilbert space

size with increase in system size is the biggest hurdle of this method.

2.2 Matrix product states (MPS)

Matrix product states (MPS) are a class of ansatz for the one-dimensional quantum states. As the name suggests, these are the matrix product representations of a given many-body state. The ground state search using the variational principle under the MPS formalism has been highly successful in strongly correlated matters. In the following we first present the details of the MPS formalism and then provide the algorithm to implement the density matrix renormalization group (DMRG) method using the same.

Consider an exemplary system with two basis states $|\uparrow\rangle$ and $|\downarrow\rangle$. A simple state can be written as the product of these two as

$$|\Psi\rangle = |\uparrow\rangle \otimes |\downarrow\rangle. \quad (2.10)$$

In general, a state can be written in terms of a product of two sites as

$$|\Psi\rangle = (a|\uparrow\rangle + b|\downarrow\rangle) \otimes (c|\uparrow\rangle + d|\downarrow\rangle). \quad (2.11)$$

Further, these can be written as an outer product of two element vectors as

$$|\Psi\rangle = \sum_{\sigma_1, \sigma_2} V_{\sigma_1} |\sigma_1\rangle \otimes V_{\sigma_2} |\sigma_2\rangle = \sum_{\sigma_1, \sigma_2} C_{\sigma_1, \sigma_2} |\sigma_1\rangle \otimes |\sigma_2\rangle \quad (2.12)$$

where $\sigma_i \in \{\uparrow, \downarrow\}$. The coefficient C_{σ_1, σ_2} can be represented by a two component tensor:

$$C_{\sigma_1, \sigma_2} = \begin{pmatrix} ac & ad \\ bc & bd \end{pmatrix}. \quad (2.13)$$

Similarly, for a system of L lattice sites and d local states, the coefficient becomes an L -index tensor, thus, the corresponding wavefunction is given by

$$|\Psi\rangle = \sum_{\sigma_1, \dots, \sigma_L} C_{\sigma_1 \dots \sigma_L} |\sigma_1\rangle \otimes \dots \otimes |\sigma_L\rangle. \quad (2.14)$$

Using the MPS formalism we can split an L -index tensor into a series of local tensors. Thus, the coefficient can be re-written in terms of a product of local matrices A as

$$|\Psi\rangle = \sum_{\sigma_1, \dots, \sigma_L} \sum_{a_1, \dots, a_{L-1}} A_{a_1}^{\sigma_1} A_{a_1 a_2}^{\sigma_2} \dots A_{a_{L-2} a_{L-1}}^{\sigma_{L-1}} A_{a_{L-1}}^{\sigma_L} |\sigma_1, \dots, \sigma_L\rangle. \quad (2.15)$$

Here $|\sigma_1, \dots, \sigma_L\rangle$ stands for $|\sigma_1\rangle \otimes \dots \otimes |\sigma_L\rangle$ and a_i 's represent the virtual or bond indices whereas σ_i 's denote the physical indices. For a site l the tensor $M_{a_{l-1}, a_l}^{\sigma_l}$ contains d matrices of dimension $a_{l-1} \times a_l$, except at the first and last site where they are just vectors of dimension $1 \times a_1$ and $a_{L-1} \times 1$, respectively.

2.2.1 Singular value decomposition

Singular value decomposition (SVD) is a mathematical tool to manipulate tensor network states. Using this method, one can write a rectangular matrix M of dimension $m \times n$ as

$$M = USV^\dagger, \quad (2.16)$$

where U is a unitary matrix of dimension $m \times \min(m, n)$ and has orthogonal columns ($U^\dagger U = I$). Similarly, V is another unitary matrix of dimension $\min(m, n) \times n$ but with orthogonal rows ($VV^\dagger = I$). S is known as a singular matrix which contains diagonal entries only.

For a system where the bases are split into two blocks A and B, a corresponding state can be written using the SVD as

$$|\psi\rangle = \sum_{i,j} \Psi_{i,j} |\sigma_i\rangle_A |\sigma_j\rangle_B = \sum_{i,j,a} U_{ia} S_{aa} V_{aj}^\dagger |\sigma_i\rangle_A |\sigma_j\rangle_B. \quad (2.17)$$

Here $|\sigma_i\rangle_A$ and $|\sigma_i\rangle_B$ are orthonormal bases of A and B, respectively and the SVD has been applied to the coefficient matrix $\Psi_{i,j}$. We call this process as Schmidt decomposition.

2.2.2 Canonical form

As shown above, any state with an L -index tensor $C_{\sigma_1 \dots \sigma_L}$ can be re-written in terms of the MPS formalism. The conversion of a coefficient tensor into an MPS goes as follows: first, we reshape the tensor to a matrix $C'_{\sigma_1, (\sigma_2 \dots \sigma_L)}$ and then split the matrix into two by performing SVD.

$$C_{\sigma_1 \dots \sigma_L} = C'_{\sigma_1, (\sigma_2 \dots \sigma_L)} = \sum_{a_1} U_{\sigma_1, a_1}^{[1]} S_{a_1, a_1}^{[1]} V_{a_1, (\sigma_2, \dots, \sigma_L)}^{\dagger [1]} \quad (2.18)$$

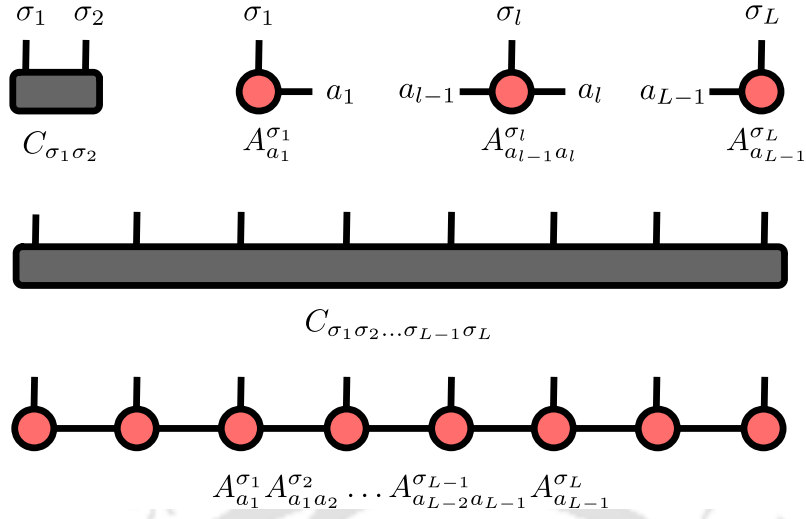


Figure 2.1: Top row from left to right shows the coefficient of the wavefunction of a two-site lattice, A matrix in the left end, A matrix in the bulk and A matrix in the right end of the lattice of L sites. The middle figure represents an L -index coefficient tensor and the bottom figure shows the matrix product representation.

Now, we reshape $U_{\sigma_1, a_1}^{[1]}$ into $A_{a_1}^{\sigma_1}$ and contract $S_{a_1, a_1}^{[1]}$ with $V_{a_1, (\sigma_2, \dots, \sigma_L)}^{\dagger[1]}$.

$$C_{\sigma_1 \dots \sigma_L} = \sum_{a_1} A_{a_1}^{\sigma_1} C_{a_1}^{\sigma_2 \dots \sigma_L} \quad (2.19)$$

The tensor involving physical indices other than σ_1 can be reshaped into a matrix $C_{a_1 \sigma_2, (\sigma_3 \dots \sigma_L)}^{[2]}$ and split by SVD

$$\begin{aligned} C_{\sigma_1 \dots \sigma_L} &= \sum_{a_1} A_{a_1}^{\sigma_1} \sum_{a_2} U_{a_1 \sigma_2, a_2}^{[2]} S_{a_2, a_2}^{[2]} V_{a_2, (\sigma_3, \dots, \sigma_L)}^{\dagger[2]} \\ &= \sum_{a_1, a_2} A_{a_1}^{\sigma_1} A_{a_1, a_2}^{\sigma_2} C_{a_2}^{\sigma_3 \dots \sigma_L} \end{aligned} \quad (2.20)$$

where again, the $U_{a_1 \sigma_2, a_2}^{[2]}$ matrix is reshaped to $A_{a_1, a_2}^{\sigma_2}$ and $S_{a_2, a_2}^{[2]}$ and $V_{a_2, (\sigma_3, \dots, \sigma_L)}^{\dagger[2]}$ matrices are contracted together to form $C_{a_2}^{\sigma_3 \dots \sigma_L}$.

The above procedure can be repeated for the whole system of L sites as

$$C_{\sigma_1 \dots \sigma_L} = \sum_{\sigma_1, \dots, \sigma_L} \sum_{a_1, \dots, a_{L-1}} A_{a_1}^{\sigma_1} A_{a_1, a_2}^{\sigma_2} \dots A_{a_{L-2}, a_{L-1}}^{\sigma_{L-1}} A_{a_{L-1}}^{\sigma_L}, \quad (2.21)$$

which is known as left-canonical form. Since we obtained this representation from U matrices of the SVD, it turns out to be left-normalized. Fig. 2.2 shows the procedure

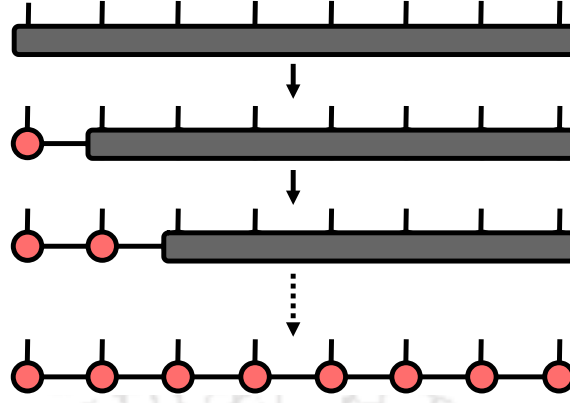


Figure 2.2: The iterative construction of a matrix product state from an arbitrary state is represented graphically.

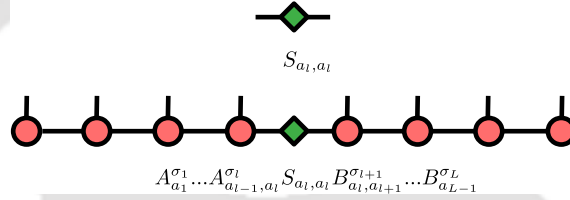


Figure 2.3: The top figure shows a singular matrix corresponding to l th lattice site. An MPS in mixed-canonical form is shown in the bottom figure.

to convert an arbitrary wavefunction into a left-canonical MPS. Similarly, we can represent a state in right canonical form, which is right-normalized, by reshaping the V^\dagger matrix into a B matrix and contracting U and S matrices together. A right canonical MPS is given by

$$C_{\sigma_1 \dots \sigma_L} = \sum_{\sigma_1, \dots, \sigma_L} \sum_{a_1, \dots, a_{L-1}} B_{a_1}^{\sigma_1} B_{a_1 a_2}^{\sigma_2} \dots B_{a_{L-2} a_{L-1}}^{\sigma_{L-1}} B_{a_{L-1}}^{\sigma_L}. \quad (2.22)$$

A state represented by both A and B matrices, with a singular matrix S in between, is known as mixed-canonical MPS (see Fig. 2.4). Here the left side (from first to l th site) is left-normalized whereas the right side (from the l th site to the last site) is right-normalized. A general mixed-canonical MPS is given by

$$|\Psi\rangle = \sum_{a_1, \dots, a_L} A_{a_1}^{\sigma_1} \dots A_{a_{l-1}, a_l}^{\sigma_{l-1}} S_{a_l, a_l} B_{a_l, a_{l+1}}^{\sigma_l} \dots B_{a_{L-1}}^{\sigma_{L-1}} |\sigma_1, \dots, \sigma_L\rangle. \quad (2.23)$$

Now that we are familiar with the MPS approach, we can easily compute the overlap or inner product of an MPS and the expectation value of an operator quite easily [40]. Suppose, we have two MPSs in left-canonical form, $|\Psi\rangle$ and $|\Phi\rangle$ which are

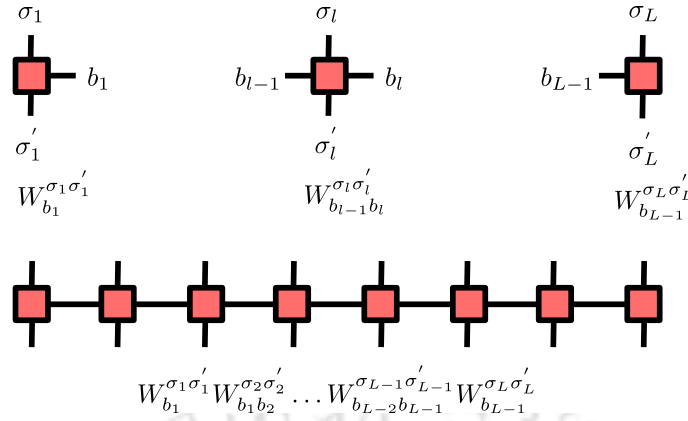


Figure 2.4: The top row from left shows the W matrices for the left end, bulk and the right end. The bottom figure shows the graphical representation of a matrix product operator.

composed of A^{σ_i} and \tilde{A}^{σ_i} matrices, respectively. Here the indices a_i are hidden for convenience. Thus, the overlap between these two can be computed by contracting the common indices from one end of the lattice to the other end as

$$\langle \Phi | \Psi \rangle = \sum_{\sigma_L} \tilde{A}^{\sigma_L \dagger} \left(\dots \left(\sum_{\sigma_2} \tilde{A}^{\sigma_2 \dagger} \left(\sum_{\sigma_1} \tilde{A}^{\sigma_1 \dagger} A^{\sigma_1} \right) A^{\sigma_2} \right) \dots \right) A^{\sigma_L} \quad (2.24)$$

Similarly, the expectation value of an operator corresponding to a wavefunction $|\Psi\rangle$ can be calculated using a similar approach. An L -site operator O is usually represented as the tensor product of L onsite operators as $O = O_1 \otimes O_2 \otimes \dots \otimes O_L$. Now we can compute the expectation value of the operator using the formula

$$\langle \Psi | O | \Psi \rangle = \sum_{\sigma_L \sigma'_L} O_L^{\sigma_L \sigma'_L} A^{\sigma_L \dagger} \left(\dots \left(\sum_{\sigma_2 \sigma'_2} O_2^{\sigma_2 \sigma'_2} A^{\sigma_2 \dagger} \left(\sum_{\sigma_1 \sigma'_1} O_1^{\sigma_1 \sigma'_1} A^{\sigma_1 \dagger} A^{\sigma'_1} \right) A^{\sigma_2 \dagger} \right) \dots \right) A^{\sigma'_L}. \quad (2.25)$$

2.2.3 Matrix product operator (MPO)

Next, we discuss the idea of matrix product operator (MPO) which is based on the MPS-like formalism. An operator O , in general, is written as

$$O = \sum_{\sigma_1, \dots, \sigma_L} \sum_{\sigma'_1, \dots, \sigma'_L} O_{\sigma_1 \sigma'_1 \dots \sigma_L \sigma'_L} |\sigma_1, \dots, \sigma_L\rangle \langle \sigma'_1, \dots, \sigma'_L|. \quad (2.26)$$

An MPO can be constructed from this by using a similar approach of reshaping-

SVD-resaping for the MPS derivation. A typical MPO is represented as

$$O = \sum_{\sigma_1, \dots, \sigma_L} \sum_{\sigma'_1, \dots, \sigma'_L} W_{b_1}^{\sigma_1 \sigma'_1} W_{b_1 b_2}^{\sigma_2 \sigma'_2} \dots W_{b_{L-2} b_{L-1}}^{\sigma_{L-1} \sigma'_{L-1}} W_{b_{L-1}}^{\sigma_L \sigma'_L} |\sigma_1, \dots, \sigma_L\rangle \langle \sigma'_1, \dots, \sigma'_L|. \quad (2.27)$$

Notice that the W_i 's are four-index tensors with bond indices b_i . The Hamiltonian H of a given model can be represented as an MPO and thus, one can compute the eigenvalues by using the formula $\langle \Psi | H | \Psi \rangle$. This can be done by contracting the common indices of the MPSs and MPO iteratively from one end of the lattice. However, here the Hilbert space size still grows exponentially if the system size increases. In the following we provide the details of the DMRG algorithm which solves this problem and efficiently computes the ground state.

2.3 Density matrix renormalization group (DMRG)

Two of the convenient methods for solving one-dimensional models are Wilson's numerical renormalization group (NRG) method [41, 42] and the density matrix renormalization group (DMRG) method devised by S.R. White [43]. Both NRG and DMRG are numerical methods that reduce the size of this Hilbert space to a point that computations become easier, while retaining the necessary information regarding the low energy eigenstates. The NRG algorithm works by tracing out the higher energy scales of the system but keeping the low energy states. However, this procedure does not work properly for most lattice problems. It turns out that the solution of getting a successful procedure for a one dimensional lattice system lies in the density matrix projection. Instead of using the lowest m eigenstates to truncate the Hamiltonian matrix at each step, DMRG uses the lowest m eigenstates of the ground state density matrix to perform the truncation.

The DMRG procedure is usually divided into the infinite and finite algorithms. The infinite algorithm is used to grow a superblock up to a certain size, whereas the finite algorithm acts upon the superblock to accurately obtain the ground state of the system. However, in the MPS formalism we use the former to obtain a random MPS and the latter is used to obtain the ground state with a desired accuracy.

Using variational approach the ground state is obtained by minimizing the energy functional

$$E_g = \frac{\langle \Psi_g | H | \Psi_g \rangle}{\langle \Psi_g | \Psi_g \rangle} \leq \frac{\langle \Psi | H | \Psi \rangle}{\langle \Psi | \Psi \rangle}. \quad (2.28)$$

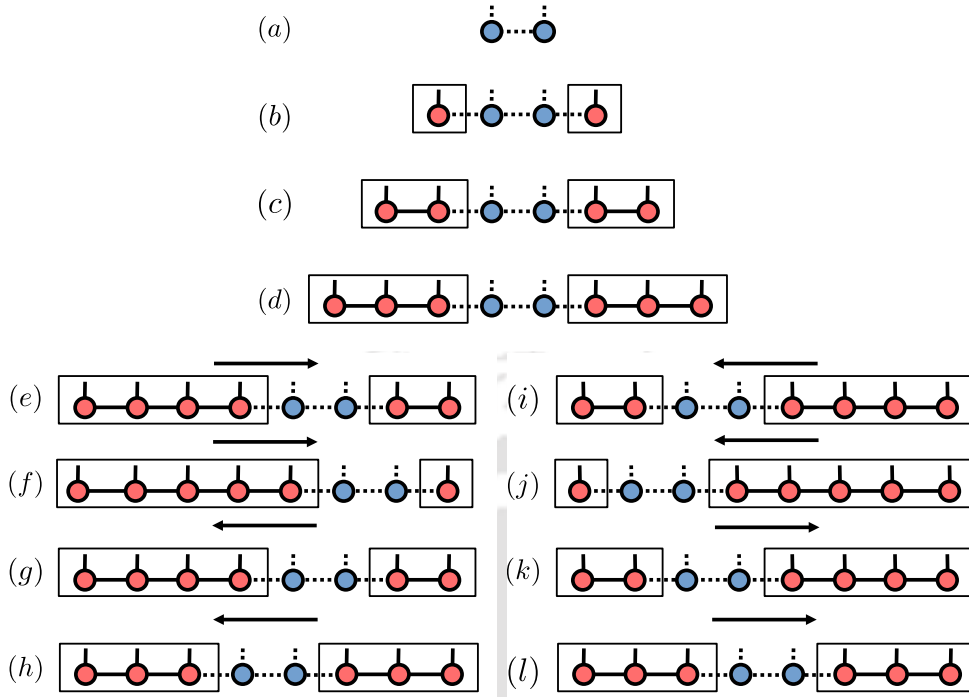


Figure 2.5: The graphical representation of the DMRG method using MPS formalism. Here (a-d) represent the infinite DMRG algorithm and (e-l) represent the finite DMRG algorithm. The arrow sign shows the direction of the sweeping process.

So in the so called two-site DMRG process the Hamiltonian is written as

$$H = \sum_k H_L^k \otimes H_{i,j}^k \otimes H_R^k. \quad (2.29)$$

Here the total Hamiltonian is divided into the left and the right blocks which are also known as the system parts. Now the local minimization becomes an eigenvalue problem like

$$\tilde{H}_{a\sigma_i\sigma_jb}^{a'\sigma'_i\sigma'_jb'} X_{a'\sigma'_i\sigma'_jb'} = E X_{a'\sigma'_i\sigma'_jb'}, \quad (2.30)$$

where

$$\tilde{H}_{a\sigma_i\sigma_jb}^{a'\sigma'_i\sigma'_jb'} = \sum_k (\tilde{H}_R^k)_a^{a'} (\tilde{H}_L^k)_b^{b'} (H_{i,j}^k)_{\sigma_i\sigma_j}^{\sigma'_i\sigma'_j} \quad (2.31)$$

Here \tilde{H}_R^k and \tilde{H}_L^k can be derived from the previous step and $X_{a'\sigma'_i\sigma'_jb'}$ is basically the local wavefunction. The above eigenvalue problem can be solved using the Lanczos algorithm which is described above. In the DMRG method we use the wavefunction of a particular and proceed with it as a guess for the next step. Thus, the MPS can be computed from $X_{a\sigma_i\sigma_jb}$ with a truncation in the bond dimension during the SVD

process.

Now, we provide the algorithm for the conventional two-site DMRG method using MPS formalism.

Step-1: Start with two active sites on the edges, i.e. on sites 1 and L along with the corresponding MPO tensors for each site W_1 and W_L . Build the Hamiltonian matrix from these MPO tensors and dummy left block $L[1]$ and dummy right block $R[L]$. Diagonalize the Hamiltonian using the Lanczos method and obtain the ground state wavefunction Ψ . Then perform an SVD on Ψ , reshape U and store it as A^{σ_1} and V^\dagger as B^{σ_L} .

Step-2: Keeping in mind that the left (right) virtual index of site 1 (L) is dummy, build the blocks $L[2]$ and $R[L-1]$ from the new A and B tensors and the corresponding MPO tensors. The matrix of singular values S is discarded to preserve normalization before introducing two more sites 2 and $L-1$.

Step-3: Run the remaining infinite algorithm with the same procedure as the above step. Insert two sites, build Hamiltonian matrix, diagonalize it and find Ψ . Then perform SVD but reshape it only with χ left-singular vectors with largest singular values of U to A^{σ_i} and similarly reshape the χ right-singular vectors of V^\dagger to $B^{\sigma_{L+1-i}}$. This procedure of truncating the size of the MPS tensors and setting the bond dimension as χ is called as an SVD compression. After the final iteration set the last S matrix to an identity for normalization. This will result in a MPS state with bond dimension χ . The truncation procedure described here is similar to the truncation of density matrix basis in the classical DMRG method and the bond dimension χ is analogous to the number of eigenstates m . The end of infinite algorithm leaves a mixed-canonical MPS of length L , where the left hand side of the chain is composed of left-normalized tensors (A) and the right hand side is composed of right-normalized tensors (B).

Step-4: Begin the finite DMRG algorithm by sweeping from the middle of the chain with $i = (L/2) + 1$. Construct the effective Hamiltonian as before from $L[i]$, $R[i+1]$, $W[i]$ and $W[i+1]$ tensors. Then diagonalize it to obtain Ψ , upon which perform an SVD. Reshape U to A^{σ_i} , contract S and V^\dagger with $B^{\sigma_{i+1}}$ and reshape to provide a guess for the next diagonalization step. Repeat this until $i = L-1$ where the right end of the lattice is reached. For left sweep repeat the same sequence except after diagonalization and SVD, reshape V^\dagger to $B^{\sigma_{i+1}}$ and contract $A^{\sigma_{i-1}}$ with U and S to provide the guess for the next iteration. Repeat it until $i = L-1$ where the left end of the lattice is reached. Perform right and left sweeps until convergence is achieved with desired accuracy.



Chapter 3

Symmetry protected topological phase through dimerized interactions

3.1 Introduction

The study of topological phases and phase transitions has been a topic of paramount interest in recent years [8]. Starting from the seminal observation of quantized Hall conductance in quantum Hall states [7], enormous progress has been made to understand the topological phases of matter [44] which do not belong to the conventional Landau theory of phase transition. Characterized by non-trivial physical properties and non-local correlations, topological phases are extremely important in the context of fundamental science and technological applications [45–49].

There exists a different class of topological phases of matter, known as the symmetry protected topological (SPT) phases [50, 51] which are protected by certain underlying symmetry(ies). Characterised by a finite bulk excitation gap and gapless edge/surface modes, the SPT phases are fundamentally known to be robust against small perturbations. Any transition to another gapped phase due to strong perturbation requires the closing of the excitation gap. Due to their simplest single particle classification, the SPT phases and transitions have been very well understood in the context of topological insulators and superconductors [8, 44]. One of the simplest models that exhibits an SPT phase is the one dimensional Su-Schrieffer-Heeger (SSH) model [12] which has been simulated in recent experiments using disparate systems [52–57].

Interactions on the other hand play important roles in stabilizing the SPT phases. While strong interaction is found to destroy the non-local order of the SPT phases in certain systems due to spontaneous symmetry breaking, a well defined topological

character can be favoured due to competing interaction and underlying topology in certain systems such as the Haldane phase. Several recent studies based on the fermionic SSH models have also revealed that the SPT phases are robust against weak to moderate interaction strength. Moreover, strong interactions may as well favour the SPT phases under proper conditions which have been discussed both in the fermionic as well as bosonic interacting SSH models. Recent progress in simulating quantum phases using ultracold atoms has allowed the successful realization of such SPT phases [58, 59].

The presence of interaction usually complicates the study of quantum mechanical systems due to the deviation from single particle perspective and the requirement of a pure many-body description. Interactions can either destroy the topology present in the non-interacting limit or they can go hand in hand to produce a new topological phase altogether. In this chapter, we study two one-dimensional models to show whether a topological phase can be realized solely due to interaction or not.

3.2 Model and approach

For our studies we consider a system of one dimensional nearest-neighbour interacting hardcore bosons with particle-hole symmetry described by the model

$$\begin{aligned}
 H = & -t \sum_i (a_i^\dagger a_{i+1} + \text{H.c.}) \\
 & + V_1 \sum_{i \in \text{odd}} \left(n_i - \frac{1}{2}\right) \left(n_{i+1} - \frac{1}{2}\right) \\
 & + V_2 \sum_{i \in \text{even}} \left(n_i - \frac{1}{2}\right) \left(n_{i+1} - \frac{1}{2}\right). \tag{3.1}
 \end{aligned}$$

Here, $a_i^\dagger(a_i)$ is the creation (annihilation) operator of the particles at site i . V_1 and V_2 are the NN interactions between alternate bonds. We consider dimerized interactions which is achieved by setting $V_1 \neq V_2$. When $V_1 = V_2$ ($V_1 \neq V_2$), we call the system symmetric (dimerized). Note that the model shown above can be mapped to spin polarized fermions and spins under proper transformations [60], hence, the observables considered for our studies possess identical behaviour for all the three cases. We perform the simulations using the density matrix renormalization group (DMRG) method where we consider up to 500 bond dimensions. Our focus is on the physics at half filling i.e. $\rho = N/L = 0.5$, where N and L are the number of particles and system size respectively. We have considered system sizes up to

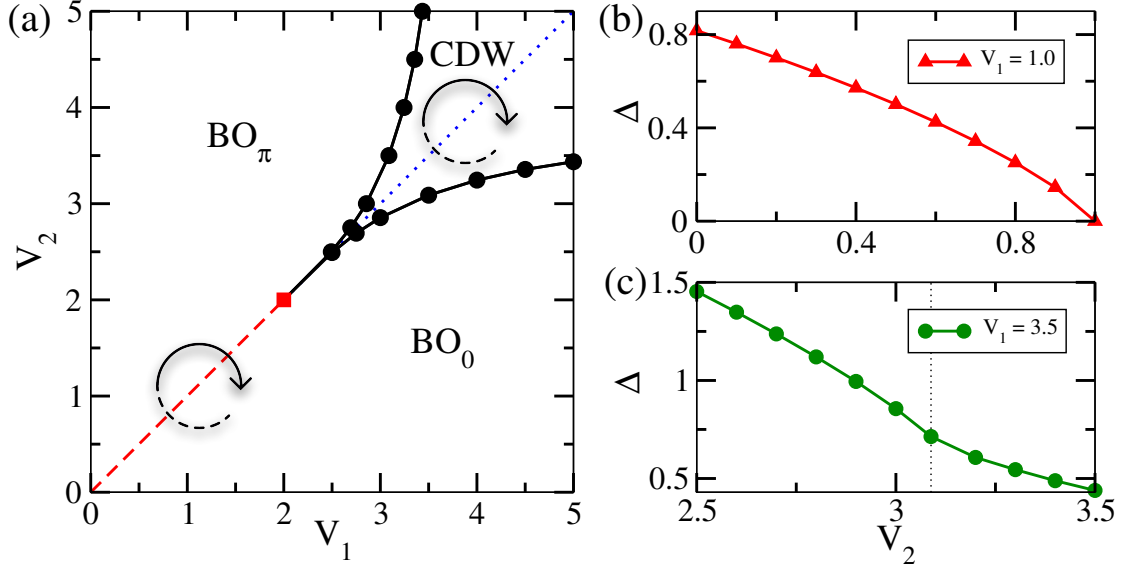


Figure 3.1: (a) The phase diagram of model (3.1) in $V_1 - V_2$ plane. The red dashed (blue dotted) line represents the gapless SF (gapped CDW) phase at $V_1 = V_2$. The SF-CDW critical point is marked by the solid red square. The black solid circles represents the boundary between the BO and the CDW phases. The arrow directions in (a) show the pumping protocols. Here θ in BO_θ is the associated Berry phase. (b) and (c) show the extrapolated gap at $V_1 = 1.0$ and 3.5 respectively with varying V_2 . The thin dotted line in (c) marks the BO-CDW transition point.

$L = 700$ to avoid finite size effects and set $t = 1$ as the energy scale of the system.

It is well known that at half filling ($\rho = 0.5$) the model(3.1) in the symmetric interaction limit i.e. $V_1 = V_2 = V$, is the well known $t - V$ model which exhibits a gapless superfluid (SF) to a gapped charge density wave (CDW) phase transition at the critical point $V = 2t$. In this chapter we show that by moving away from this symmetric limit (i.e. for finite dimerization) interesting features appear in the phase diagram leading to the topological phase transition which will be discussed in detail in the following.

3.3 Results

3.3.1 Phase diagram

Before discussing the topological aspects of our studies, we first present the complete ground state phase diagram of the model (3.1) obtained using our DMRG

simulations in Fig. 3.1(a). As already mentioned before, when $V_1 = V_2$, a transition takes place from the gapless SF phase (red dashed line) to the gapped CDW phase (blue dotted line) at the critical point $V_1 = V_2 = 2$ denoted as the red solid square in Fig. 3.1(a). Interestingly, starting from the SF region, as soon as the dimerization is turned on i.e. when $V_1 \neq V_2$, the system immediately becomes gapped. However, the gap which exists at $V_1 = V_2 > 2$ remains finite as a function of dimerization. In Fig. 3.1, we plot the extrapolated values of the charge gap [60]

$$\Delta_{L \rightarrow \infty} = E(L, N + 1) + E(L, N - 1) - 2E(L, N) \quad (3.2)$$

as a function of V_2 at two different cuts through the phase diagram i.e. at $V_1 = 1.0$ (Fig. 3.1(b)) and $V_1 = 3.5$ (Fig. 3.1(c)). Here E is the ground state energy of the system. The behaviour of $\Delta_{L \rightarrow \infty}$ clearly shows that for $V_1 = 1$, the gap closes exactly at $V_2 = 1$ and remains finite otherwise. On the other hand for $V_1 = 3.5$, the gap always remains finite as a function of V_2 . These features indicate that the regions depicted in the entire phase diagram are gapped except the SF phase (red dashed line) at $V_1 = V_2$.

Interestingly, the gapped regions immediately below and above the symmetric line (where $V_1 \neq V_2$) up to $V_1 = V_2 = 2$ (red square in Fig. 3.1) are found to possess finite bond ordering induced by the NN interaction exhibiting finite oscillation in the bond kinetic energy $B_i = a_i^\dagger a_{i+1} + H.c.$ with i denoting the site index. On the other hand, in the limit of strong interactions i.e. $V_1 = V_2 > 2$, the CDW nature is found to remain stable up to certain range of dimerization before the system undergoes a transition to the BO phase. While the BO phases are characterized by a finite peak in the bond order structure factor

$$S_{BO}(k) = \frac{1}{L^2} \sum_{i,j} e^{ikr} \langle B_i B_j \rangle, \quad (3.3)$$

the CDW phase is characterized by a finite peak in the density structure factor

$$S(k) = \frac{1}{L^2} \sum_{i,j} e^{ikr} (\langle n_i n_j \rangle - \langle n_i \rangle \langle n_j \rangle). \quad (3.4)$$

In Fig. 3.2 we compare the behaviour of the finite size extrapolated values of $S_{BO}(\pi)$ and $S(\pi)$ by plotting them as a function of V_2 at two different cuts through

the phase diagram i.e. $V_1 = 1.0$ and 3.5 . It is clearly seen from Fig. 3.2(a) that for $V_1 = 1$, the $S_{BO}(\pi)$ remains finite for all the values of V_2 except at the symmetric point $V_1 = V_2 = 1$ where $S_{BO}(\pi)$ vanishes. However, for the cut through $V_1 = 3.5$, there is a clear indication of transition between the BO and the CDW phases at a critical V_2 as shown in Fig. 3.2(b). The BO - CDW phase transition is found to follow the Ising universality class and the critical points are obtained by using appropriate scaling behaviour of the CDW structure factor

$$S(\pi)L^{2\beta/\nu} = F((V_2 - V_2^c)L^{1/\nu}) \quad (3.5)$$

where β and ν are the critical exponents [60]. In Fig. 3.2(c) we plot $S(\pi)L^{2\beta/\nu}$ as a function of V_2 for $V_1 = 3.5$ with $\beta = 1/8$ and $\nu = 1$. The curves for different system sizes cross at the critical point which is found to be $V_2^c \sim 3.09$. Now by using the scaling function shown in Eq. 3.5 a perfect data collapse is obtained with $V_2^c = 3.09$ as shown in Fig. 3.2(d). Using this approach we trace out the entire CDW phase which is flanked by the BO phases and the BO - CDW transition is marked by the black circles in Fig. 3.1(a). Note that the BO - CDW transition occurs in both the regimes of dimerization i.e. $V_1 < V_2$ and $V_1 > V_2$. In the following we will show that the emergence of such bond order phases in such a simple model is responsible for the topological phase transition in the system.

3.3.2 Topological character

After discussing the bulk phase diagram of the model, in this part we discuss the topological character of these BO phases and the transition between them. As already highlighted in the bulk phase diagram, there exist two BO phases across the symmetric line of interaction. Here we show that these BO phases are topologically different from each other and a phase transition occurs between them through the gap closing point at $V_1 = V_2$ along the red dashed line that extends up to $V_1 = V_2 = 2$ in the phase diagram of Fig. 3.1.

As a first signature to distinguish between the two BO phases, we examine the edge properties of a finite system in search of the degenerate zero energy edge states which are the typical character of the topological insulators. To this end we plot the real space onsite particle numbers at each site for $V_1 > V_2$ (black circles) and $V_1 < V_2$ (red squares) in Fig. 3.3(a). The polarized edge population for $V_1 < V_2$ in the figure indicates the topological character of the BO phase. To further quantify this feature we compute the Berry phase (γ) as the topological invariant in such

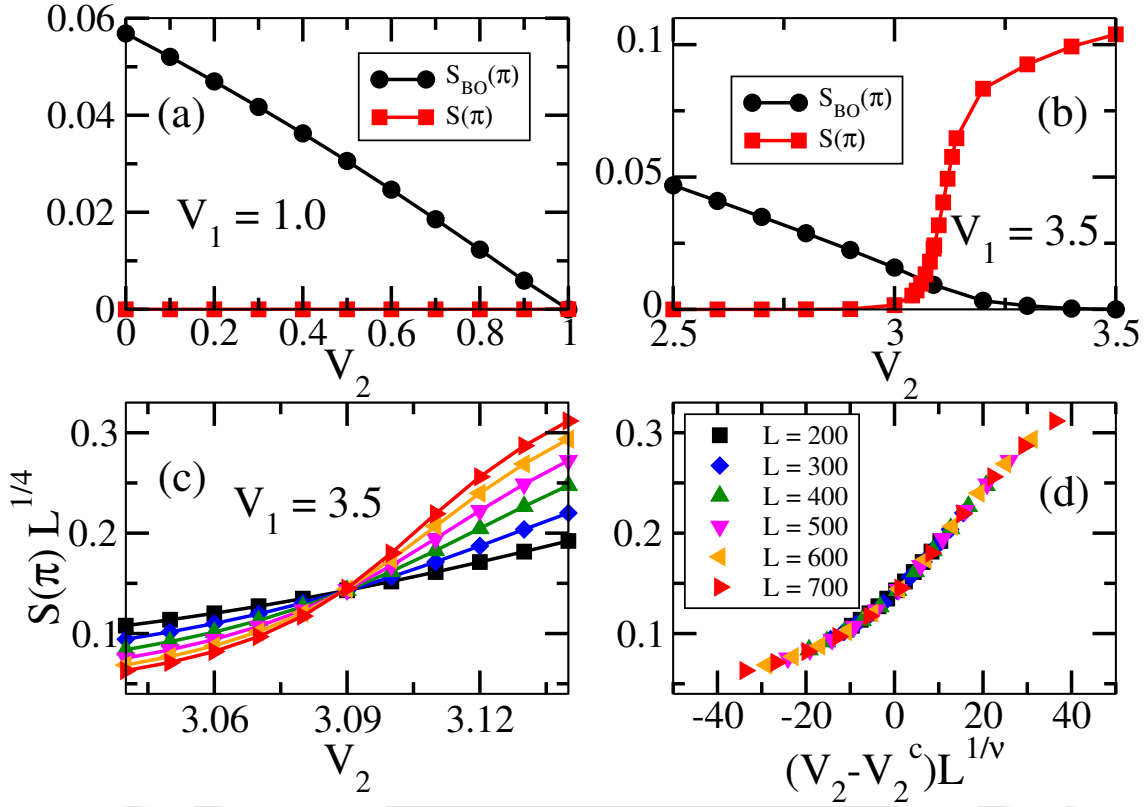


Figure 3.2: (a) and (b) show the behavior of $S_{BO}(\pi)$ (black circles) and $S(\pi)$ (red squares) with varying V_2 for cuts through $V_1 = 1.0$ and 3.5 respectively in the phase diagram. (c) The finite-size scaling of $S(\pi)$ is shown for different values of L at $V_1 = 3.5$ with varying V_2 . The crossing of the curves for different L at a point represents the BO-CDW transition. (d) Scaled $S(\pi)$ is plotted against the scaled V_2 showing the collapse of all points onto a single curve and thus confirming $V_2^c = 3.09$ as the transition point.

interacting system. By using the twisted boundary condition [61, 62] i.e. by setting $a_i \rightarrow e^{i\phi/L} a_i$ and by varying the twist angle ϕ from 0 to 2π the Berry phase can be computed as

$$\gamma = \int_0^{2\pi} d\phi \langle \psi(\phi) | \partial_\phi \psi(\phi) \rangle. \quad (3.6)$$

We calculate γ for small systems of size up to $L = 12$ sites using the exact diagonalization (ED) method and plot them with respect to V_2 for $V_1 = 1.0$ in Fig. 3.3(b). The discontinuous jumps from $\gamma = 0$ to $\gamma = \pi$ at $V_1 = 1$ for all lengths indicate a clear signature of topological phase transition. With this distinction, we classify the BO phases below and above the symmetric line as trivial and topological BO phases denoted by BO_0 and BO_π phases respectively as depicted in the phase diagram of Fig. 3.1(a).

Furthermore, we show that the topological BO_π phase is found to exhibit a non-

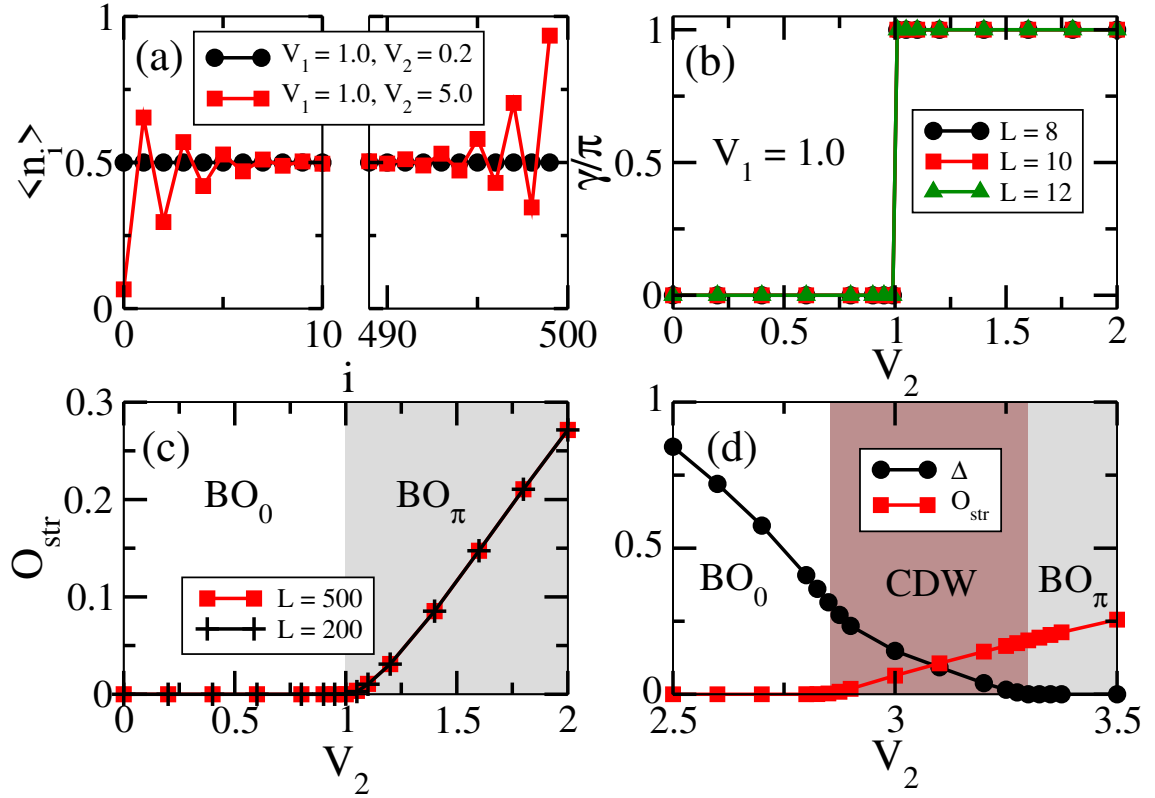


Figure 3.3: (a) Onsite particle densities $\langle n_i \rangle$ vs i are plotted in the BO_0 (black circle) and BO_π (red squares) phases. (b) The Berry phase γ/π for different lengths $L = 8, 10, 12$ obtained using the ED method is plotted as a function of V_2 across the topological phase transition at $V_1 = 1.0$. (c) O_{str} vs V_2 for $V_1 = 1.0$ are plotted for $L = 500$ (red squares) and $L = 200$ (black plus) where the effective topological phase transition is valid. (d) The extrapolated values of Δ (black circles) and O_{str} for $L = 400$ are plotted as a function of V_2 for $V_1 = 3.0$. The finite (vanishing) values of O_{str} (Δ) after $V_2 = 3.3$ indicate a transition to the BO_π phase.

local string order which can be quantified by the string order parameter [63–65] defined as

$$O_{str}(r) = -\langle z_i e^{i\frac{\pi}{2} \sum_{k=i+1}^{j-1} z_k z_j} \rangle, \quad (3.7)$$

where $z = 1 - 2a^\dagger a$ and $r = |i - j|$. To avoid the edge sites and to consider a maximum distance r , we chose $i = 2$ and $j = L - 1$ in Eq. 3.7.

We plot O_{str} as a function of V_2 for $V_1 = 1.0$ in Fig. 3.3(c) for two different lengths such as $L = 200$ (black plus) and 500 (red squares) which becomes finite after the critical point of transition i.e. at $V_1 = V_2$. This feature clearly indicates the existence of a non-local string order in the BO_π phase and is an important signature which distinguishes the two BO phases having the same bulk properties in the regimes of $V_1 > V_2$ and $V_1 < V_2$. However, across the transition through the

CDW phase, due to construction, the O_{str} is expected to be finite in the CDW phase as well which can be seen in Fig. 3.3(d) where the O_{str} (red squares) is plotted as a function of V_2 for $V_1 = 3.0$.

Therefore, in order to distinguish the BO phases from the CDW phase in this case we plot the excitation gap Δ (black circles) as a function of V_2 which vanishes in the BO_π phase signifying the existence of gapless edge states. Comparing the values of O_{str} and Δ one can clearly separate the CDW phase (brown shaded region) from the two BO phases and the transition between them.

From the above discussion, it is evident that the presence of only dimerized interaction is sufficient to establish a topological BO phase and a topological phase transition. This topological phase transition is protected by the emergent bond inversion symmetry and the already assumed particle-hole symmetry of the system. An interesting inference which can be drawn from this analysis is that a topological transition is not possible between the two BO phases beyond the limit $V_1 = V_2 = 2$. This ambiguity can be attributed to the spontaneously broken translational as well as the bond inversion symmetry in the gapped CDW phase. Moreover, due to the particle-hole symmetry, the CDW phase also exhibits non-degenerate and energetic edge states (not shown) as mid gap states.

3.3.3 Experimental realization

In this part, we provide the possible signatures of the topological character of the BO_π phase in the context of the Thouless charge pumping (TCP) [66] which has been successfully observed in different experiments to characterise the topological nature of non-interacting systems [53, 54]. The recent generalization of the TCP to interacting systems are based on systems with finite hopping dimerization and are described by the Rice-Mele model [3, 67–69]. In general the pumping protocol relies on the adiabatic variation of a parameter which is responsible for the topological phase transition. Moreover, an additional symmetry breaking term that helps to keep the gap of the system open in the pumping cycle is a necessary condition. In the process the number of charge quanta pumped in a cycle reveals a topological invariant.

Here we propose a pumping protocol based on the Hamiltonian (Eq. 3.1) with

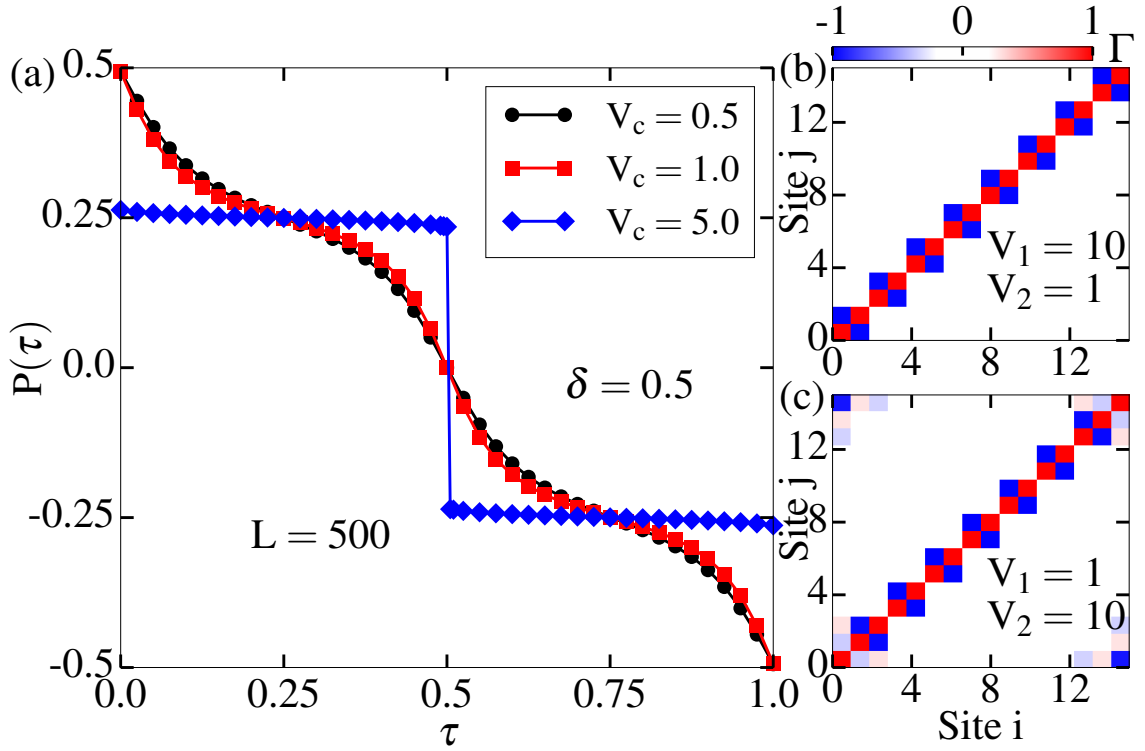


Figure 3.4: (a) Shows the evolution of polarization following a pumping cycle across three different critical points such as $V_c = 0.5$ (black circles), 1.0 (red squares) and $V_c = 5.0$ (blue diamonds) of the phase diagram in Fig. 3.1 obtained using the DMRG simulations. The density correlation matrix Γ obtained using the ED method is plotted for $L = 16$ sites in (b) for the BO_0 phase ($V_1 = 10.0, V_2 = 1.0$) and in (c) for the BO_π phase ($V_1 = 1.0, V_2 = 10.0$).

an additional symmetry breaking parameter Δ , given by

$$\begin{aligned}
 H_p = & -t \sum_i (a_i^\dagger a_{i+1} + \text{H.c.}) \\
 & + \sum_i (V_c - (-1)^i \delta \cos(2\pi\tau)) \left(n_i - \frac{1}{2}\right) \left(n_{i+1} - \frac{1}{2}\right) \\
 & + \Delta \sin(2\pi\tau) \sum_i (-1)^i n_i,
 \end{aligned} \tag{3.8}$$

where τ is the pumping parameter. The parameter Δ ensures that the gap remains open during the pumping cycle, especially at $\tau = 1/4$ and $3/4$. Note that in the limit $\Delta = 0$, the above Hamiltonian reduces to model 3.1 with $V_1 < V_2$ ($V_1 > V_2$) at $\tau = 0$ ($\tau = 1/2$). The V_c is the gap closing point that resides on the gapless line in the phase diagram of Fig. 3.1 when $\delta = \Delta = 0$ (i.e., $V_1 = V_2 = V_c$).

To study the TCP, we consider different values of V_c with $\delta = \Delta = 0.5$ and

compute the polarization given by

$$P(\tau) = \frac{1}{L} \sum_{i=0}^{L-1} \langle \psi(\tau) | (i - i_0) n_i | \psi(\tau) \rangle \quad (3.9)$$

where $i_0 = (L - 1)/2$. The total number of charge pumped during the pumping cycle is then given as

$$Q = \int_0^1 \partial_\tau P(\tau) d\tau. \quad (3.10)$$

Here $|\psi(\tau)\rangle$ is the ground state wavefunction for a particular value of τ . We compute $P(\tau)$ for a system of size $L = 500$ and plot them as a function of τ in Fig. 3.4(a) for $V_c = 0.5$ (black circles) and 1 (red squares). The continuous change of $P(\tau)$ from 0.5 to -0.5 indicates a robust charge pumping of one particle $Q = 1$ in a pumping cycle. However, for a critical $V_c = 5.0$ (blue diamonds) a clear breakdown of charge pumping is seen indicating no SPT transition. Furthermore, we also examine the density-density correlation matrix $\Gamma = \langle z_i z_j \rangle - \langle z_i \rangle \langle z_j \rangle$, which can be accessed in the quantum gas experiments [58] to distinguish between the trivial and the topological phases. The two isolated red points at the two opposite ends of the correlation matrix Γ in Fig. 3.4(c) clearly confirm the presence of the edge states in the BO_π phase that distinguishes it from the BO_0 phase (see Fig. 3.4(b)) where the edge states are absent.

In the remaining part of this chapter we extend our studies to a two-component system where we explore the topological properties of a one-dimensional two-component system where a topological phase can be induced in one component by the density dependent hopping or in other words, a bond-charge interaction.

3.4 Topological phase transition induced via density dependent hopping

We investigate a system of one-dimensional lattice consisting of two-component hardcore bosons $\{\uparrow, \downarrow\}$ where the first component leaves on a lattice with onsite staggered potential and the hopping of the second component depends upon the onsite particle density of the first one. The model Hamiltonian for this case is given

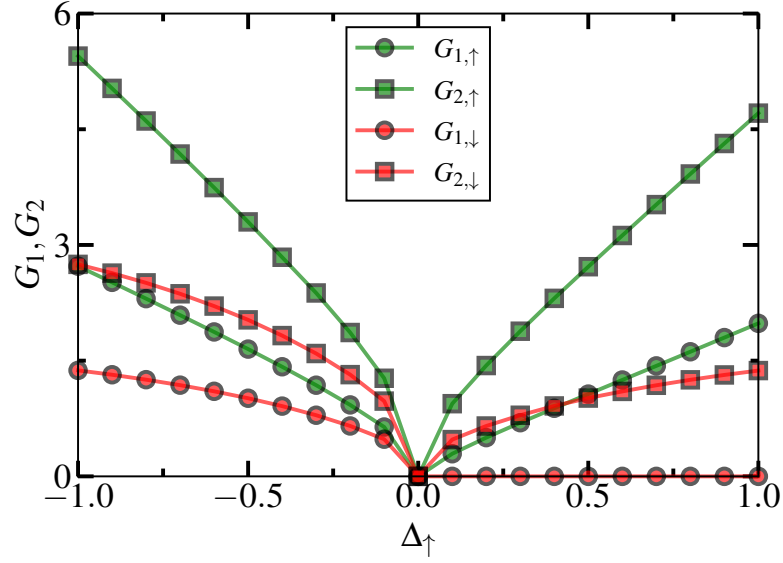


Figure 3.5: Single and two particle excitation energy gap for both the components as a function of Δ_{\uparrow} .

as

$$H = -t_{\uparrow} \sum_i (a_{i,\uparrow}^{\dagger} a_{i+1,\uparrow} + H.c.) + \Delta_{\uparrow} \sum_i (-1)^i n_{i,\uparrow} \quad (3.11)$$

$$-t_{\downarrow} \sum_i n_{i,\uparrow} (a_{i,\downarrow}^{\dagger} a_{i+1,\downarrow} + H.c.)$$

where $a_{i,\sigma}$ is the bosonic annihilation operator and $n_{i,\sigma}$ is the respective number operator at the i th lattice site for $\sigma \in (\uparrow, \downarrow)$. While t_{\uparrow} and Δ_{\uparrow} denote the hopping and staggered onsite potential strengths of the \uparrow -component, respectively, t_{\downarrow} fixes the hopping strength of the \downarrow -component. Here we set $t_{\uparrow} = t_{\downarrow} = 1$ as the energy scale and perform all the numerical simulations under open boundary conditions using the DMRG method.

We begin the analysis by looking at the ground state properties of the system at half-filling of both the components. Fig. 3.5 depicts the single and two particle excitation energy gaps as a function of Δ_{\uparrow} computed by using the formula

$$G_{1,\sigma} = E(N_{\sigma} + 1) + E(N_{\sigma} - 1) - 2E(N_{\sigma}) \quad (3.12)$$

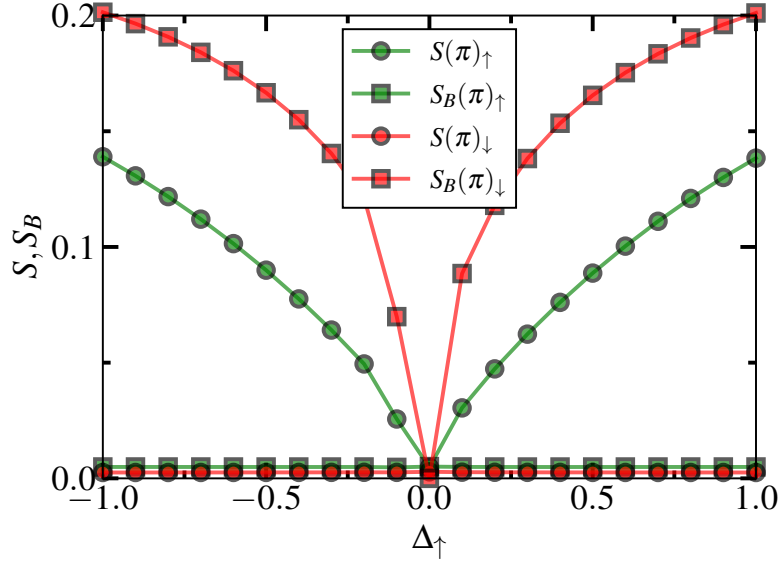


Figure 3.6: CDW and BO structure factors for both the components as a function of Δ_{\uparrow} .

and

$$G_{2,\sigma} = E(N_{\sigma} + 2) + E(N_{\sigma} - 2) - 2E(N_{\sigma}), \quad (3.13)$$

respectively. Here $E(N_{\sigma})$ is the ground state energy of the system with N particles for each component. From Fig. 3.5 we notice that the \uparrow -component is gapped for any finite value of Δ_{\uparrow} . On the other hand, for the \downarrow -component both the single and two particle gaps are finite for negative values of Δ_{\uparrow} . However, the vanishing single particle gap and finite two particle gap for positive Δ_{\uparrow} values signify the behaviour of a topological insulator. Therefore, the transition from one gapped phase without any zero energy modes to another gapped phase with zero energy modes via a gap-closing point as a function of Δ_{\uparrow} in the \downarrow -component can be called as a topological phase transition.

To understand the bulk properties of the system first, we compute the CDW and the BO structure factors using the formula

$$S(k)_{\sigma} = \frac{1}{L^2} \sum_{i,j} e^{ik|i-j|} \langle n_{i,\sigma} n_{j,\sigma} \rangle \quad (3.14)$$

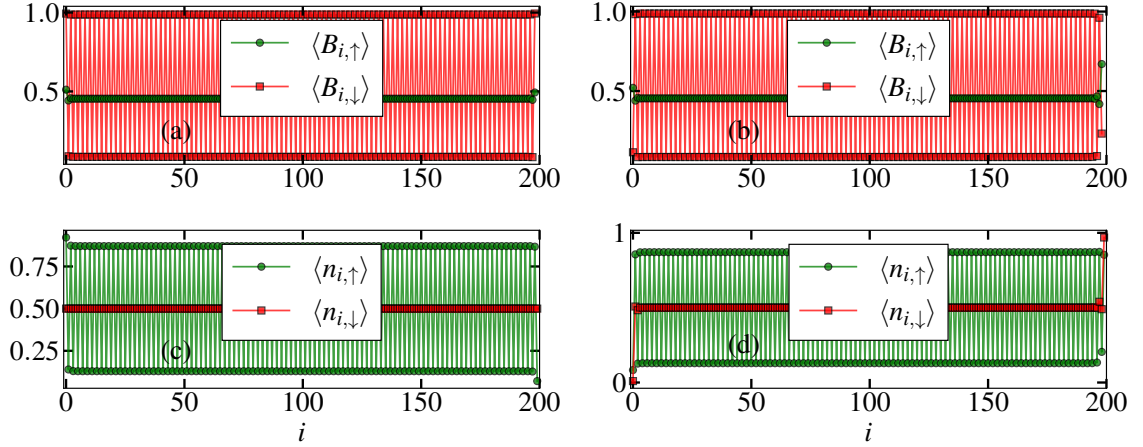


Figure 3.7: Onsite density and bond energy, respectively, for $\Delta_{\uparrow} = -1.0$ in (a) and (c) and $\Delta_{\uparrow} = 1.0$ in (b) and (d).

and

$$S_B(k)_{\sigma} = \frac{1}{L^2} \sum_{i,j} e^{ik|i-j|} \langle B_{i,\sigma} B_{j,\sigma} \rangle, \quad (3.15)$$

respectively, where $B_{i,\sigma} = a_{i,\sigma}^{\dagger} a_{i+1,\sigma} + H.c.$ is the bond energy associated to the i th bond of the component σ . In Fig. 3.6 the finite value of the CDW structure factor $S(k)$ and vanishing value of the bond order structure factor $S_B(k)$ in the gapped regions of \uparrow -component indicate the signature of a CDW phase. On the other hand, for the \downarrow -component S_B remains finite whereas $S(k)$ vanishes in the gapped regions, indicating a bond order phase. To extract more information on the CDW and the BO phases we plot the bond energies $\langle B_{i,\uparrow} \rangle$ and onsite densities $\langle n_{i,\uparrow} \rangle$ for $\Delta_{\uparrow} = -1.0$ in Fig. 3.7 (a) and (c), respectively and $\langle B_{i,\downarrow} \rangle$ and $\langle n_{i,\downarrow} \rangle$ for $\Delta_{\uparrow} = 1.0$ in Fig. 3.7 (b) and (d), respectively. We notice that there is a finite oscillation in the density (bond energy) of the \uparrow (\downarrow)-component for both $\Delta_{\uparrow} = -1.0$ and 1.0 . The oscillation in the density (bond energy) is a clear signature of a CDW (BO) phase. Interestingly, we notice further that for $\Delta_{\uparrow} = 1.0$ the \downarrow -component exhibits polarized edge states whereas such states are not present for $\Delta_{\uparrow} = -1.0$. Thus, the gapped phase of the \downarrow -component when $\Delta_{\uparrow} > 0$ ($\Delta_{\uparrow} < 0$) is a topological (trivial) insulator and the topological feature arises only when the density dependent hopping term becomes finite. The emergence of the topology and phase transition can be understood as follows. Due to the difference in chemical potential on alternate lattice sites, the particles in the \uparrow -component get trapped in the deeper sites, i.e. where Δ is negative. Moreover, the hopping in the \downarrow -component becomes finite along the i th bond only

if the density at the i th lattice site \uparrow -component is finite and thus, disconnected dimers are formed in \downarrow -component which is a limiting feature of the well known SSH model. Therefore, depending on whether the first site is empty or filled, the \downarrow -component exhibits gapless zero energy edge states.

3.5 Conclusions

We have shown that for a one-dimensional model of spinless fermions or hardcore bosons, a symmetry protected topological phase can be achieved by allowing only dimerized NN interactions while the hopping remains uniform. By extensive DMRG analysis we showed that a trivial to topological phase transition occurs as a function of dimerized interaction which stems from the emergent BO phases in the system. While there exists an SPT phase transition in the limit of weak NN interaction, for strong interaction, the two BO phases are separated by a gapped CDW phase indicating no SPT transition. The model considered in our analysis is one of the simplest systems to exhibit interaction induced topological phase transition and can be simulated using the ultracold dipolar atoms in optical lattice. Keeping this in mind, we provided possible experimental signatures of the topological phases in terms of Thouless charge pumping and density-density correlation function.

Furthermore, we also considered a one-dimensional two-component lattice and revealed that if the first component is a two-period superlattice then the hopping term in the second component which depends on the density of the first component, gives rise to a topological phase transition similar to the SSH model.

Our analysis provides a route to obtain interaction induced SPT phase transition for one dimensional spinless fermions or hardcore bosons without explicitly constraining the particle tunneling and thereby breaking the translational symmetry. These findings therefore provides interesting platforms to study the robustness of the topological character in presence of other perturbations. For example, an immediate extension can be to see the effect of diagonal disorder and frustrated next-nearest neighbour hoppings on the SPT phases. Furthermore, it would be interesting to explore the stability of the topological character by moving away from the one dimensional limit in coupled one dimensional lattices.

Chapter 4

Interacting bosons on a Su-Schrieffer-Heeger ladder

4.1 Introduction

In the past decade, a profusion of solid state, ultracold atomic, and metamaterial systems have realized topological phases of matter that beautifully conform to predictions made at the single-particle level. Particularly, the SSH model has offered the simplest platform to realize topological phase transition in low dimensional lattice systems [70, 71].

With well-established single-particle topological physics in place, attention has now turned to interaction effects. Naturally, the SSH model has formed a key subject for understanding how interactions modify its predicted topological phases [50]. Inter-particle interactions in the SSH model and its variants are known to have significant effects on the topological character [1, 3, 69, 72–82]. Moreover, interactions can even induce a topological phase and an associated phase transition [14, 83, 84].

On the other hand, two-leg ladders provide a minimal setup to explore the intermediate regime between one- and two-dimensional lattices. Thus, the topological properties of coupled SSH models have been theoretically investigated at the single particle level [85–91] and even realized experimentally [92]. The coupling between the chains, which forms the ladder, provides a degree of freedom to vary, and the possibility of new phases. The effect of interactions on this physics has been studied in many-body spin and fermionic systems [93, 94]. Many-body physics in bosonic SSH ladders is far from a simple extrapolation; competing effects offer hitherto unexplored regimes and form the subject of our study. Spinless fermions and hardcore bosons provide the same signature in the single particle limit. Moreover, in one di-

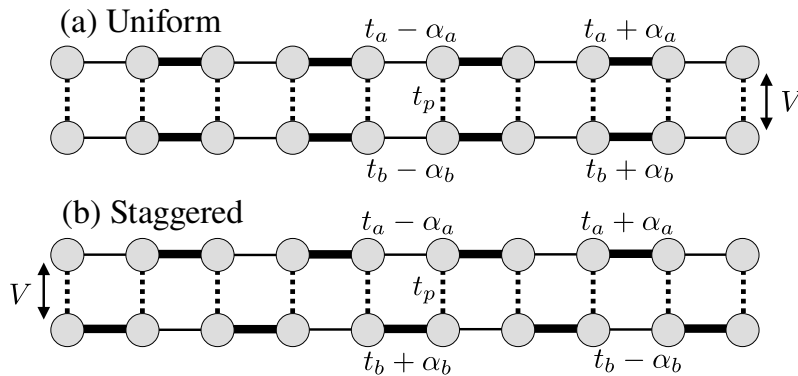


Figure 4.1: Two-leg ladder with different hopping dimerization patterns: (a) the uniform dimerization pattern, and (b) the staggered dimerization pattern. t_a , t_b and t_p are the hoppings along the leg-a, leg-b and along the rungs of the ladder. α_a and α_b decide the dimerization along leg-a and leg-b respectively. The circles represent the sites, and the thick (thin) bonds along the legs represent the strong (weak) hopping strengths. The dashed vertical lines illustrate the rung hopping. We allow inter-particle interaction V only along the rungs which is marked by the arrow.

mension both of them exhibit the same phase diagram in the many-body limit. However, once we deviate from the one dimension and move to a quasi-one-dimensional system like a coupled ladder system, the respective phase diagrams differ quite a bit due to the difference in statistics between fermions and bosons. While for the former, there exists a critical point of transition from a gapless to gapped phase when the inter-leg coupling is tuned, the latter exhibits a gapped phase for any finite value of the coupling [95]. Thus, it will be interesting to see whether the gapless zero-energy edge modes of the SSH model survive in presence of inter-leg coupling and interaction or not.

In this chapter, we perform an in-depth study of the topological nature of hardcore bosons on the two-leg SSH ladder in the presence of inter-leg interactions. We first review single-particle physics to set the stage for phenomena exhibited by interacting bosons. We establish how the most significant effects of topology come into play at half-filling, away from gapless superfluid phases that surround gapped phases in parameter space. On introducing inter-leg interactions, for the uniform ladder, we show how a ‘rung-Mott insulator’ phase can dictate and suppress the topological nature of the system. For the staggered ladder, starting from a topological phase at a fixed rung hopping, we show that the system sustains a robust topological phase with increasing inter-leg interactions until it reaches a critical strength at which it undergoes a phase transition to a trivial phase. We find that the topological phase transition is sensitive to the nature of the interaction, i.e., a topological to trivial

phase transition occurs at a smaller (larger) critical rung hopping when the interaction is repulsive (attractive). We do a careful study to quantify these topological properties by deriving and analyzing the excitation spectrum, finite edge polarization, quantized Berry phase, and Thouless charge pumping properties. Our studies show that the SSH bosonic ladder has a rich range of phases, is topologically robust, and has some features that are markedly different from its single-particle and fermionic counterparts.

4.2 Model and approach

The systems of interacting hardcore bosons on a two-leg SSH ladder studied here are described by the Hamiltonian

$$\begin{aligned} \mathcal{H} = & - \sum_j (t_a - (-1)^j \alpha_a) (a_j^\dagger a_{j+1} + \text{H.c.}) \\ & - \sum_j (t_b - (-1)^j \alpha_b) (b_j^\dagger b_{j+1} + \text{H.c.}) \\ & - t_p \sum_j (a_j^\dagger b_j + \text{H.c.}) + V \sum_j n_{aj} n_{bj} \end{aligned} \quad (4.1)$$

where a_j (b_j) and n_{aj} (n_{bj}) are respectively the bosonic annihilation and onsite number operator for j^{th} lattice site on leg-a(b). The hopping amplitudes along the respective legs are denoted by t_a and t_b . The parameters α_a and α_b set the SSH model type dimerization along the a and b legs respectively. The two legs interact with each other through hopping and interactions along the rung-direction. Here t_p represents the hopping amplitude along the rung, and V is the inter-leg interaction strength. The hardcore constraint is imposed by assuming $(a^\dagger)^2 = 0$, which ensures not more than one boson in a particular site.

In this work, we systematically analyze the effect of t_p and V on the topological properties of the system. In our studies, we consider two different combinations of dimerizations such as (a) uniform dimerization i.e. $\alpha_a = \alpha_b > 0$ and (b) staggered dimerization i.e. $\alpha_a = -\alpha_b > 0$ as depicted in Fig. 4.1(a) and (b), respectively. In the absence of t_p and V , for the uniform dimerization case, the particles in both the legs are in topological phases and for the staggered dimerization case the particles in leg-a are in topological phase and in leg-b they are in the trivial phase. In the following we study the effect of t_p and V on the topological features of the system.

To achieve the above two dimerization patterns, we set the following parameters.

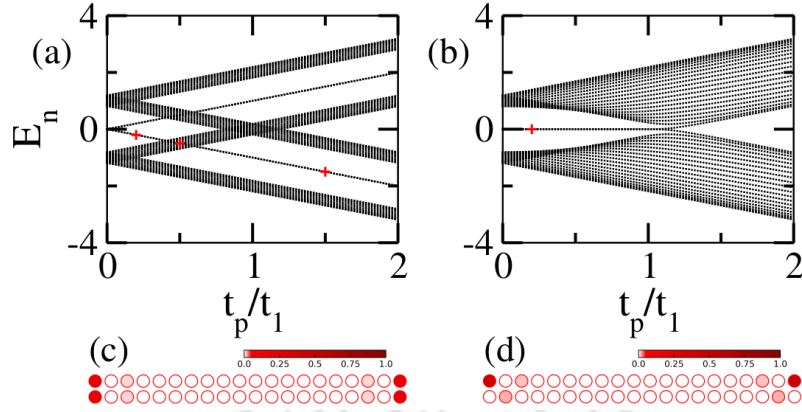


Figure 4.2: The single particle energy spectrum of a system of 40 sites ($L = 20$) with varying t_p for (a) uniform dimerization pattern ($t_a = t_b = 0.6t_1$ and $\alpha_a = \alpha_b = 0.4t_1$) and (b) staggered dimerization pattern ($t_a = t_b = 0.6t_1$ and $\alpha_a = -\alpha_b = 0.4t_1$) along the legs. (c) and (d) show the on-site probability $|\psi_j|^2$ of states marked by the red plus signs in (a) and (b) respectively. Note that, the on-site probability for of all the states marked in (a) are identical as that of in (c). This clearly indicates that the edge states are crossing the band from one gapped phase to another.

The uniform dimerization is enforced by fixing $t_a = t_b = t$ and $\alpha_a = \alpha_b = \alpha$. Similarly, the staggered dimerization pattern along the legs is enforced by setting $t_a = t_b = t$ and $\alpha_a = -\alpha_b = \alpha$. We consider $t = 0.6$ and $\alpha = 0.4$ in our calculations such that the hopping strength in strong and weak bonds in the legs are $t_1 = t + \alpha = 1$ and $t_2 = t - \alpha = 0.2$, respectively. Here $t_1 = 1.0$ defines the unit of energy, which makes the other parameters in the system dimensionless.

4.3 Results

Before presenting many-body features, we first analyze the single particle spectrum of the model shown in Eq. 5.1. Although the model under consideration is for hardcore bosons, we show that significant insights about the topological properties of the many-particle ground state can be obtained from the single particle spectrum at different fillings. In the following, we describe the quantum phases at different fillings for both the uniform and staggered dimerization configurations considered in our study.

As a specific representative case, we plot the numerically obtained single particle spectrum as a function of t_p for a system of length $L = 20$ for uniform dimerization ($t_a = t_b = 0.6t_1$ and $\alpha_a = \alpha_b = 0.4t_1$) and staggered dimerization case ($t_a = t_b = 0.6t_1$ and $\alpha_a = -\alpha_b = 0.4t_1$) in Fig. 4.2(a) and (b) respectively.

Note that for the case of uniform dimerization, the system is a weak topological system consisting of a stack of lattices that are topologically identical in nature. When $t_p = 0$, the two legs of the ladder are equivalent to two isolated SSH chains, which are individually known to manifest a gap in the middle of the spectrum due to the onset of the bond order (BO) phase [1]. This gapped phase hosts a pair of symmetry protected zero-energy edge states (see Fig. 4.2(a)). When t_p takes finite values, apart from the gap at the middle of the spectrum, two more gaps open up symmetrically at quarter and three quarter fillings of the spectrum after a critical t_p due to the formation of a plaquette order (PO) in the system, which will be discussed in details in the next section. The zero energy edge modes in the two legs of the ladder hybridize to become energetic while staying at the edges. These states can be called as mid-gap states. However, in this case, these states merge with the energy bands before the bulk gap closes at a higher value of t_p violating the bulk-edge correspondence. As mentioned before, this phenomenon can be attributed to the weak topology of the uniform dimerization configuration. With further increase in t_p , the bulk gap opens up again but without the mid-gap states. A pair of mid-gap states appear inside the two symmetrically formed gaps at quarter and three quarter fillings of the energy spectrum. To confirm that these mid-gap states are edge states, in Fig. 4.2(c) we plot the probability density $|\psi_j|^2$ of these states marked by red plus signs in Fig. 4.2(a) where ψ_j is the wavefunction amplitude at each lattice site j . It can be clearly seen that the amplitude ψ_j has maximum weight on the edge lattice sites of both the legs. We note that these mid-gap states cross the bulk bands and go from one gapped phase to another gapped phase as a function of t_p . While crossing the band, the edge state retains its properties, i.e., the probability density behaves similar to Fig. 4.2(c) at all three positions marked by the red plus symbols in Fig. 4.2(a).

For the case of staggered dimerization, however, the single particle spectrum exhibits a simple but topologically richer picture. In this case a gap-closing transition occurs between two gapped phases as a function of t_p where one of the gapped phases hosts zero energy edge modes as can be seen from Fig. 4.2(b). This indicates a clear topological phase transition where the bulk-boundary correspondence is preserved. We plot the probability density ($|\psi_j|^2$) in Fig. 4.2(d) for the states marked by the red plus sign in Fig. 4.2(b). It can be seen that the edge states are concentrated on the two edges of leg-a.

The single-particle orbitals discussed above can be filled one by one from the lowest energy onwards to obtain different ground state phases arising at different

fillings of fermions in the many-body context. Fundamentally, hardcore bosons share some properties with the spinless fermions such as the energy and diagonal correlations but strictly in one dimension. The situation is different in the case of a two-leg ladder. A critical study on this front has been performed in Ref. [95] where the differences between non-interacting spinless fermions and hardcore bosons in a two-leg ladder model with uniform leg hopping has been highlighted. It has been shown in Ref. [95] that at half filling, both spinless fermions and hardcore bosons stabilize to the gapped phases as a function of the rung hopping. In these gapped phases the particles prefer to localize on the rungs. However, the difference between fermions and hardcore bosons is that the transition to the gapped phase occurs after a critical t_p for the case of spinless fermions, whereas for hardcore bosons, the system becomes a gapped RMI phase for any finite value of t_p indicating a clear difference between the two systems. While these differences exist, the single-particle analysis provides a broad basis for understanding topological insulators in both fermionic and bosonic systems.

4.3.1 Many-body phases

In this section we analyse the many-body physics of the SSH ladder shown in Eq. 5.1 in the absence of interaction (i.e. $V = 0$) for both the cases of dimerizations considered.

4.3.1.1 Uniform dimerization

In Fig. 4.3 we show the phase diagram for uniform dimerization on both the legs of the ladder with $t_a = t_b = 0.6t_1$ and $\alpha_a = \alpha_b = 0.4t_1$. The phase diagram is obtained as a function of the chemical potential μ and t_p , and it exhibits three gapped phases at $\rho = 1/2$, $1/4$ and $3/4$ denoted by the white regions with black solid boundaries. The boundaries of these gapped phases are calculated using the formula

$$\mu_- = E(N) - E(N - 1); \quad \mu_+ = E(N + 1) - E(N), \quad (4.2)$$

where $E(N)$ is the ground state energy of the system consisting of N bosons. Here, μ_- (μ_+) is the chemical potential that defines the lower (upper) boundary of a gapped phase. All the lines in the figure are plotted after extrapolating the values of μ_{\pm} to thermodynamic limit. One of the major differences that appears in the energy gap at $\rho = 1/2$ as compared to the single particle picture is that it always remains finite as a function of t_p (compare with Fig 4.2(a)). A similar feature exists

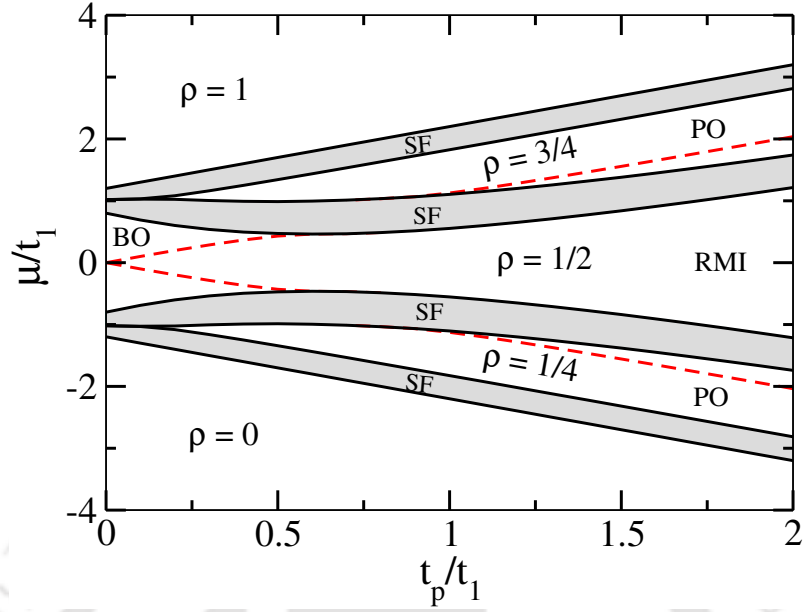


Figure 4.3: Phase diagram of Model(5.1) with $V = 0$, $t_a = t_b = 0.6t_1$ and $\alpha_a = \alpha_b = 0.4t_1$ plotted in the t_p - μ plane. The solid black lines show the phase boundaries of gapped phases, such as the plaquette order (PO), the bond order (BO), and the rung-Mott insulator (RMI) phases. The dashed red lines denote the mid-gap states. The gapless superfluid (SF) phase is represented by the grey shaded area.

for the non-dimerized hardcore bosonic ladder where a gapped RMI phase extends until $t_p = 0$ at half filling in contrast to the single-particle physics [95]. The red dashed lines are the mid-gap edge states which are determined by analysing the ρ - μ plot, as shown in Fig. 4.4. The figure depicts the behaviour of the bulk (ρ_b) and edge (ρ_e) densities which are defined as

$$\rho_b = \frac{1}{L-2} \sum_{j=2}^{L-1} \langle n_{aj} + n_{bj} \rangle \quad (4.3)$$

and

$$\rho_e = \frac{1}{4} \langle n_{a1} + n_{b1} + n_{aL} + n_{bL} \rangle \quad (4.4)$$

respectively as a function of μ . The panels (a), (b) and (c) of Fig. 4.4 show the ρ - μ behaviour for $t_p = 0.2t_1$, $0.75t_1$ and $1.5t_1$ respectively corresponding to three different cuts in the phase diagram of Fig. 4.3. The plateaus in the ρ_b curves (black solid lines) indicate the three bulk gaps at $\rho = 1/4$, $\rho = 1/2$ and $\rho = 3/4$ which confirm the existence of the gapped phases. The shoulders around the plateaus are the signature of gapless regions where the system exhibits a superfluid (SF) character with off-diagonal quasi-long-range order.

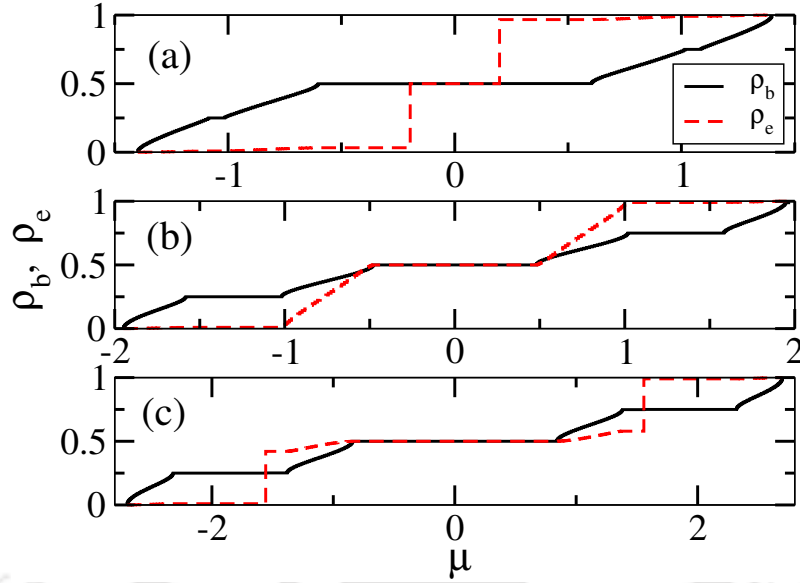


Figure 4.4: The figure displays the bulk and edge densities of the system represented by ρ_b and ρ_e respectively as a function of μ . (a), (b) and (c) show the ρ_b (solid lines) and ρ_e (dashed lines) with varying chemical potential μ for $t_p = 0.2t_1$, $0.75t_1$ and $1.5t_1$, respectively, corresponding to three cuts in the phase diagram shown in Fig 4.3. This shows the nature of the bulk phases (gapped or gapless) when the edge states are being filled in different parameter regimes.

The behaviour of the ρ_e (red dashed lines) in Fig. 4.4 reflects the existence of edge states in the system. When the bulk is gapped, the sudden change in the number of particles at the edges (N_e) by two or a change in ρ_e by 0.5 for $t_p = 0.2t_1$ and $1.5t_1$ (Fig. 4.4 (a) and (c)) mark the μ of the mid-gap edge states. The change in N_e by two particles is due to the two degenerate mid-gap edge states at that particular μ . Interestingly, for the case of $t_p = 0.75t_1$ (Fig. 4.4(b)), ρ_e increases continuously only when the bulk is in the gapless SF region with density $1/4 < \rho_b < 1/2$ and $1/2 < \rho_b < 3/4$. This indicates that, the edge states get filled up while the bulk of the system exhibits a gapless SF phase. As discussed earlier, a similar phenomenon can be seen in the single particle case, where the edge states survive inside the bands between half and quarter fillings.

Now we discuss the properties of the gapped phases in different parameter regimes. At $\rho = 1/2$, when $t_p = 0$, the two chains are isolated SSH chains. Due to the dimerized hopping on both legs, the system exhibits a gapped bond order (BO) phase along the legs with edge states on both legs. For the other limit of t_p , when it is large compared to the hopping along the legs the system is gapped once again, but due to the dimerization along the rungs. This phase is known as the rung-Mott insulator (RMI) phase as already introduced before. However, from

the phase diagram shown in Fig. 4.3, it can be seen that the two gapped phases at two limits of t_p are connected without any gap closing. To identify these phases, we calculate the bond energy along the legs and the rungs using the formula given by

$$\begin{aligned} B_{a,j} &= \langle a_j^\dagger a_{j+1} + H.c. \rangle; & B_{b,j} &= \langle b_j^\dagger b_{j+1} + H.c. \rangle \\ B_{r,j} &= \langle a_j^\dagger b_j + H.c. \rangle \end{aligned} \quad (4.5)$$

Here the subscripts a , b and r denote the leg-a, leg-b and the rung respectively. Fig. 4.5(a-d) display the bond energy in all the bonds along with the onsite particle densities for a system of size $L = 20$ at half filling when $t_p = 0.2t_1, 0.2t_1, 0.75t_1$ and $1.5t_1$ respectively. Here the thickness of the bonds is proportional to the bond energy B_j , and the face colour of the circles represents the particle densities on a particular site. In Fig. 4.5(a) we can see that the alternate bonds along the legs are stronger indicating the BO phase with one particle delocalized in the first and last rungs. When both the legs are isolated ($t_p = 0$), a configuration with one particle in one of the edges of leg-a and one particle in one of the edges of leg-b, is an energetically favourable configuration at half filling. However, in Fig. 4.5(a) since we consider a finite rung hopping ($t_p = 0.2t_1$), the system chooses to be in a state such that both the edge rungs have one particle delocalized in them, which is the minimum energy configuration. We can get more insights regarding the edge states by moving away from half filling, e.g., by adding one extra particle to the system we get a strong bond on the right most rung as shown in Fig. 4.5(b). This is because at $\rho_b = 1/2$, there are in principle two pairs of edge states at different μ . Since in this case we consider $N = L + 1$ particles, three out of four edge states are filled. Due to this, two particles reside on the left edge of the ladder (i.e. the first rung) and one particle resides on the right edge of the ladder (i.e. the last rung). The particle that resides on the last rung delocalizes itself on the rung due to finite t_p (as can be seen from Fig. 4.5(b)).

Apart from the gapped phase at $\rho = 1/2$, we also see two more gapped phases at $\rho = 1/4$ and $3/4$, which is expected from the single particle analysis. Note that the gapped phases at $\rho = 1/4$ and $\rho = 3/4$ are dual to each other due to the particle-hole symmetric nature of the model in the absence of interaction ($V = 0$). At $\rho = 1/4$ ($\rho = 3/4$), for $t_p = 0$, the system is in SF phase but when t_p is strong, a particle (hole) tends to get localized in every alternate plaquette of the ladder and hops within the plaquette only. This phase is very similar to the BO phase but here a particle gets trapped in a plaquette rather than a bond, which we call the plaquette

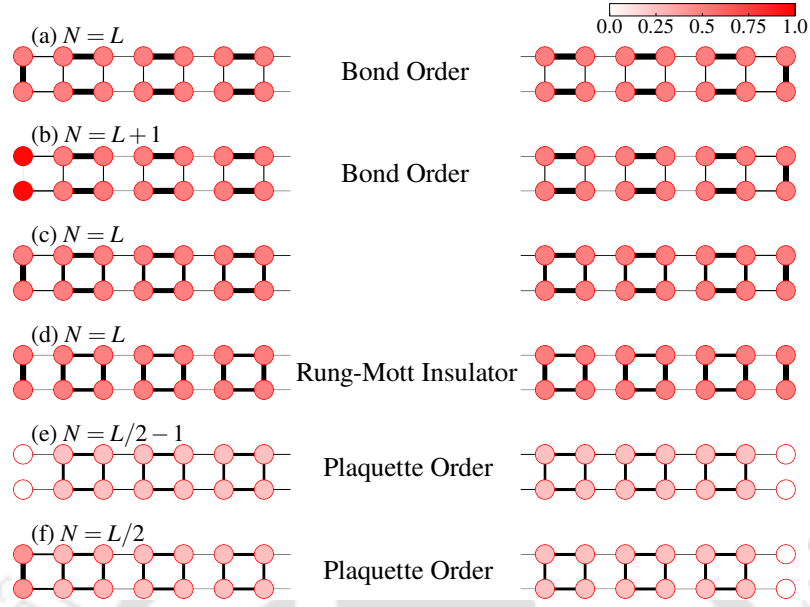


Figure 4.5: The figure shows the bond energies (B_j) of all the bonds defined in Eq. 4.5 and the onsite particle number ($\langle n_j \rangle$) for different phases corresponding to Fig. 4.3 with a system consisting of 40 sites ($L = 20$ rungs). In the figures, the thickness of a bond is proportional to the respective strength of B_j , and the face colour of the circles represents the values of $\langle n_j \rangle$. This captures different dimerization patterns and the existence of edge states in different phases. (a) shows B_j and $\langle n_j \rangle$ corresponding to the bond order (BO) phase at 1/2-filling ($N = L$) for $t_p = 0.2t_1$, which has two filled edge states (localized at each edge). The parameters in (b) are the same as (a) but with $N = L + 1$, which has three occupied edge states (two localized on the left edge and one on the right edge). (c) and (d) show the same quantities for $t_p = 0.2t_1$, $0.75t_1$ and $1.5t_1$ respectively at 1/2-filling ($N = L$). The change in bond order pattern can be seen going from the bond order (BO) (a) to the rung-Mott insulator (RMI) (d) phase. (e) and (f) correspond to the 1/4-filling plaquette order (PO) phases for parameters $t_p = 0.5t_1$ with $N = L/2 - 1$ and $t_p = 1.5t_1$ with $N = L/2$, respectively. The edge state appears (localized on the left edge) in (f). Note that in all the cases, we have used a small onsite potential of $-0.001t_1$ in one edge to break the degeneracy of the edge-state pair.

order (PO) phase. In Fig. 4.5(e) and (f), we show the bond energy and particle densities of the gapped phase at $\rho = 1/4$ for $t_p = 0.5t_1$ and $1.5t_1$ respectively. Here we can see that at every alternate plaquette, the bond energy is stronger. But the edge state exists only in Fig. 4.5(f), which is dimerized in the first rung.

4.3.1.2 Staggered dimerization

In this case, the leg-a (leg-b) of the ladder is considered to be of topological (trivial) nature. Similar to the uniform dimerization case, we first discuss the many-body phase diagram in the absence of interaction ($V = 0$) and compare it with the single particle picture (Fig. 4.2(b)). In Fig. 4.6, we show the phase diagram with the

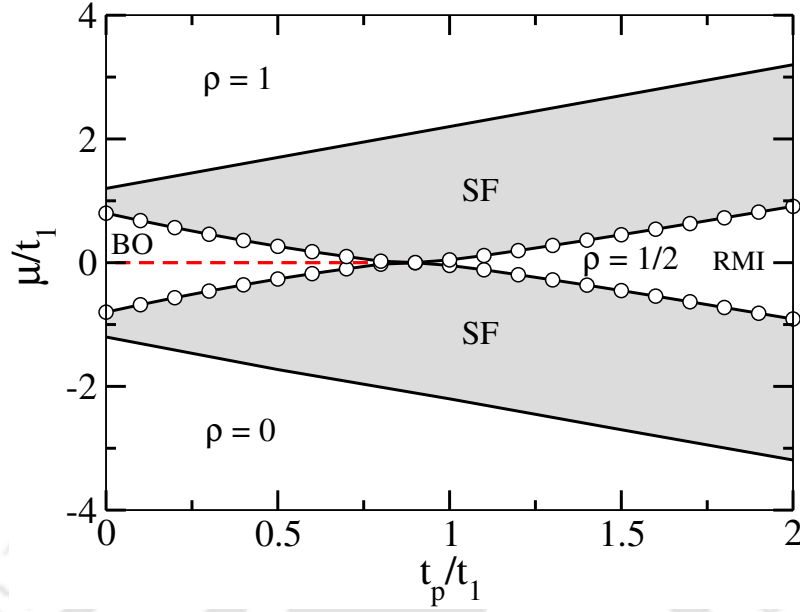


Figure 4.6: Phase diagram of Model(5.1) with $V = 0$, $t_a = t_b = 0.6t_1$ and $\alpha_a = -\alpha_b = 0.4t_1$ is plotted in t_p - μ plane. The solid black lines show the phase boundaries of gapped phases and the dashed lines denote the mid-gap states. The gapless superfluid (SF) phase is represented by the shaded grey area. A topological phase transition happens through a gap-closing point for $\rho = 1/2$ from a non-trivial bond order (BO) to a trivial rung-Mott insulator (RMI) phase.

parameters $t_a = t_b = 0.6t_1$ and $\alpha_a = -\alpha_b = 0.4t_1$ in the $\mu - t_p$ plane. In the figure, the white regions bounded by the black line with circles correspond to the gapped phases, and the grey regions around them are the gapless regions. The phase diagram clearly shows a phase transition between two gapped phases as a function of t_p at half-filling. In the following, we show that this transition through a gap-closing point is well defined topological phase transition, which was already indicated in the single-particle picture (compare with Fig. 4.2(b)).

First of all, when $t_p = 0$, the system corresponds to two isolated SSH chains. Due to staggered dimerization, the upper leg at $\rho = 1/2$, exhibits a nontrivial BO phase with zero-energy edge states, and the lower leg exhibits a trivial BO phase without any edge states. Because of this, there exists a finite gap at $t_p = 0$ with zero energy states at the middle. Upon switching on the rung hopping t_p , the system shows an affinity towards dimerizing along the rungs due to the enforcement of the RMI character. As a result, the topological BO phase and the edge states (red dashed line) survive up to certain values of t_p . After a critical value of $t_p \sim 0.9t_1$, the dimerization in the rungs dominate, leading to the appearance of the gapped RMI phase, which does not exhibit any edge states. This transition clearly occurs through a gap

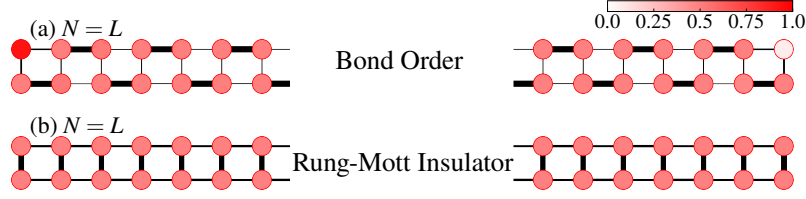


Figure 4.7: The figure shows the bond energy (B_j) of all the bonds defined in Eq. 4.5 and the onsite particle number ($\langle n_j \rangle$) for different phases of a system consisting of 40 sites ($L = 20$). (a) and (b) represent two gapped phases at the 1/2-filling ($N = L$), which are topological bond order (BO) and trivial rung-Mott insulator (RMI) phases corresponding to the parameter value $t_p = 0.25t_1$ and $1.5t_1$ respectively in Fig. 4.6. Here the thickness of a bond is proportional to the corresponding value of B_j , and the face color of the circles represents the onsite particle number. We can see the change in dimerization pattern between (a), which also has an occupied edge state (localized at the left edge), and (b). Note that in both cases, we have used a small onsite potential of $-0.001t_1$ in one edge to break the degeneracy of the edge-state pair.

closing point, indicating a topological phase transition as a function of t_p . These two gapped phases can be distinguished by comparing their bulk behavior through B_j as shown in Fig. 4.7(a) and (b) which are plotted for parameters $t_p = 0.25t_1$ and $1.5t_1$ respectively at $\rho = 1/2$. From the figure, it can be seen that when t_p is below the critical value, the dimerization is maximum along the legs of the ladder and the left edge of leg-a is occupied by a particle, indicating the presence of an edge state. When t_p is above the critical value, we see a dominant dimerization along the rungs forming the RMI phase, which does not host any edge states.

In this section, we study the fate of the topological phase that occurs for the staggered dimerization case in the presence of interaction (V). For this purpose, we start in the parameter domain $t_p = 0.2t_1$, $t_a = t_b = 0.6t_1$ and $\alpha_a = -\alpha_b = 0.4t_1$ in the non-interacting phase diagram shown in Fig. 4.6, where the system is in a gapped BO phase exhibiting edge states at $\rho = 1/2$ and examine the effect of finite V . By introducing V , we obtain a phase diagram which is shown in Fig. 4.8 in the $\mu - V$ plane, obtained after appropriate finite-size extrapolation. The phase diagram clearly shows a gapped to gapped phase transition where the gapped and gapless phases are indicated by the white and grey regions, respectively. We find that the degenerate edge states still survive at finite V (indicated by the red dashed line), preserving the topological nature of the phase. With increase in V , however, a gap-closing transition to a trivial phase occurs at a critical interaction strength $V_c \sim 2.85t_1$. The gap closing transition induced by interaction signifies the bulk-edge correspondence of the topological phase transition even though the edge states

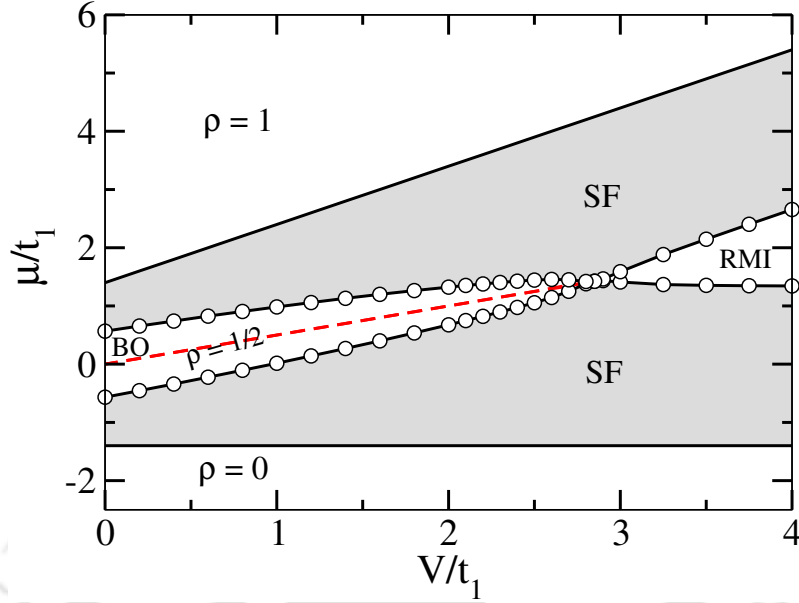


Figure 4.8: Phase diagram of Model(5.1) with $t_a = t_b = 0.6t_1$, $\alpha_a = -\alpha_b = 0.4t_1$ and $t_p = 0.2t_1$ is plotted in V - μ plane. The solid black lines show the phase boundaries of gapped phases and the red dashed lines stand for the mid-gap edge states. The gapless superfluid (SF) phase is represented by the shaded grey area. Here, at $\rho = 1/2$, the topological phase transition occurs from a non-trivial bond order (BO) to a trivial rung-Mott insulator (RMI) phase through a gap-closing point with increasing V .

shift from the $\mu/t_1 = 0$ value due to the particle-hole symmetry breaking of the Hamiltonian. Note that in this case, the gapped phase below V_c is a nontrivial BO phase, and above V_c , it is the RMI phase.

The underlying mechanism of this interaction-induced topological phase transition can be described by the arguments based on the minimization of the ground state energy. Starting from the non-interacting ($V = 0$) case (e.g., Fig. 4.7(a)), the dimerization pattern reveals a large probability of finding two particles on a single rung. At finite V , this configuration is unfavourable due to an extra energy cost. In such a situation, to minimize the energy, the system tends to dimerize along the rungs by localizing one particle at each rung. This preference of dimerization along the rungs by the particles leads to a transition from the BO phase (topological) to the RMI phase (trivial) as a function of V . This also suggests that a finite $V > 0$ favors a topological phase transition and therefore, the transition should occur at a smaller t_p as compared to the $V = 0$ case. This is confirmed in our numerical simulations as shown in Fig. 4.9, where we compare the average bond energies along the legs (B_a and B_b) and the rungs (B_r) as a function of t_p for different values of V . It can be clearly seen that for $V = 1.5t_1$ (Fig. 4.9(a)) the bond energy along

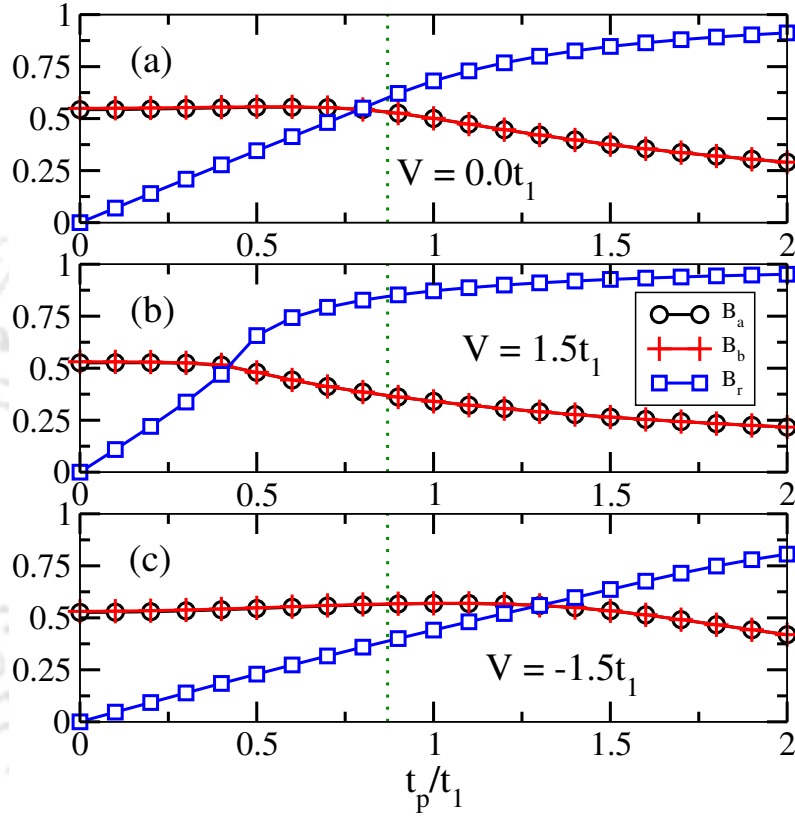


Figure 4.9: Bond energies along the legs ($B_{a,b}$) and along the rung (B_r) computed by averaging over all the respective bonds for 240 sites ($L = 120$) at $\rho = 1/2$. (a), (b) and (c) represent the bond energies for $V = 0.0t_1$, $1.5t_1$ and $-1.5t_1$, respectively, with varying t_p . The B_r dominates over $B_{a,b}$ after different t_p values for different values of V , implying the onset of a trivial RMI phase with different critical transition points. The green dotted lines in all the plots mark the critical point corresponding to $V = 0.0t_1$ in Fig. 4.6.

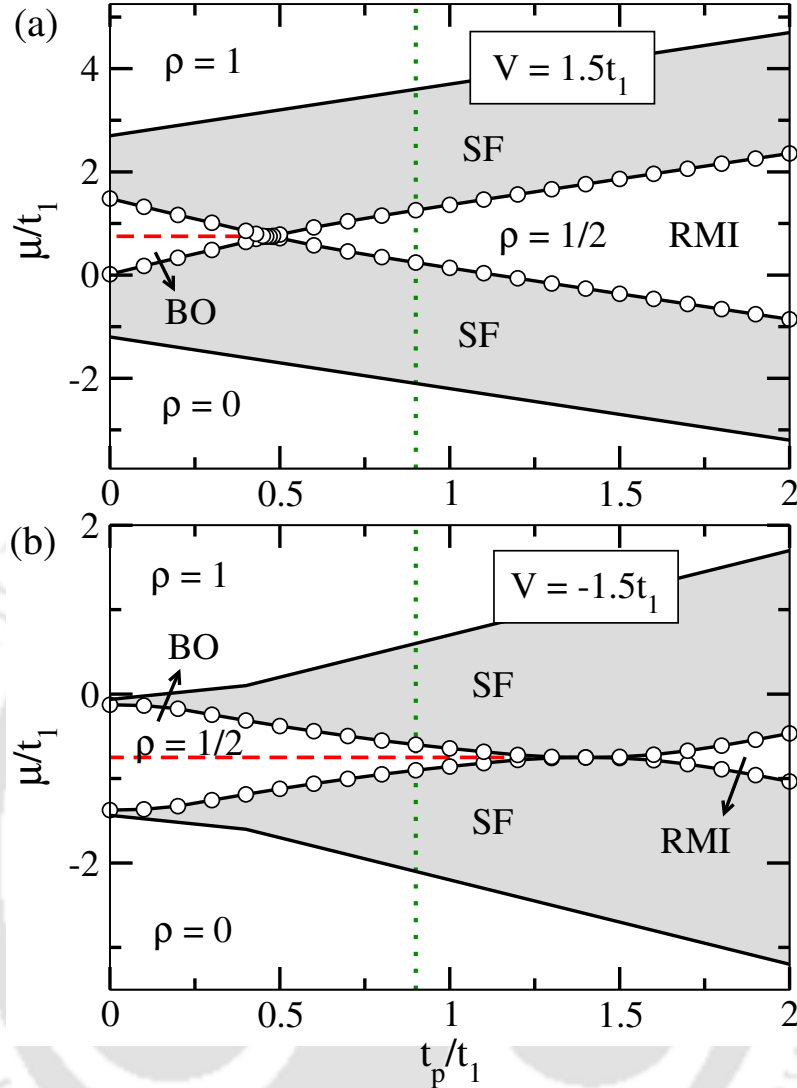


Figure 4.10: Phase diagrams of Model(5.1) with (a) $V = 1.5t_1$ and (b) $V = -1.5t_1$ are plotted in $t_p - \mu$ plane. The solid black lines show the phase boundaries of the gapped topological bond order (BO) phase, and trivial rung-Mott insulator (RMI) phases. The dashed lines stand for the mid-gap edge states. The gapless superfluid (SF) phase is represented by the shaded grey area. The green dotted line marks the critical point corresponding to $V = 0.0t_1$ in Fig. 4.6. The change in the gapless critical points for finite interaction can be seen by comparing to the non-interacting case at half-filling.

the rungs starts to dominate over the bond energies along the legs at a smaller t_p , indicating an early BO-RMI transition compared to the case when $V = 0.0t_1$ (see Fig. 4.9(b)).

In this context, we also examine the effect of attractive interaction on the topological phase transition. We find that the B_r dominates over all other bond-energies at a larger value of t_p for attractive V as shown in Fig. 4.9(c) (for $V = -1.5t_1$). This

opposite behaviour can be understood using an argument similar to the repulsive V case. When $V < 0.0t_1$, the particles prefer to dimerize along the legs rather than on the rungs. Hence, a larger t_p is necessary to break the bond ordering along the legs and introduce rung dimerization as compared to the repulsive V case. These behaviors can also be seen in the phase diagrams shown in Fig. 4.10 (a) and (b) for $V = 1.5t_1$ and $V = -1.5t_1$ respectively. Comparing the transition point for $V = 0.0t_1$ marked by vertical dotted lines, we can clearly see that, the topological phase transition occurs at a smaller (larger) critical t_p for repulsive (attractive) V .

To quantify the interaction induced topological phase transition, we obtain the critical rung hopping strengths t_p^c for different values of V by monitoring the bulk gap-closing point (as already done for Fig. 4.6 and Fig. 4.10). To this end we fix $t_a = t_b = 0.6t_1$ and $\alpha_a = -\alpha_b = 0.4t_1$ in the Hamiltonian shown in Eq. 5.1 and compute the phase diagram in the $V - t_p$ plane as shown in Fig. 4.11 (a) where the topological phase (brown region) and trivial phase (white region) are separated by the critical boundary (line with circles). We obtain that the t_p^c shifts to a higher (lower) value for attractive (repulsive) interaction.

The topological phase transitions can also be detected from the discontinuous jump in the topological invariant of the corresponding phases. A bulk topological invariant, calculated from the Berry phase, is always linked with the symmetry-protected edge states according to bulk-boundary correspondence in topological systems. The Berry phase, defined by the formula

$$\gamma = \int_0^{2\pi} \langle \psi(\theta) | \partial_\theta \psi(\theta) \rangle d\theta \quad (4.6)$$

can be a suitable topological invariant for our model in the many-body limit under twisted phase boundary conditions (TBCs) [13]. Here $|\psi\rangle$ is the ground state wavefunction, and we achieve the TBC by setting $a_j \rightarrow e^{i\theta/L} a_j$ and $b_j \rightarrow e^{i\theta/L} b_j$ in leg-a and leg-b, respectively. When the twist angle θ is varied from 0 to 2π adiabatically, $|\psi\rangle$ picks up a phase, which is nothing but the Berry phase. Thus, γ is expected to be quantized in units of π for a topological phase, whereas it should vanish in the trivial phase. We plot γ/π as a function of t_p in Fig. 4.11 (b) to capture the topological phase transitions for $V = 0.0t_1, 1.5t_1$ and $-1.5t_1$. As anticipated, γ clearly distinguishes the topological BO and trivial RMI phases for all three values of V . It also marks the respective critical points ($\sim 0.87t_1$ for $V = 0.0t_1$, $\sim 0.47t_1$ for $V = 1.5t_1$ and $\sim 1.4t_1$ for $V = -1.5t_1$), where we see an abrupt jump from $\gamma = \pi$ to $\gamma = 0$.

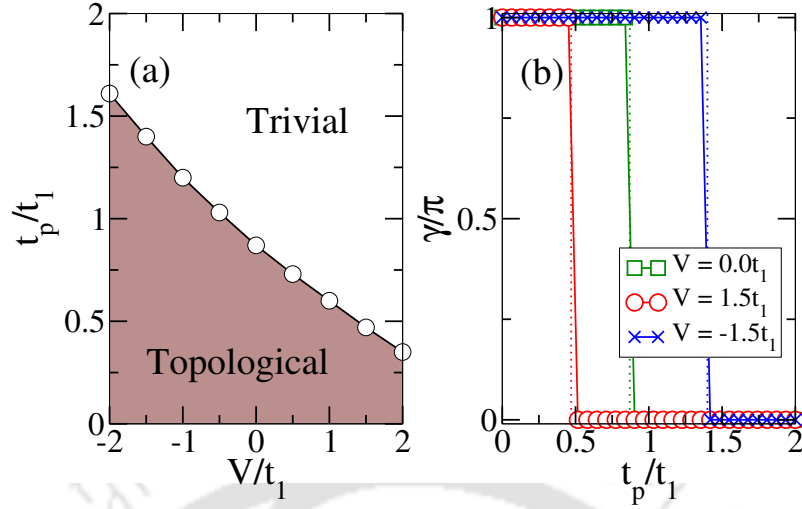


Figure 4.11: (a) Phase diagram at $\rho = 1/2$ corresponding to the Hamiltonian given in Eq. 5.1 for $t_a = t_b = 0.6t_1$ and $\alpha_a = -\alpha_b = 0.4t_1$ (staggered dimerization). Here the topological (trivial) phase is the BO (RMI) phase. The figure shows how the critical point changes with the interaction strength V . (b) Berry phase under twisted phase boundary conditions showing the topological phase transition as a function of t_p/t_1 for $V = 0.0t_1, 1.5t_1$ and $-1.5t_1$ on a system of length $L = 6$ (12 lattice sites). The dotted lines mark the transition points extracted from the phase diagram in (a) corresponding to each V .

We now propose an experimentally relevant quantity in terms of Thouless charge pumping (TCP)[96] which can detect the interaction-induced topological phase transition arising from our model. The TCP has recently been used to characterize the topological nature of a system both in theory as well as in experiments [53, 54, 97–102]. As per the TCP measure, it is possible to pump a quantized amount of charge with an adiabatic variation of the system parameters in a pumping cycle which is related to the Chern number. The celebrated Rice-Mele (RM) model [103, 104] defines the pumping protocol in one dimension where in the parameter space, the pumping path winds around a gapless singular point [69]. Here the system periodically and adiabatically goes from non-trivial to trivial and to non-trivial phase again by breaking the symmetry that protects the topology in the system. While originally, the RM model described the TCP of non-interacting systems, recently its connection to interacting systems has been proposed in various systems [3, 69, 72, 98, 105–110]. For our current system under consideration, which exhibits a topological phase transition, we can define a pumping protocol by introducing a symmetry breaking term such that the pumping path in the parameter space adiabatically winds around the topological phase transition point.

In the following, we present the pumping protocol for the two-leg ladder system

with the parametric extension of the model 5.1 which is given as

$$\begin{aligned}
 \mathcal{H}_p(\tau) = & - \sum_j (t_a - (-1)^j \alpha_a) (a_j^\dagger a_{j+1} + \text{H.c.}) \\
 & - \sum_j (t_b - (-1)^j \alpha_b) (b_j^\dagger b_{j+1} + \text{H.c.}) \\
 & - (t_o + \delta(\tau)) \sum_j (a_j^\dagger b_j + \text{H.c.}) \\
 & + \Delta(\tau) \sum_j ((-1)^j n_{aj} + (-1)^{j+1} n_{bj}) \\
 & + V \sum_j n_{aj} n_{bj},
 \end{aligned} \tag{4.7}$$

where $\delta(\tau) = A_\delta \cos(2\pi\tau)$ changes the hopping dimerization along the rungs and $\Delta(\tau) = A_\Delta \sin(2\pi\tau)$ changes the staggered onsite potential, which breaks the sublattice symmetry. The quantity τ is the adiabatic pumping parameter with $O = (t_p = t_o, 0)$ as the origin of the pumping cycle in the $\delta - \Delta$ plane. A schematic representation of the periodic variation of the parameters is shown in Fig. 4.12(a) for three different t_o 's with A_δ and $A_\Delta > 0$. Note that the pumping can only happen if the pumping path encloses the gap-closing critical point (t_p^c). This implies that only for the cycle-2 (green continuous line) of Fig. 4.12(a) we can expect robust and quantized charge pumping.

However, the results obtained for $V = 0$ suggest that the critical rung hopping t_p^c for the topological phase transition can be moved towards smaller and larger values depending on the repulsive or attractive nature of V , respectively. Hence, it can be made possible to shift the t_p^c along the δ axis of Fig. 4.12(a) by a suitable choice of V such that it lies inside the cycle-1 or 3 and a finite quantized amount of pumped charge can be generated in these cases. The phenomenon of charge pumping induced by interactions, can be termed as an interaction-induced topological charge pumping (iTCP).

In our analysis, the iTCP is demonstrated by defining three different pumping cycles for three parameter sets of $(t_o, A_\delta, A_\Delta)$ in Fig. 4.12(a) such as cycle-1: $(0.5t_1, 0.3t_1, 0.5t_1)$, cycle-2: $(1.0t_1, 0.4t_1, 0.5t_1)$ and cycle-3: $(1.4t_1, 0.4t_1, 0.5t_1)$. All the cycles correspond to the parameter sets $t_a = t_b = 0.6t_1$, $\alpha_a = -\alpha_b = 0.4t_1$, for which the critical rung hopping for the non-interacting ($V = 0$) topological phase transition is $t_p^c \sim 0.87t_1$ (Fig. 4.6) at half-filling. Following the standard protocol of

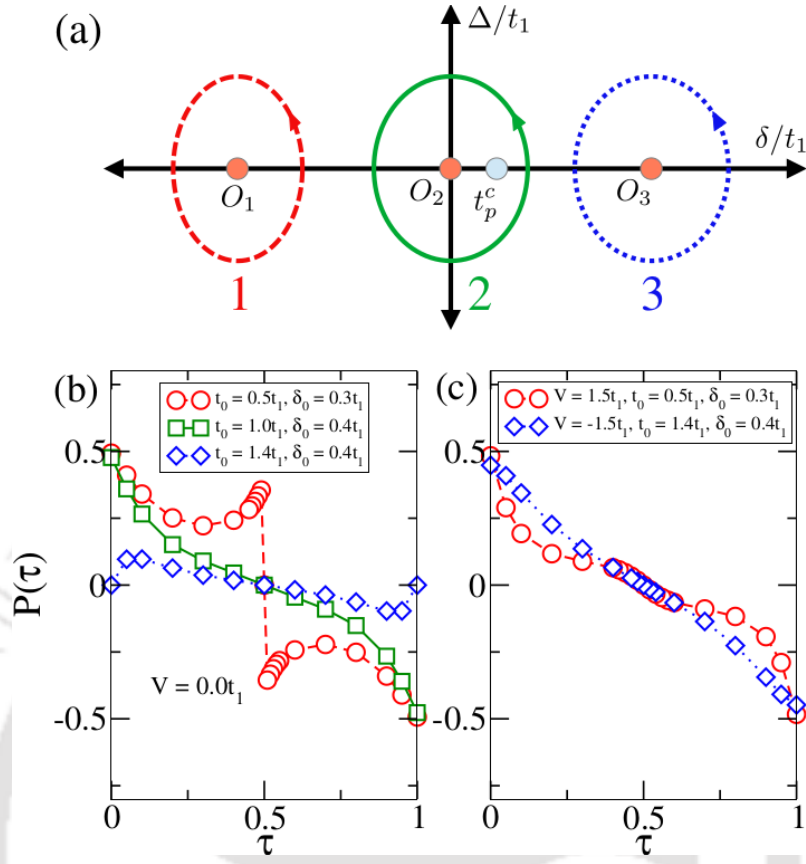


Figure 4.12: (a) Pictorial representation of the adiabatic variation of parameters are shown for three different pumping cycles with three different origins (t_o 's). The topological phase transition critical point t_p^c is marked with a green circle on the δ -axis. (b) The evolution of the polarization ($P(\tau)$) is plotted for three different t_o 's corresponding to three different pumping cycles shown in (a) for $V = 0$. Here $t_p^c \sim 0.87t_1$. Here only cycle-2, which encloses the t_p^c , shows robust pumping. (c) The evolution of $P(\tau)$ is shown for the same parameters corresponding to cycle-1 and 3 that are considered in (b), but with finite interaction strength $V = 1.5t_1$ and $V = -1.5t_1$ respectively. Unlike the non-interacting case, here a quantized amount of charge is being pumped. We call this phenomenon as the interaction-induced topological charge pumping. Here, for all the cases we consider $\Delta = 0.5t_1$ and a finite system of $L = 200$ rungs.

the charge pump, we compute a quantity known as polarization using the formula

$$P(\tau) = \frac{1}{L} \sum_{j=0}^{L-1} \langle \psi(\tau) | (j - L/2) n_j | \psi(\tau) \rangle \quad (4.8)$$

which can estimate the pumped charge (Q) as,

$$Q = \int_0^1 d\tau \partial_\tau P(\tau). \quad (4.9)$$

Here, $|\psi(\tau)\rangle$ is the ground state corresponding to the Hamiltonian $\mathcal{H}_p(\tau)$ since the evolution is adiabatic. In Fig. 4.12(b), we plot $P(\tau)$ for $V = 0$, for the pumping cycle-1 (dashed line with circles), cycle-2 (continuous line with squares) and cycle-3 (dotted line with diamonds). According to the parameters considered, the t_p^c resides on the δ axis within the cycle-2 ($t_o - A_\delta < 0.87t_1 < t_o + A_\delta$) only. Thus, we can see from the figure that only for cycle-2, $P(\tau)$ varies continuously from 0.5 to -0.5 resulting in $|Q| = 1$. However, for cycle-1 and cycle-3, the situation is completely different. For cycle-1, there is a clear breakdown of charge pumping in the middle of the pumping cycle, and there is no charge being pumped for cycle-3.

To verify the iTCP, we re-perform the pumping along cycle-1 and 3 with finite interactions $V = 1.5t_1$ and $-1.5t_1$, which shift the t_p^c into cycle-1 and cycle-3, respectively. In Fig. 4.12(c), we plot $P(\tau)$ for cycle-1 (dashed line with circles) and cycle-3 (dotted line with diamonds). The continuous change of $P(\tau)$ from 0.5 to -0.5 clearly shows a quantized TCP for both the cases. Note that this finite TCP was not present for the $V = 0$ case (Fig. 4.12(b)), and it is induced by the interaction (V), indicating an iTCP. This analysis substantiates the interaction-induced topological phase transition as already shown in Fig 4.11.

From the analysis above, we can see that interaction favours a topological phase transition from topological BO to the trivial RMI phase. The same underlying physics also dictates the change in the critical rung hopping of topological phase transition in the presence of interaction. Such an interaction effect on the topological phase transition allows for an interaction-induced topological charge pumping.

4.4 Conclusions

In summary, we have studied the topological properties of the bosonic Su-Schrieffer-Heeger ladder for its two possible configurations. These configurations correspond to the uniform dimerization case where the dimerization pattern is such that both the legs are topological for the appropriate choice of boundary conditions, and the staggered dimerization case, where one of the legs is topological and the other is trivial. Compared to previous studies of either single particle physics or fermions, we analyzed hardcore bosons hopping on the ladder and endowed with interleg interactions. We first analyzed the ground state properties of the many-body system without any inter-leg interaction and showed that for the uniform dimerization case, there is no topological phase transition as a function of the rung hopping strength. Rather, the system goes from a gapped bond order phase to a gapped rung-Mott insulator phase

at half-filling without any gap-closing. In contrast, the staggered dimerization case supports a well defined topological phase transition from a topological bond order phase to a trivial rung-Mott insulator phase. Further, we investigated the effect of inter-leg interaction which greatly influences the topological phases. We found a topological phase transition as a function of interaction for a fixed rung hopping strength. We also found that when interaction is fixed, the critical rung hopping for the topological phase transition strongly depends on the nature of the interaction. That is, for repulsive (attractive) interaction the topological phase transition occurs at a smaller (larger) critical rung hopping strength. We characterized the transitions through multiple approaches and density matrix renormalization group (DMRG) techniques; these included obtaining the excitation gap, edge state profiles, Berry phases and Thouless charge pumping measures.





Chapter 5

Multiple localization transitions in a quasiperiodic lattice

5.1 Introduction

In general, it is understood that after the localization transition in quasiperiodic systems, the localized states remain localized as a function of the quasidisorder. However, a recent study has revealed the phenomenon of the re-entrant localization transition by imposing certain constraints on the parameters of the AA model [111]. It has been shown that a dimerized hopping strength along with staggered onsite disorder, drives the system through two localization transitions. In other words, after a first localization transition, some of the localized states become extended for a range of parameters and eventually become localized at a different critical disorder strength. On the other hand, a cascade of localization transitions has been predicted and observed [112] in a system with an engineered quasiperiodic potential that continuously maps the AA model to the Fibonacci model [113, 114]. These remarkable findings further motivate to explore the possible existence of such multiple localization transitions in a simple quasiperiodic model without directly imposing any constraint on the quasidisorder.

5.2 Model and approach

The one-dimensional quasiperiodic lattice model which is considered for our studies is given by

$$H = -J \sum_i (c_i^\dagger c_{i+1} + H.c.) + \lambda \sum_i \cos(2\pi\beta i + \phi) n_i + \Delta \sum_i (-1)^i n_i \quad (5.1)$$

where c_i^\dagger and $n_i = c_i^\dagger c_i$ are the fermionic creation and the number operator respectively at site i . J is the hopping matrix element between the nearest-neighbour sites and λ corresponds to the quasiperiodic disorder (hereafter referred as only disorder) strength. Unless mentioned otherwise, all the numerical simulations are performed under open boundary condition (OBC). The quasiperiodicity is ensured by choosing irrational numbers $\beta = (\sqrt{5} - 1)/2$ - known as the inverse Golden ratio and $\beta = F_{n-1}/F_n$ with F_n being the n -th Fibonacci number for OBC and periodic boundary condition (PBC), respectively. The ratios of Fibonacci numbers are used to protect the quasiperiodicity in the PBC [115–118] which tend to the inverse Golden ratio for large system sizes. ϕ is the phase offset between the primary and secondary lattices and Δ is the onsite staggered potential. We set $J = 1$ as the unit of energies and considered system sizes according to the Fibonacci series. Note that when $\Delta = 0$, the Eq. 5.1 represents the standard AA model which exhibits a sharp localization transition at $\lambda_{AA} = 2$. For our analysis we consider large system sizes such that the effect of ϕ is negligible. Therefore, for most of the cases we set $\phi = 0$ unless otherwise mentioned. It is important to note that the lattice corresponding to Eq. 5.1 has already been used as a tool to observe the localization transitions [119–121]. However, the localization transition of the model corresponding to Eq. 5.1 itself has not been explored in detail except for some specific parameter domain where a re-entrant localization of individual states has been predicted [122]. In the following we explore the physics of this simple yet not well explored model and predict the phenomenon of multiple localization transitions.

5.3 Results

In this we discuss our main results where we show the appearance of the multiple localization transition and then its possible signatures from the wavepacket dynamics.

5.3.1 Multiple localization transitions

In this section we study the localization transition of the model given in Eq. 5.1 and the central result is given as the phase diagram in the $\Delta - \lambda$ plane as depicted in Fig. 5.1(a). The blue region below (above) the red region is the extended (localized) phase and the red region corresponds to the intermediate phase where both extended and localized states exist. It can be seen that the system undergoes localization transitions (from all states extended to all states localized) through the intermediate region as a function of λ for all values of Δ except at $\Delta = 0$ (the AA limit). This is expected as the self-duality of Eq. 5.1 is broken due to the onset of Δ . However, for some particular values of Δ , two localization transitions or the re-entrant localization transitions [111] occur as a function of λ . This type of signature is similar to the situation discussed in Ref. [111]. However, the interesting feature here is that for a range of λ ($1 < \lambda \lesssim 2$), the system undergoes a series of localization transitions as a function of Δ . In the following we discuss the phase diagram of Fig. 5.1(a) in detail.

The signatures of the localization transition can be discerned from the participation ratios (PRs) [5, 111, 115, 123] which are considered to be the standard diagnostics to study the localization transitions. We compute the inverse participation ratio (IPR) and the normalized participation ratio (NPR) for the m^{th} eigenstate defined as $\text{IPR}_m = \sum_{i=1}^L |\psi_m^i|^4$ and $\text{NPR}_m = \left(L \sum_{i=1}^L |\psi_m^i|^4 \right)^{-1}$ respectively, where i is the site index [115, 124, 125]. The values of $\text{IPR}_m = 0$ ($\neq 0$) and $\text{NPR}_m \neq 0$ ($= 0$) in the large L limit characterize the extended (localized) states. The re-entrant localization behaviour can be understood by directly plotting the IPR as a function of all the eigenenergies and eigenstates of Eq. 5.1 for different values of λ as depicted in Fig. 5.1(b) and (d) respectively for an exemplary value of $\Delta = 1.8$. While the regions with dark blue (red) color for all the states indicate the extended (localized) phases at weak (strong) values of λ , two intermediate phases in the range $0.4 \lesssim \lambda \lesssim 0.8$ and $1.4 \lesssim \lambda \lesssim 1.6$ indicate the presence of both extended ($\text{NPR} \neq 0$) and localized ($\text{IPR} \neq 0$) states. Based on the behaviour of the PRs of the states we compute the phase diagram shown in Fig. 5.1(a) by plotting the quantity $\eta = \log_{10}[\langle \text{IPR} \rangle \times \langle \text{NPR} \rangle]$ [5, 111] in the $\Delta - \lambda$ plane. Here $\langle \cdot \rangle$ stands for the average over the entire spectrum. For the extended or localized phase since either $\langle \text{IPR} \rangle$ or $\langle \text{NPR} \rangle$ has $1/L$ dependence on the system size, $\eta < -\log_{10} L$ i.e. $\eta < -4$ as $L \sim 10^4$ in our case but when both of them are finite, i.e. of $\mathcal{O}(1)$, we get $-4 < \eta < -1$. The phase diagram clearly exhibits two localization transitions

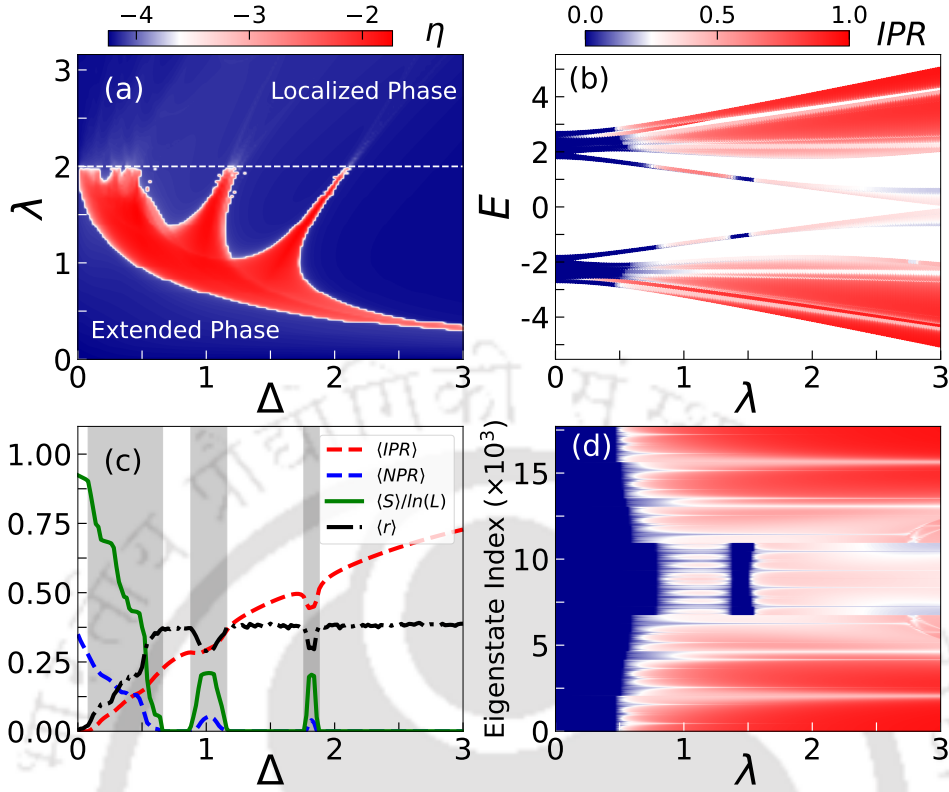


Figure 5.1: (a) The phase diagram in the $\Delta - \lambda$ plane obtained using the values of η for a system of size $L = 17711$. (b) IPR of all the eigenstates as a function of energies and λ for $\Delta = 1.8$ and a system size of $L = 17711$. (c) Extrapolated values of $\langle \text{IPR} \rangle$ (dashed red), $\langle \text{NPR} \rangle$ (dashed blue) with system sizes $L = 2584, 4181, 6765, 10946, 17711$, $\langle S \rangle / \ln(L)$ (solid green) for $L = 17711$ and $\langle r \rangle$ (dot-dashed black) for $L = 2584$ are plotted as a function of Δ for $\lambda = 1.5$ showing the multiple localization transitions. The $\langle r \rangle$ is computed using PBC with $\beta = 1597/2584$ and an average over 5000 phase offsets ϕ are considered. The intermediate phases are indicated by the grey shaded regions. (d) IPR of all the eigenstates as a function of state index and λ for $\Delta = 1.8$ and $L = 17711$. The white dashed line in (a) indicates the AA critical point at $\lambda = 2$.

(re-entrant localization) as a function of λ for several values of Δ . However, for some fixed values of λ , the localization transition is robust as a function of Δ . For smaller λ , there exists only one localization transition at larger Δ . With increase in λ the system exhibits multiple localization transitions as a function of Δ . Interestingly, the number of localization transitions increases up to $\lambda \lesssim 2 = \lambda_{AA}$ where four localization transitions can be seen.

To quantify these localization transitions as a function of Δ , we plot the extrapolated values of average PRs as a function of Δ in Fig. 5.1(c) for a cut through the phase diagram of Fig. 5.1(a) at $\lambda = 1.5$. Initially, when $\lambda = 1.5$ and $\Delta = 0$ (AA limit), the system is in the extended phase indicated by $\langle \text{IPR} \rangle = 0$ and $\langle \text{NPR} \rangle \neq 0$.

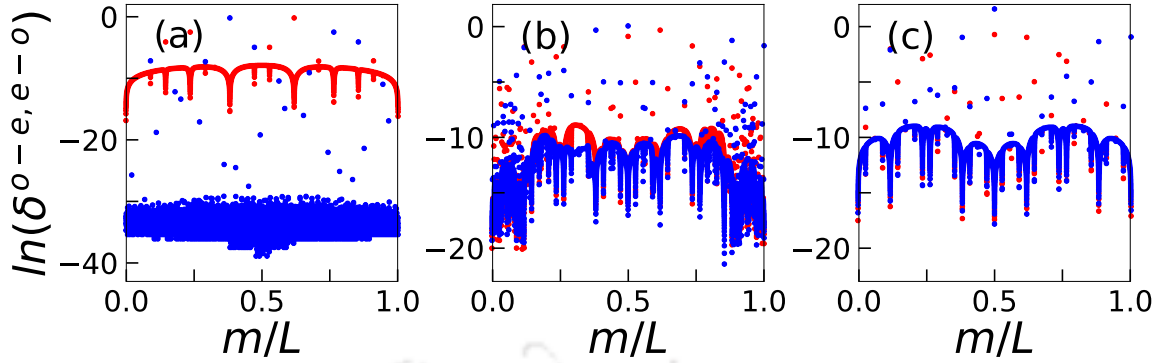


Figure 5.2: Even-odd δ^{e-o} (red) and odd-even δ^{o-e} (blue) for $\lambda = 0.75$ and different values of Δ . For (a) $\Delta = 0.0$, (b) $\Delta = 0.9$ and (c) $\Delta = 3.0$ the system lies in the extended, intermediate and localized phase respectively. The results are obtained for a system of size $L = 28657$ and $\beta = 17711/28657$ under PBC.

With increase in Δ , the system enters into different phases. The behaviour of $\langle \text{IPR} \rangle$ together with $\langle \text{NPR} \rangle$ clearly indicates transitions to the localized phases at three different critical values of Δ such as $\Delta_c \sim 0.7, 1.2, 1.9$ and three intermediate phases emerge (shaded regions). These localization transitions are further complemented by inspecting the behaviour of other parameters of interest such as the Shannon entropy [126–128] and the gap ratio [129, 130]. The Shannon entropy is defined from the single particle states as $S_m = -\sum_i |\psi_m^i|^2 \ln(|\psi_m^i|^2)$ which vanishes for the localized states due to participation from a single site only and approaches its maximum value $\ln(L)$ for the extended states where the wave amplitude is finite for all lattice sites [128]. On the other hand the average value of the gap ratio

$$r_m = \frac{\min(\delta_m, \delta_{m+1})}{\max(\delta_m, \delta_{m+1})} \quad (5.2)$$

where, $\delta_m = E_m - E_{m-1}$ is the difference between two adjacent energies calculated using PBC, is 0 (0.386) in the extended (localized) phases [129, 130]. Here, E_m are the eigenenergies arranged in increasing order. We plot $\langle S \rangle / \ln(L)$ and $\langle r \rangle$ as a function of Δ in Fig. 5.1(c). The Shannon entropy clearly vanishes in the localized phases and remains finite in both the extended and the intermediate phases as expected. On the other hand, $\langle r \rangle$ approaches its maximum value (as predicted by the Poissonian statistics) in the localized phases and decreases in the intermediate phases and becomes vanishingly small in the extended phase. All these quantities together confirm the multiple localization transitions of Fig. 5.1(a).

To further understand the behaviour of $\langle r \rangle$ we compute the even-odd and odd-

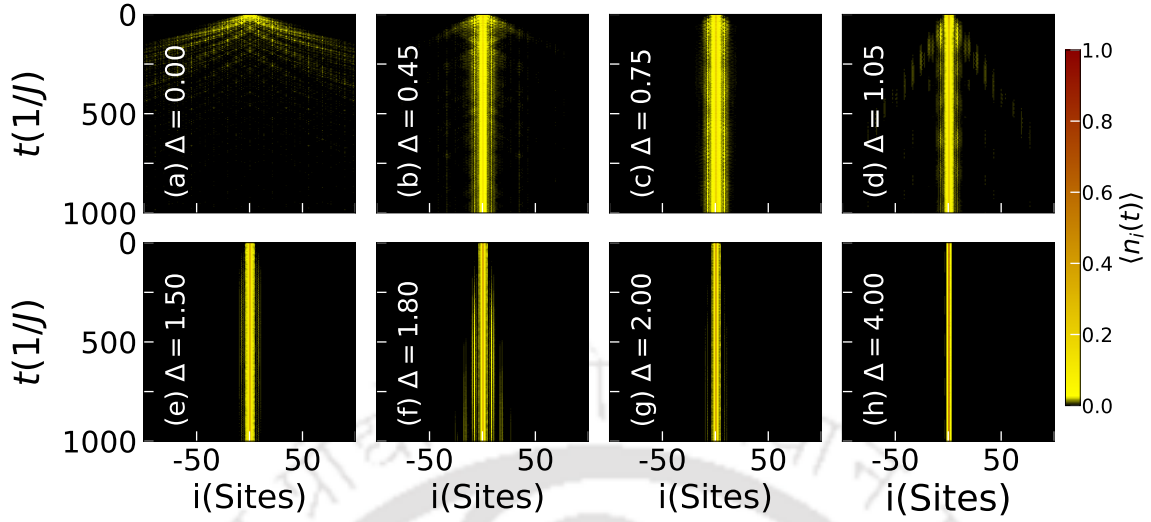


Figure 5.3: The density distribution during the time evolution of an initial state for different values of Δ (a-h) at a fixed $\lambda = 1.5$ and $L = 2584$ with an average over 500 different values of phase offset ϕ . Only central 201 sites are shown for clarity.

even level spacings which are given by [128, 131]

$$\delta^{e-o} = E_{2m} - E_{2m-1} \text{ and } \delta^{o-e} = E_{2m+1} - E_{2m}, \quad (5.3)$$

respectively, that can clearly distinguish between the extended, intermediate and localized phases. In the extended region, due to the presence of doubly degenerate spectrum of the underlying Hamiltonian with no onsite staggered potential, δ^{e-o} vanishes and hence it is well separated from δ^{o-e} as shown in Fig. 5.2 (a). On the other hand, δ^{e-o} and δ^{o-e} have no clear distinction between them for the localized states as the degeneracy is lifted (Fig. 5.2 (c)). However, in the intermediate region (Fig. 5.2 (b)), we see regions of finite and vanishing gap between δ^{e-o} & δ^{o-e} when the states are extended and localized respectively. Therefore, $\langle r \rangle$ attains zero (maximum) value in the extended (localized) regions as $\min(\delta_m, \delta_{m+1})$ vanishes for all m . However, in the intermediate region, it lies in between the two extreme values.

The important inferences which stem out from our analysis so far are as follows. From Fig. 5.1(a) it is clear that in general Δ favours the localization transition. However, for some values of Δ the AA limit of the localization transition is unaffected and the (re)localization transition occurs exactly at $\lambda = \lambda_{AA} = 2$. On the other hand, as a function of Δ , there occurs only one localization transition in the limit of smaller λ . However, for larger λ , the system undergoes multiple localization transitions. While further analysis is necessary to understand the physics behind

these intriguing behaviour of multiple localization transitions and the associated intermediate phases, one possible reason for the multiple localization can be as follows. Due to the two competing onsite potentials such as the disorder and the staggered potential, a situation might favour an overlap of two nearest neighbour states turning a localized state extended [112]. This kind of re-entrant localization of the individual states happens in different parameter domains depending on the energies of the states. Hence, the system as a whole exhibits multiple localization transitions.

5.3.2 Expansion dynamics

In this part we analyse the multiple localization transitions discussed above in the expansion dynamics. Our analysis is based on the standard quenching protocols of unitary time evolution i.e.

$$|\Psi(t)\rangle = e^{-iHt}|\Psi(0)\rangle \quad (5.4)$$

, with the time independent Hamiltonian H given in Eq. 5.1 and an initial state $|\Psi(0)\rangle$ at $t = 0$. For our studies we consider

$$|\Psi(0)\rangle = |\cdot \cdot c_0^\dagger \cdot \cdot\rangle \quad (5.5)$$

, a state corresponding to a particle located at the center of the lattice with open boundary condition. First of all, we track the real space density evolution $\langle n_i(t) \rangle$ computed using the time evolved state $|\Psi(t)\rangle$ as shown in Fig. 5.3(a-h) for different values of $\Delta = 0.0, 0.45, 0.75, 1.05, 1.5, 1.8, 2.0, 4.0$ respectively for a cut through the phase diagram at $\lambda = 1.5$. While the extended and localized phases are characterized by the fast and no spreading of the densities respectively, the intermediate phases are characterised by a bimodal distribution where part of the density remains localized around the central site and a part expands slowly. The bimodal nature of the density profile is due to the presence of both localized and extended states in the intermediate phase. Although this quantity can be observed in experiments [132], to obtain clear signatures of the multiple localization transition we compute the root mean-square displacement defined as

$$\sigma(t) = \left[\sum_i (i - i_0)^2 |\psi_i(t)|^2 \right]^{1/2}, \quad (5.6)$$

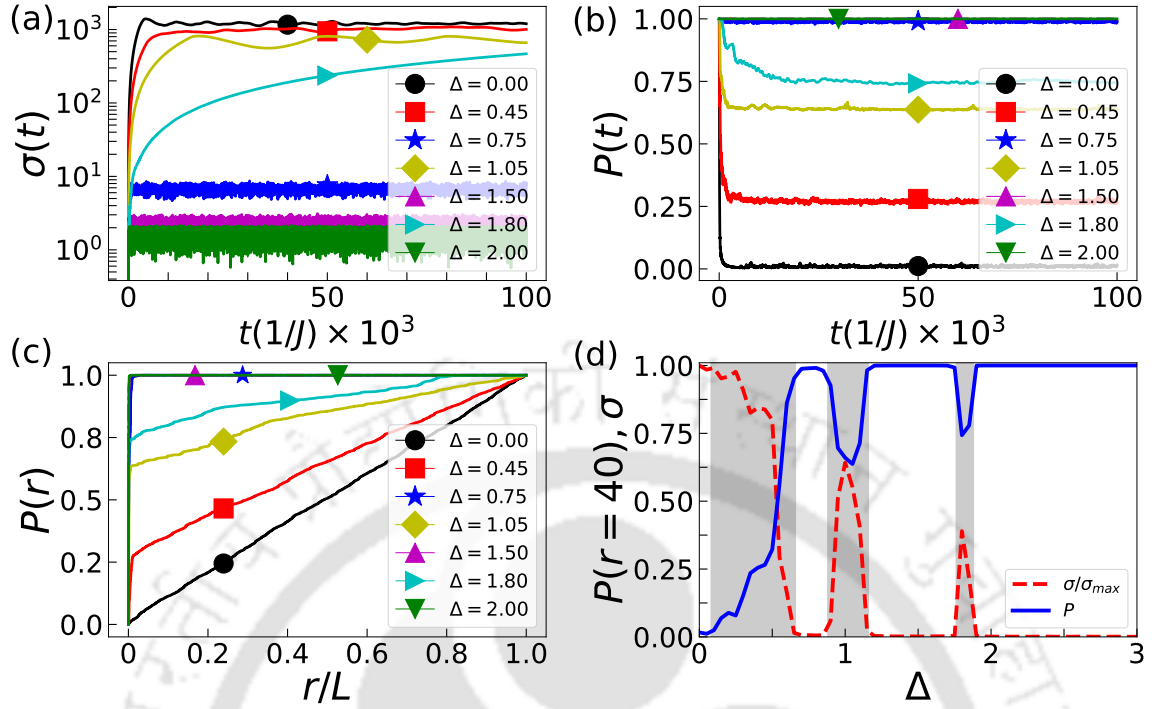


Figure 5.4: (a) $\sigma(t)$ vs t (b) $P_{r=40}(t)$ vs t for $\Delta = 0.0, 0.45, 0.75, 1.05, 1.5, 1.8, 2.0$ and $\lambda = 1.5$. (c) $P_r(t = 10^5(1/J))$ as a function of r/L shows the multiple localization transition (see text). (d) The time evolved values of σ (red dashed) and $P_{r=40}$ (blue solid) to $t = 10^5(1/J)$ are plotted as a function of Δ for $\lambda = 1.5$. The shaded regions indicate the intermediate phases. For all the cases a system size of $L = 4181$ is considered.

where i_0 is the initial position of the particle. This quantity directly corresponds to the expansion of wavepacket and exhibits distinct features in its long time evolution for the extended, intermediate and the localized phases as recently observed in the quantum gas experiments [119].

While a faster (slower) expansion characterizes the extended (intermediate) phases, the localized phases are characterised by no expansion as shown in Fig. 5.4(a). In the figure, the saturation of $\sigma(t)$ to different values after a long time evolution [115, 119] for different $\Delta = 0.0, 0.45, 0.75, 1.05, 1.5, 1.8, 2.0, 4.0$ and $\lambda = 1.5$ clearly indicates the multiple localization transitions.

We also compute the survival probability defined as

$$P_r(t) = \sum_{i=-r/2}^{r/2} |\psi_i(t)|^2 \quad (5.7)$$

which is the probability of finding the particle within a range of sites between $-r/2$ to $r/2$ for small r [131, 133, 134]. For the quenching to the extended phase, due to the

fast expansion of the wavepacket, $P_r(t)$ tends to vanish in the long time evolution. On the other hand for the localized phases, $P_r(t)$ is maximum ($P_r(t) \rightarrow 1$) indicating no spreading. However, in the intermediate phases, due to the finite probability of both escaping and remaining within the small range of r the value of P_r decreases but remains finite. To examine this behaviour we plot $P_{r=40}(t)$ as a function of t in Fig. 5.4(b) for parameters considered in Fig. 5.4(a) and obtain a clear feature of multiple localizations.

Additionally, the multiple localization transitions can also be seen by looking at the behaviour of P_r as a function of r/L for different values of Δ after the long time evolution (Fig. 5.4(c)). As in the extended phase ($\Delta = 0$), the probability of finding the particle at all sites is equal to $1/L$, the P_r varies as r/L depicting an almost straight line. For the localized phases, $P_r \rightarrow 1$ within a short range of r/L as expected. However, for the intermediate phases, $P_r \rightarrow 1$ at different values of r/L for a given time t . The saturation of P_r is dependent upon the localization length; larger the localization length, $P_r \rightarrow 1$ at larger r/L value and vice versa. As Δ increases, the multiple localization features can be clearly seen as the position of $P_r \rightarrow 1$ shifts between the extended and localized limits.

Finally to clearly see the signatures of the multiple localization transitions from the expansion dynamics, we plot the saturated values of $\sigma(t = 10^5(1/J))$ along with $P_r(t = 10^5(1/J))$ as a function Δ for $\lambda = 1.5$ and $L = 4181$. The variation of P_r along with σ clearly shows three localization transitions and three intermediate phases (shaded regions in Fig. 5.4(d)) as already shown in Fig. 5.1(c).

5.3.3 Experimental scheme

In this part we provide a realistic setup to observe the multiple localization transitions predicted above in optical lattice experiments. It should be noted that the lattice model considered here has already been used as a tool to study the localization and topological physics [119–121, 135] in the quantum gas experiments. For the observation of the localization phenomena, a lattice with onsite staggered potential (superlattice) was used to create an initial state for the dynamical evolution and was not part of the final quasiperiodic system. However, in our case the superlattice potential is itself a parameter of the Hamiltonian and moreover, our predictions are based on the dynamics of a single particle initial state. Therefore, we propose a different method where the single particle initial state can be created and the dynamics can be observed.

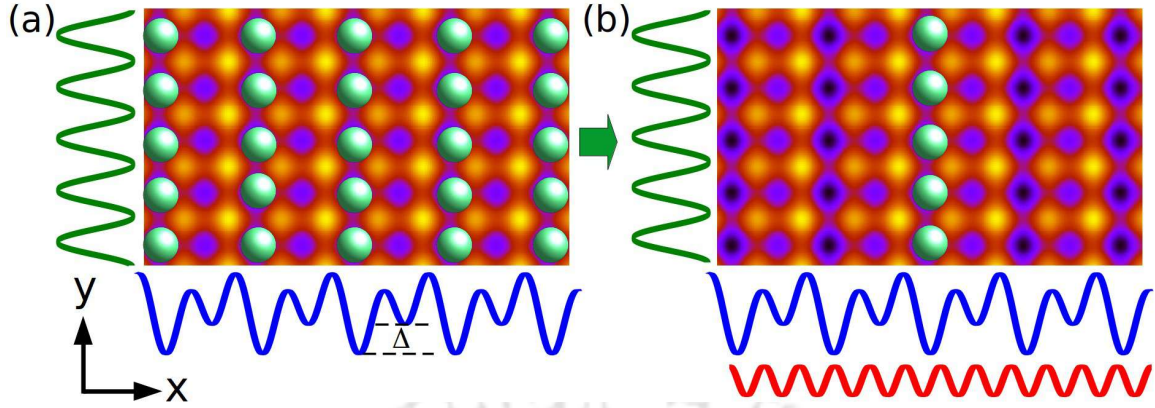


Figure 5.5: Scheme for initial state preparation for the experimental observation of the multiple localization transitions. Deep (light) blue regions are the deep (shallow) lattice sites and the green spheres indicate the atoms. Δ denotes the onsite staggered potential.

Following the prescriptions given in Ref. [119, 135], at first a square lattice can be created with superlattice (normal lattice) along the x - (y -) directions using the equation

$$V(x, y) = V_P \cos^2\left(\frac{2\pi x}{d}\right) + V_L \cos^2\left(\frac{\pi x}{d} - \varphi\right) + V_P \cos^2\left(\frac{2\pi y}{d}\right)$$

where V_P and V_L are the depths of the primary and the long lattices respectively, d is the lattice constant and φ is the phase difference between them. By choosing $V_P \gg V_L$ and $\varphi = \pi/3$ a superlattice relevant for our studies can be created along the x -direction whereas the lattice remains uniform along the y -direction. When loaded with ultracold atoms (spin-polarized fermions or hardcore bosons), an initial stripe phase can be formed where atoms occupy the rows of deep lattice sites along the y - direction (see Fig. 5.5(a)). Further, the atoms can be selectively removed from all the rows except the central row [132] leading to a situation where each individual tube contains only one atom localized at the center as depicted in Fig. 5.5(b). Now by superimposing a disorder lattice of the form $V_D \cos^2(\frac{\pi x}{d_D})$ along the x -direction, the desired initial state can be achieved which can be deep in the localized phase of the phase diagram shown in Fig. 5.1(a). Following an appropriate quenching protocol, the multiple localization transitions can in principle be observed by measuring the above mentioned quantities.

We examine the phase diagram in $\Delta - \lambda$ plane further and extract more information out of it. In Fig. 5.6 we show the expanded version of the phase diagram

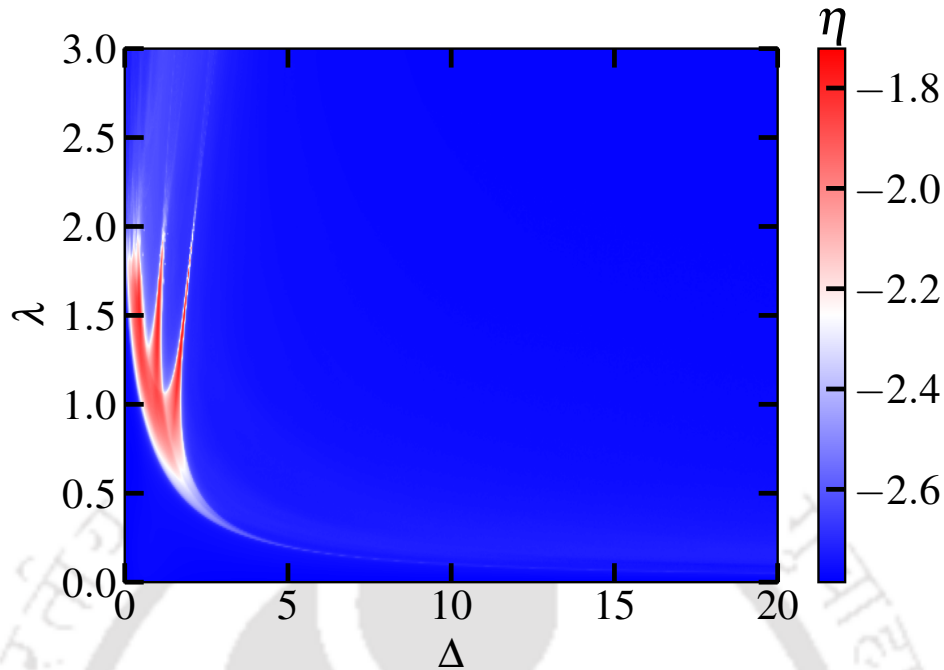


Figure 5.6: The phase diagram in the Δ - λ plane obtained using the values of η for a system of size $L = 610$.

presented in Fig. 5.1(a). We notice that as Δ increases the intermediate phase (marked by red and white regions) becomes narrower and at larger values of Δ , the tail of the intermediate phase approaches to the Δ -axis, indicating a localization for smaller values of λ . Fig. 5.7(b) shows the behaviour of $\langle \text{IPR} \rangle$ and $\langle \text{NPR} \rangle$ as a function of Δ for $\lambda = 0.1$ where the system exhibits a sharp localization transition at $\Delta = 1/\lambda = 10$. The sharp transition is clearly depicted in Fig. 5.7(a) where all the states are extended (localized) before (after) the critical point ($\Delta = 10$). This behaviour is similar to the Aubry-André model which also exhibits a sharp localization transition as a function of λ . From this analogy one can infer that the self-duality which is broken due to the presence of small yet finite Δ , gets restored again for large Δ .

5.4 Conclusions

We have studied the localization transitions in a one-dimensional quasiperiodic lattice of AA type with onsite staggered potential. By analysing various physical quantities such as participation ratios, Shannon entropy and gap ratio we have predicted the scenario of multiple localization transitions in the parameter space. The impor-

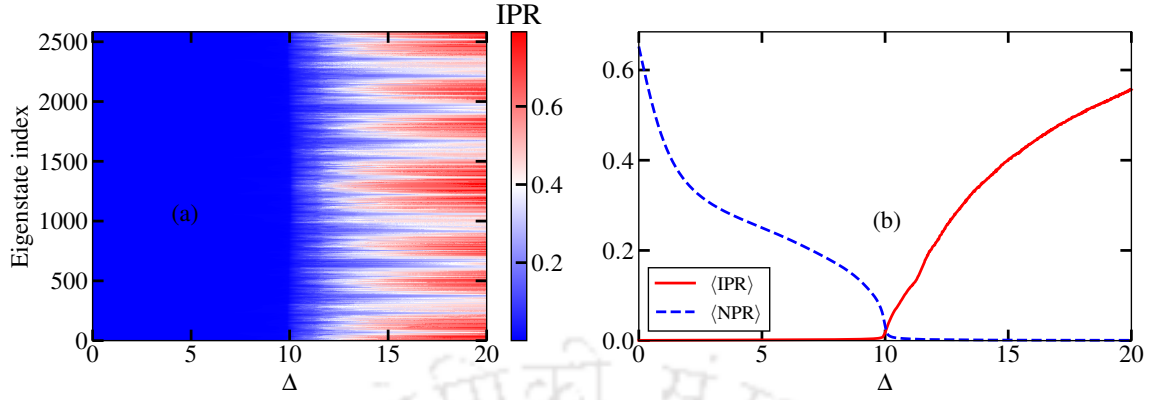


Figure 5.7: (a) IPR as a function of eigenstate index and Δ , (b) $\langle \text{IPR} \rangle$ (red solid line) and $\langle \text{NPR} \rangle$ (blue dashed line) as a function of Δ for $\lambda = 0.1$ with system size $L = 2584$ showing a sharp localization transitions.

tant observation is that for fixed disorder strengths, there exist multiple localization transitions of the system as a function of the staggered potential strength. Interestingly, the number of localization transition as a function of the staggered potential increases with increase in disorder strengths. Apart from this the system undergoes two localization transitions as a function of the disorder strength for different values of the dimerization - a feature similar to Ref. [111]. All the localization transitions are found to occur through intermediate phases hosting both the extended and localized states. We have further analysed these findings in the context of expansion dynamics and proposed a method for observation of the multiple localization transitions in the quantum gas experiments. Finally, we revealed that the localization transition as a function of the staggered potential for vanishingly small disorder is sharp in nature, indicating the restoration of the self-duality of the Aubry-André model.

Chapter 6

Disorder driven topological phase transition

6.1 Introduction

As already mentioned in the Introduction, the topological phases of matter are robust to disorder as long as the energy gap remains open. However, for strong enough disorder, the gap in the system vanishes which erases the topological character in the system [38, 39, 136, 137].

One of the characteristic features of topological phases is the Thouless charge pumping (TCP) which has been introduced in Chapter 3. Thouless charge pumps are the quantum analog of the Archimedes screw pump which facilitate particle transport in a one-dimensional lattice through adiabatic and periodic modulation of some parameters of the system and not by any external gradient or field. In the case of topological phase transitions through gap closing singularities, the TCPs are known to be quantized around a cycle encircling the gap closing point and are related to a topological invariant known as the Chern number defined in the context of quantum Hall physics. On the other hand, the presence of disorder plays a crucial role in stabilizing the TCPs. While the quantization of charge transport remains robust against weak disorder or as long as the bulk gap remains finite, strong disorder leads to a breakdown of the TCP due to the closing of the bulk gap and vanishing of the topological phase [38, 39, 136–138]. In this chapter, however, we propose a one-dimensional model with quasiperiodic disorder which exhibits a disorder mediated Thouless charge pumping. We first show the robustness of TCP as a function of the disorder and mark a disorder-induced topological phase transition through the TCP measures. Moreover, unlike any other existing works which involve the periodic

modulation of hopping terms, we show that a quantized amount of charge transport is also possible as a function of the periodic modulation of the quasiperiodic potential for fixed hopping strengths.

6.2 Model and approach

We consider a one-dimensional (1D) lattice of spinless fermions with N two-site unit cells. The model Hamiltonian including unit cell-wise staggered onsite quasiperiodic disorder then reads as

$$\begin{aligned}
 H = & -t_1 \sum_{j=1}^N \left(c_{j,A}^\dagger c_{j,B} + H.c. \right) - t_2 \sum_{j=1}^{N-1} \left(c_{j+1,A}^\dagger c_{j,B} + H.c. \right) \\
 & + \lambda \sum_{j=1}^N (-1)^{j+1} \cos [2\pi\beta(2j-1) + \phi] n_{j,A} \\
 & + \lambda \sum_{j=1}^N (-1)^{j+1} \cos [2\pi\beta(2j) + \phi] n_{j,B} \\
 & + \Delta \sum_{j=1}^N (n_{j,A} - n_{j,B})
 \end{aligned} \tag{6.1}$$

where $c_{j,A}$ ($c_{j,B}$) is the fermionic annihilation operator at A (B) sublattice site of the j th unit cell. The corresponding onsite number operator is given by $n_{j,A}$ ($n_{j,B}$). While t_1 and t_2 stand for the intra-cell and inter-cell hopping matrix elements respectively, λ fixes the strength of the quasiperiodic disorder which we refer to as disorder in the following. The cell-wise staggered nature of the disorder strength produces a pattern like $\lambda, \lambda, -\lambda, -\lambda, \dots$ throughout the lattice. Thus, we consider lattice sites as the multiple of four in order to have equal number of positive and negative disorder strengths. The last term in the Hamiltonian is a staggered onsite potential term with strength Δ on A sublattice sites and $-\Delta$ on B sublattice sites. A schematic representation of the model is shown in Fig. 6.1. The quasiperiodicity of the lattice is ensured by considering $\beta = (\sqrt{5} - 1)/2$ - the inverse Golden mean and all the numerical simulations are performed under periodic boundary conditions (PBCs), unless otherwise explicitly mentioned. For convenience we define a quantity $\alpha_1 = t_1/t_2$ by fixing $t_2 = 1$, which also sets the energy scale of the system. In our studies we set $\phi = 0$, as the results do not change significantly for finite values of ϕ

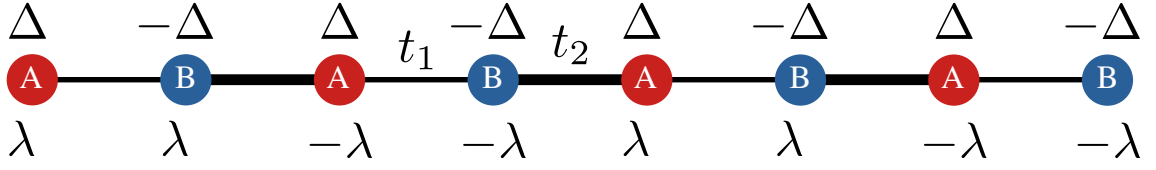


Figure 6.1: The figure depicts the model given in Eq. 6.1 in terms of lattice sites, hopping strengths t_1 and t_2 , staggered onsite potential strength Δ and the quasiperiodic disorder strength λ . The sublattice sites in a unit cell are denoted by A and B .

when the system size is large.

6.3 Results

In the absence of onsite terms ($\lambda = \Delta = 0$) our model reduces to the well known Su-Schrieffer-Heeger (SSH) model which exhibits a phase transition from a trivial insulator (when $t_1 > t_2$) to a topological insulator (when $t_1 < t_2$) via a gap-closing point (at $t_1 = t_2$). The topology of the SSH model is protected by the chiral symmetry which protects two degenerate zero energy edge states lying inside the bulk gap of the topological phase. While this symmetry is robust for any kind of disorder associated to the hopping, it gets broken for a finite onsite or diagonal disorder which lifts the degeneracy of the edge states. The effect of onsite disorder has already been extensively studied in a truly random as well as a quasiperiodic lattice. The key finding in these systems is that although the degeneracy is lifted, the system remains topological as long as the bulk gap is finite and once the gap is closed, there is no possibility of opening up again. However, the opening up of the bulk gap again after its closing was predicted as a function of random dimer disorder in Ref. [139].

In this chapter, we show that for the model under consideration, disorder can actually induce a topological phase transition. Using a modified pumping scheme which involves the periodic modulation of the disorder strength, we show that a robust and quantized Thouless charge pumping can be achieved in the lattice.

We initiate the discussion by capturing the topological properties of the model for vanishing staggered potential, i.e. for $\Delta = 0$. As a first approach we compute the single particle spectral gap G between the two middle eigenstates as a function of α_1 and λ under PBC and plot them in Fig. 6.2 (a). As expected, in the absence of disorder the gap is finite for all values of α_1 except for $\alpha_1 = 1$ which is the gap-closing critical point of the SSH model. Near the $\alpha_1 \sim 0$ region, a direct transition from

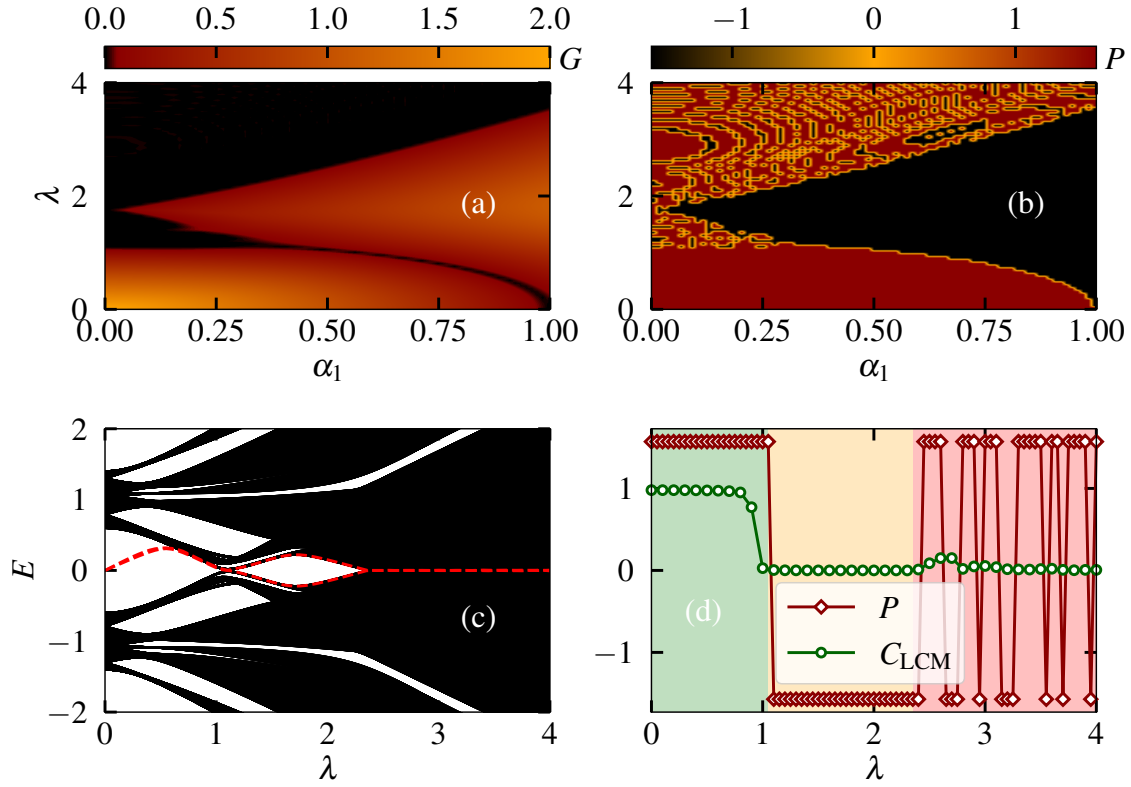


Figure 6.2: Phase diagram in the $\alpha_1 - \lambda$ plane as a function of (a) G and (b) P . (c) shows the energy spectrum, and (d) shows the polarization P and local Chern marker C_{LCM} as a function of λ for a cut through $\alpha_1 = 0.4$. The two red dashed lines in (c) denote the variation of edge states under open boundary conditions. The green, orange and red shaded areas in (d) mark the topological, trivial and gapless phases, respectively. Here the system size is considered to be $L = 400$ for C_{LCM} and $L = 2584$ for other parameters. We set $\Delta = 0$ in all the cases.

a gapped phase to a gapless phase occurs as a function of λ . However, we can see two gapped phases and an intriguing gapped-gapless-gapped-gapless transition for intermediate values of α_1 . For $\alpha_1 = 1$ the system exhibits a gapless-gapped-gapless transition.

The underlying behaviour of the gapped phases depicted in Fig. 6.2(a) cannot be captured from the spectral gap alone. Thus, we compute a quantity called polarization P in the real space which is given by the formula

$$P = \frac{1}{2\pi} \text{Im} \ln \langle \Psi | X^e | \Psi \rangle, \quad (6.2)$$

where $X^e = \exp\left(\frac{2\pi i}{L} \sum_{j=1}^L j n_j\right)$ is the exponentiated position operator with $n_j = n_{j,A}$ or $n_{j,B}$ being the onsite number operator and $|\Psi\rangle$ being the many-body ground

state at half filling. This quantity can be safely considered as a topological invariant since it clearly distinguishes the different phases (see Fig. 6.2(b)). The gapped phase corresponding to smaller (larger) λ takes a fixed value of $P = \pi/2$ ($-\pi/2$). Thus, both these gapped phases seem to be topologically different insulators. On the other hand, P does not take any fixed value in the gapless regions, where the topology is ill-defined.

The behaviour of the spectral gap and edge states can be clearly discerned from the single-particle energy spectrum plotted as a function of λ for a cut through the phase diagram at $\alpha_1 = 0.4$ under open boundary conditions (OBCs). As can be seen from Fig. 6.2(c) a pair of zero energy edge states lie inside the bulk gap for vanishing disorder ($\lambda = 0$). However, any finite disorder makes the edge states energetic and they eventually merge into the bulk states as disorder increases. On the other hand, the bulk exhibits a gapped-gapped phase transition via a gapless critical region. The first gapped phase hosting the edge states can be called as topological insulator whereas the second one without any edge states is just a trivial band insulator. It is important to note that here the edge states are sensitive to the phase ϕ and thus the position of them merging into the bulk may vary for different disorder realizations.

Now we characterize the topological phase transition at $\alpha_1 = 0.4$ by plotting the polarization P (dark red line with diamonds) as a function of λ in Fig. 6.2 (d). This quantity clearly distinguishes the topological phase where it becomes $\pi/2$, and the trivial phase where it becomes $-\pi/2$. At the transition point between these two phases, P exhibits a sharp jump. However, in the gapless regime, P does not have a fix value and we see strong fluctuation as expected.

Another quantity that can mark the topological phase transition is known as the local Chern marker (LCM) which has been proven to be a suitable topological invariant for systems with broken translational symmetries such as the one considered here. Since disorder breaks the translational symmetry of a system, momentum is not a good quantum number, thus, LCM needs to be defined in the real space. Following the prescription given in [38] we first modify the intra-cell and inter-cell hopping amplitudes as $t_1 = J - \nu$ and $t_2 = J + \nu$, respectively, where J is a fixed hopping strength and ν is the dimerization strength. Then we introduce a pumping parameter τ that helps in varying the dimerization and staggered potential periodically as $\nu = \nu_0 \cos(\tau)$ and $\Delta = \Delta_0 \sin(\tau)$, respectively. Now, using a discretized form the LCM can be defined as

$$C(j) = \frac{1}{\pi} \sum_{n=1}^{N_\tau-1} \text{Im} \langle j | X^{e^\dagger} P(\tau_n) X^e Q(\tau_n) P(\tau_{n+1}) P(\tau_n) | j \rangle, \quad (6.3)$$

where P and $Q = \mathbb{1} - P$ are the projection operators onto occupied and unoccupied states of the Hamiltonian H , respectively. Here τ is discretized with a step size $d\tau = \tau_{n+1} - \tau_n$ and N_τ is the number of points. Here the sum $C_{\text{LCM}} = \sum_j C(j)$ gives rise to the Chern number associated to the phase. In Fig. 6.2 (d) we plot C_{LCM} (green line with circles) as a function of λ for $J = 0.7, \nu_0 = 0.3$ and $\Delta_0 = 0.5$ which yields $t_1 = 0.4$ and $t_2 = 1$, implying $\alpha_1 = 0.4$, when $\tau = 0$. As anticipated, the LCM takes quantized values in the insulating phases (1 in topological phase and 0 in trivial phase). However, its value is not quantized in the gapless regimes (for $\lambda > 2.4$).

From the above analysis we observe a well defined topological phase transition as a function of onsite quasiperiodic disorder strength. Such a feature is counter intuitive as strong onsite disorder leads to the overlap of single particle states and thus the emergence of another gapped phase after gap closing is not so trivial. Nonetheless, we utilize this feature and propose a disorder driven Thouless charge pumping.

6.4 Disorder driven Thouless charge pumping (dTCP)

As mentioned in previous chapters, a quantized number of particles can be pumped in a lattice without adding extra terms to the system and this phenomenon is known as Thouless charge pumping. A finite and robust pumping requires two important criteria: (a) the pumping cycle should enclose the gap-closing point of the topological phase transition and (b) the system should remain gapped throughout the pumping cycle. The Rice-Mele (RM) model is helpful in describing a pumping scheme which is just an extended version of the SSH model with an extra staggered onsite potential term. The Hamiltonian presented in Eq. 6.1 in the absence of disorder ($\lambda = 0$) reduces to the RM model. Moreover, it has been revealed that the charge pumping of the RM model is robust for any onsite disorder as long as the bulk gap is open and a breakdown occurs otherwise. Therefore, disorder can be considered as an obstruction for topology as well as for robust charge pumping.

Here we propose an innovative charge pumping scheme led by onsite disorder strength and coin it as a disorder driven topological charge pumping (dTCP). The

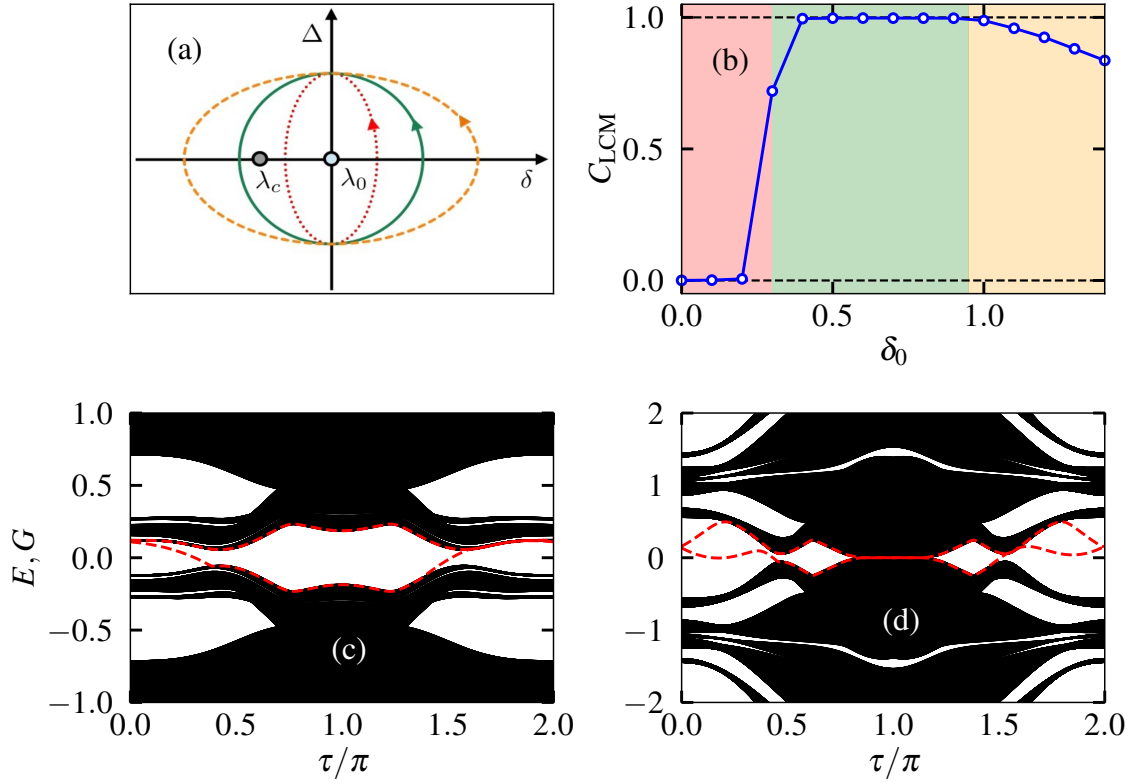


Figure 6.3: (a) shows the pumping scheme in the $\Delta - \delta$ plane corresponding to three different pumping cycles. Here $(\lambda_0, 0)$ is the origin of the cycle and λ_c is the gap closing critical point. (b) shows the variation of local Chern marker C_{LCM} as a function of δ_0 for $\alpha_1 = 0.4, \Delta_0 = 0.5$ and $\lambda_0 = 1.4$. (c) and (d) show the energy spectrum as a function of τ/π for $\delta_0 = 0.5$ and 1.2 , respectively.

scheme involves a periodic modulation of the onsite potentials (disorder and staggered potential) only but with fixed intra-cell and inter-cell hopping strengths, as opposed to any other existing literature so far. The staggered onsite potential helps in keeping the bulk gap open throughout the cycle. The pumping Hamiltonian in our case reads as

$$\begin{aligned}
 H_p = & -t_1 \sum_{j=1}^N \left(c_{j,A}^\dagger c_{j,B} + H.c. \right) - t_2 \sum_{j=1}^{N-1} \left(c_{j+1,A}^\dagger c_{j,B} + H.c. \right) \quad (6.4) \\
 & + (\lambda_0 - \delta) \sum_{j=1}^N (-1)^{j+1} \cos [2\pi\beta(2j-1)] n_{j,A} \\
 & + (\lambda_0 - \delta) \sum_{j=1}^N (-1)^{j+1} \cos [2\pi\beta(2j)] n_{j,B} \\
 & + \Delta \sum_{j=1}^N (n_{j,A} - n_{j,B})
 \end{aligned}$$

where the first two terms are the hopping terms same as in Eq. 6.1. Similarly, the last term is the staggered onsite potential term. However, the disorder strength now becomes $\lambda = \lambda_0 - \delta$ where λ_0 is the origin of the pumping cycle. We now periodically vary δ and Δ as $\delta_0 \cos(\tau)$ and $\Delta_0 \sin(\tau)$, respectively, for $\tau \in (0, 2\pi)$. A pumping scheme based on the dTCP approach is shown in Fig 6.3(a) in the $\delta - \Delta$ plane. Here we mainly consider three distinct pumping cycles; Cycle-1: the cycle does not enclose the gap-closing critical point (λ_c) of the TPT but the gap is open throughout (marked by red dotted line), Cycle-2: the cycle encloses the gap-closing point and the gap also remains open (marked by green solid line), and Cycle-3: the cycle encloses the gap-closing point but the gap is not open throughout the cycle (marked by orange dashed line). In order to compare these three cases and to quantify the pumping we compute the local Chern marker (LCM) using Eq. 6.3. The only difference here compared to the standard approach is that we now fix t_1 and t_2 , and modulate the disorder strength instead.

In Fig. 6.3 (b) we plot C_{LCM} for $(t_1, t_2, \lambda_0, \Delta_0) = (0.4, 1, 1.4, 0.5)$ and for varying δ_0 . As expected, since the pumping path follows the Cycle-1 for $\delta_0 = 0$ to 0.2, C_{LCM} vanishes, indicating no pumping of particle (red shaded area). At $\delta_0 = 0.3$ the pumping cycle passes through the gap-closing point $\lambda_c = 1.1$, hence, C_{LCM} is not quantized. However, in the regime $\lambda_0 = 0.4$ to 0.9, C_{LCM} becomes 1 which signifies a robust, finite and quantized pumping of particles per cycle (green shaded area). From $\delta_0 = 1.0$ onwards, C_{LCM} is finite but not quantized, and takes values between 0 and 1 (orange shaded area).

To have a clear picture on the behaviour of C_{LCM} we plot the energy spectrum for $\delta_0 = 0.5$ and 1.2 as a function of τ in Fig. 6.3(c) and (d), respectively under OBCs. While the bulk spectral gap is open throughout the cycle for the former case, there

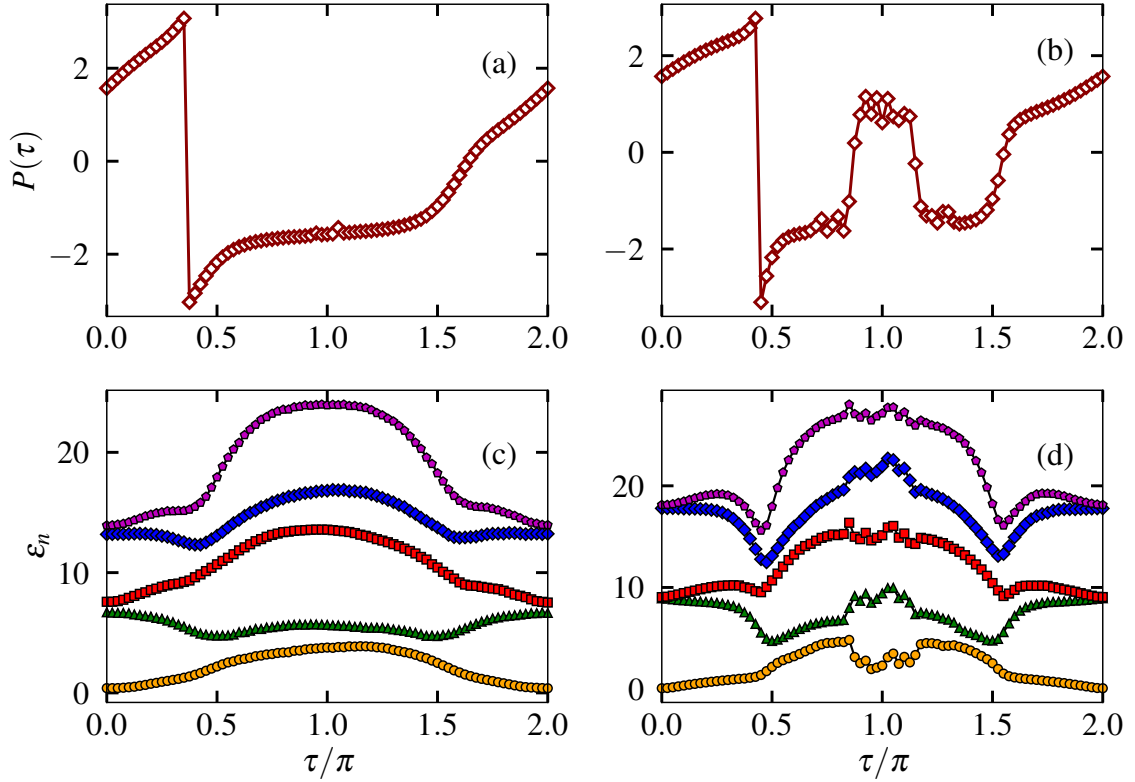


Figure 6.4: Polarization as a function of the pumping parameter τ for (a) $\lambda_0 = 0.5$ and (b) $\lambda_0 = 1.2$. The corresponding entanglement spectra using Eq. 6.8. are shown in (c) and (d), respectively.

exist a few τ values where the gap vanishes for the latter case. Further, we compute the polarization $P(\tau)$ in a pumping cycle for both these cases and compare them in Fig. 6.4(a) and (b). For $\delta_0 = 0.5$, 2π discontinuity in $P(\tau)$ occurs near $\tau = \pi/2$ but it varies smoothly over the cycle. On the other hand for $\delta_0 = 1.2$, apart from the discontinuity at $\tau = \pi/2$, $P(\tau)$ exhibits discontinuities at the gap-closing regime. This is the reason why LCM takes non-quantized value for $\lambda_0 = 1.2$.

The final diagnostic to verify the nature of the charge pumping is the entanglement spectrum of the many-body ground state in the non-interacting limit. We obtain the entanglement spectrum using the following procedure. For a bipartite system of free particles the reduced density matrix of the subsystem A can be derived using the formula

$$\rho_A = \frac{1}{Z} e^{-H_E}, \quad (6.5)$$

where

$$H_E = \sum_{i \in A} f_i^\dagger f_i \quad (6.6)$$

is the entanglement Hamiltonian and Z is the partition function. The eigenvalues of H_E give rise to the entanglement eigenvalues and these can be obtained by diagonalizing the correlation matrix $C_{i,j}$ of a free fermionic system which is given by

$$C_{i,j} = \langle c_i^\dagger c_j \rangle, \quad (6.7)$$

where $i, j \in A$. Now, if ζ_n be the eigenvalues of the correlation matrix then we can calculate the single-particle entanglement spectrum using the formula

$$\epsilon_n = \log \left(\frac{1 - \zeta_n}{\zeta_n} \right). \quad (6.8)$$

Fig. 6.4(c) and (d) depict the entanglement spectrum for $\delta_0 = 0.5$ and 1.2 , respectively where the lowest four eigenvalues of the entanglement Hamiltonian are shown as a function of τ . Similar to the polarization, the eigenvalues show smooth variation throughout the pumping cycle for the first case whereas disconnection between the eigenvalues is observed for the second case.

6.5 Localization properties

At this point we analyze the localization properties of the model under open boundary conditions. First we compute a quantity defined by $\eta = \log_{10}[\langle \text{IPR} \rangle \times \langle \text{NPR} \rangle]$ where $\text{IPR}_n = \sum_{i=1}^L |\psi_n^i|^4$ is the inverse participation ratio of the n th eigenstate $|\psi_n\rangle$ and $\text{NPR}_n = (L \sum_{i=1}^L |\psi_n^i|)^{-1}$ is the corresponding normalized participation ratio. Here $\langle \cdot \rangle$ represents the average over all the eigenstates. In Fig. 6.5 we plot η in $\alpha_1 - \lambda$ plane where the red color represents the intermediate phase and the blue color above(below) it represents the localized(delocalized) phase. At first glance we observe that the delocalized-localized phase transition as a function of λ occurs directly via an intermediate phase for most of the cases. However, along some particular cuts two localization transitions via two intermediate phases are observed. Such

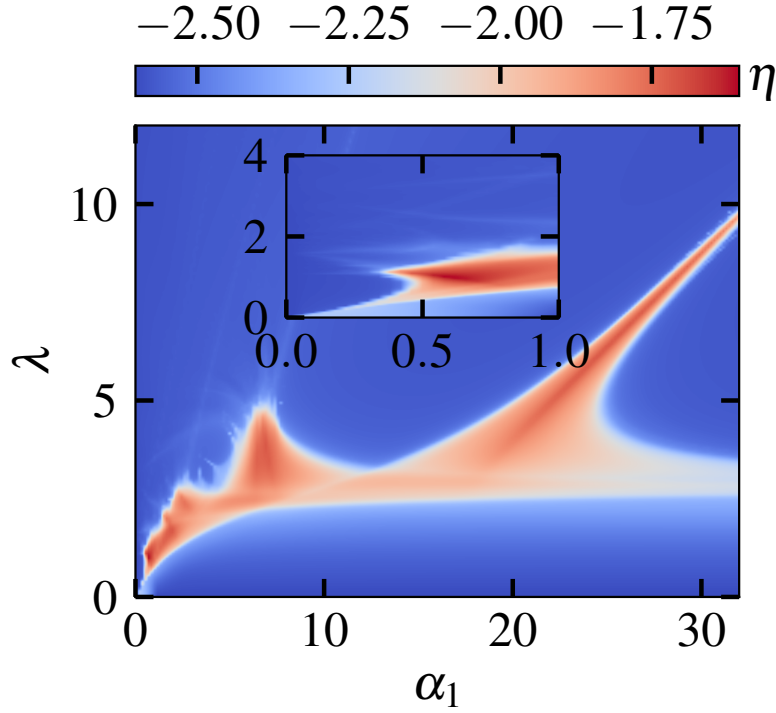


Figure 6.5: Phase diagram in the $\alpha_1 - \lambda$ plane as a function of η . The inset shows a zoomed in portion of the phase diagram.

a transition can be called as a reentrant localization transition. For clear signature we plot the participation ratios for $\alpha_1 = 0.4, 25$ in Fig. 6.6. As expected, $\langle \text{IPR} \rangle$ takes zero(finite) value in delocalized(localized) phase. On the other hand, $\langle \text{IPR} \rangle$ behaves in an opposite manner. However, the transition between them occurs via two intermediate phases where both $\langle \text{IPR} \rangle$ and $\langle \text{NPR} \rangle$ remain finite. The corresponding IPR values for individual eigenstates are plotted in Fig. 6.6 (c) and (d) which clearly indicate that the intermediate phases host both delocalized and localized states together. We also plot another quantity known as the Shannon entropy defined by $S_n = -\sum_i |\psi_n^i|^2 \ln(|\psi_n^i|^2)$ in Fig. 6.6 (a) and (b) for $\alpha_1 = 0.4$ and 25, respectively. For a completely delocalized state S_n approaches its maximum value $\ln(L)$ but vanishes for a localized state. Thus, the average Shannon entropy $\langle S \rangle / \ln(L)$ should yield a value 1(0) in the delocalized(localized) phase and a value lying between 0 and 1 in the intermediate phase. From Fig.6.6 it is evident that Shannon entropy also confirms the existence of reentrant localization transition stemming out of our model.

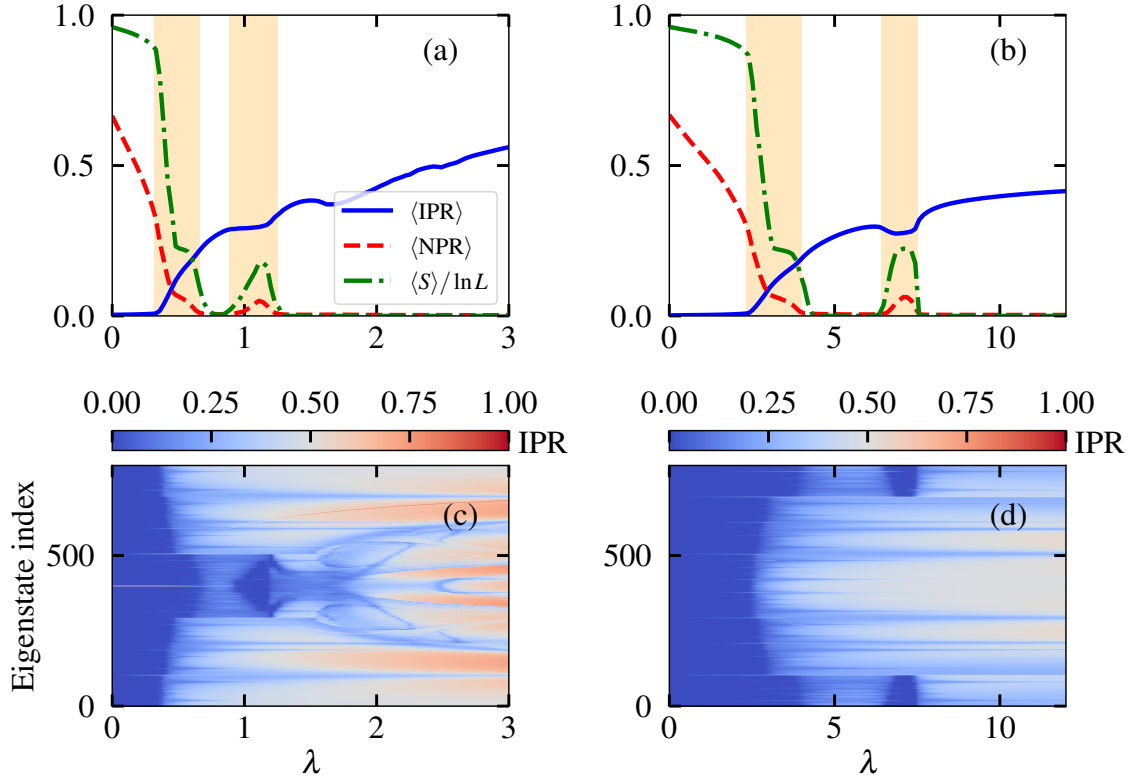


Figure 6.6: $\langle \text{IPR} \rangle$, $\langle \text{IPR} \rangle$ and $\langle S \rangle / \ln L$ as function are shown for $\alpha_1 = 0.4$ in (a) and $\alpha_1 = 25$ in (b). The corresponding IPR values are plotted as function of λ and eigenstate index in (c) and (d), respectively. The orange shaded areas in (a) and (b) denote the intermediate phases.

6.6 Conclusions

In this chapter, we studied the topological and localization properties of the SSH model in presence of a modified quasiperiodic disorder. We first showed that a topological phase with zero energy edge states in the absence of disorder undergoes a transition to a trivial phase via a gap closing point as a function of disorder. To capture this transition and to provide a new approach of topological charge transfer, we proposed a novel pumping scheme which involves the periodic modulation of the disorder strength. Finally, we revealed a reentrant localization transition using the model and showed that the topological and localization transitions do not occur at the same critical point.

Chapter 7

Conclusions and Future Directions

In this thesis, we have analyzed the effects of perturbations like interaction and disorder on the topological character in various one-dimensional models. By using straightforward and sophisticated numerical methods we have proposed some new models while keeping the experimental feasibility of these systems in mind.

In most of the systems exhibiting topological behaviour the root lies in their non-interacting counterpart which can be described via single particle physics. Here we started our discussion in the Chapter 3 with dimerized nearest neighbour interactions between hardcore bosons at half-filling and revealed an interaction induced topological phase transition as a function of the dimerized nearest neighbour interaction. Then we considered a two-component system whose first component is subjected to a two-period superlattice and showed that the second component exhibits topological character due to the hopping term which depends on the density of the first one.

In Chapter 4 we considered a quasi one-dimensional system of a two-leg SSH ladder whose legs are coupled via hopping and interaction. Our single particle and many-body analyses revealed that when the hopping dimerization in both the legs is uniform, i.e. when both of them are topological, there is no topological phase transition as a function of the inter-leg hopping. However, when the dimerization pattern is staggered such that one leg is topological and the other is trivial, there is a proper topological phase transition. Moreover, we found that interaction also drives a topological phase transition. We showed that an attractive (a repulsive) inter-leg interaction leads to a larger (smaller) critical point of transition.

In Chapter 5 we considered a quasiperiodic Aubry-Andre model and introduced a staggered onsite potential and predicted a phenomenon of multiple localization transitions. We showed that the system undergoes localization transitions via in-

intermediate phases as a function of both the disorder strength as well the staggered potential when either of the two is fixed. Further, we proposed an experimental scheme to observe such an intriguing localization transition behaviour in optical lattices. We also noticed that in the large staggered potential limit or vanishingly small disorder limit the transition no longer occurs through intermediate phases, rather it becomes sharp like the one in the case of the Aubry-André model.

Finally, in Chapter 6 we examined the effect of a particular type of quasiperiodic disorder on the topological character exhibited by the SSH model. Starting from the topological regime we observed a gapped-gapped phase transition as a function of the disorder strength. This motivated us to propose a novel Thouless charge pumping scheme involving the periodic modulation of the disorder strength and a staggered onsite potential. Our approach successfully shows quantized and robust charge pumping if there is no gap closing point in the pumping path and the gap closing point lies inside the pumping cycle. Similar to the previous chapter here also we observe multiple localization transitions.

7.1 Future Directions

The topics discussed in this thesis involves some of the timely and important areas of research in condensed matter. The results presented are novel and promise to be helpful in understanding topological and localization physics in the context of low dimensional systems. The simplicity of some of the models makes them experimentally realizable using various artificial systems. On the other hand, a few models which although look complicated, provide new insights into the topological and localization properties in general. Our work opens up the possibility to study other related systems which may lead to interesting scenarios. In the following we mention a few of them.

The interaction induced topological phase transition in one dimensional lattice can be explored in the presence of further near-neighbour interaction or hopping. For example, the interplay between topology and kinetic frustration can be studied in detail. The two-leg SSH ladder in the presence of both inter and intral leg interaction can also be explored where one can expect a much richer paradigm of interaction induced topological phase transitions. Moreover, one may also think of going to densities away from half filling where signatures of topological phase transition is also expected. Going beyond, it is also important to explore the novel scenarios that emerges from the Thouless charge pumping in such systems which

are accessible in the recent experiments. On the other hand, the studies based on quasiperiodic disorder also opens up various new possibilities. The phenomenon of multiple-reentrant localization transition can be explored in higher dimensional lattices. One can in principle consider a model that exhibits a topological character and try to study the fate of these re-entrant localization in the single particle regime as well as in two dimension. An important extension could be the exploration for many-body re-entrant localization transition. Along this line, one may look for the fate of the disorder assisted Thouless pumping in the presence of interaction.





Bibliography

- [1] S. Mondal, S. Greschner, and T. Mishra, Phys. Rev. A **100**, 013627 (2019).
- [2] A. Hayashi, S. Mondal, T. Mishra, and B. P. Das, Phys. Rev. A **106**, 013313 (2022).
- [3] S. Mondal and T. Mishra, Phys. Rev. A **101**, 052341 (2020).
- [4] S. Ejima, F. Lange, and H. Fehske, Phys. Rev. Lett. **113**, 020401 (2014).
- [5] X. Li and S. Das Sarma, Phys. Rev. B **101**, 064203 (2020).
- [6] S. Sachdev, *Quantum Phase Transitions*, Cambridge University Press, 2 edition, 2011.
- [7] K. v. Klitzing, G. Dorda, and M. Pepper, Phys. Rev. Lett. **45**, 494 (1980).
- [8] M. Z. Hasan and C. L. Kane, Rev. Mod. Phys. **82**, 3045 (2010).
- [9] M. Z. Hasan and C. L. Kane, Rev. Mod. Phys. **82**, 3045 (2010).
- [10] W. P. Su, J. R. Schrieffer, and A. J. Heeger, Phys. Rev. Lett. **42**, 1698 (1979).
- [11] A. J. Heeger, S. Kivelson, J. R. Schrieffer, and W. P. Su, Rev. Mod. Phys. **60**, 781 (1988).
- [12] J. K. Asbóth, L. Oroszlány, and A. Pályi, *The Su-Schrieffer-Heeger (SSH) Model*, pages 1–22, Springer International Publishing, Cham, 2016.
- [13] F. Grusdt, M. Hönig, and M. Fleischhauer, Phys. Rev. Lett. **110**, 260405 (2013).
- [14] E. G. Dalla Torre, E. Berg, and E. Altman, Phys. Rev. Lett. **97**, 260401 (2006).
- [15] P. W. Anderson, Phys. Rev. **109**, 1492 (1958).
- [16] S. Aubry and G. André, Ann. Israel Phys. Soc. **3**, 18 (1980).
- [17] J. Li, R.-L. Chu, J. K. Jain, and S.-Q. Shen, Phys. Rev. Lett. **102**, 136806 (2009).
- [18] C. W. Groth, M. Wimmer, A. R. Akhmerov, J. Tworzydło, and C. W. J. Beenakker, Physical Review Letters **103** (2009).
- [19] H. Jiang, L. Wang, Q.-f. Sun, and X. C. Xie, Phys. Rev. B **80**, 165316 (2009).
- [20] C.-Z. Chen, J. Song, H. Jiang, Q.-f. Sun, Z. Wang, and X. C. Xie, Phys. Rev. Lett. **115**, 246603 (2015).
- [21] H.-M. Guo, G. Rosenberg, G. Refael, and M. Franz, Phys. Rev. Lett. **105**, 216601 (2010).
- [22] A. Altland, D. Bagrets, L. Fritz, A. Kamenev, and H. Schmiedt, Phys. Rev. Lett. **112**, 206602 (2014).
- [23] I. Mondragon-Shem, T. L. Hughes, J. Song, and E. Prodan, Phys. Rev. Lett. **113**, 046802 (2014).
- [24] P. Titum, N. H. Lindner, M. C. Rechtsman, and G. Refael, Phys. Rev. Lett. **114**, 056801 (2015).

BIBLIOGRAPHY

- [25] P. V. Sriluckshmy, K. Saha, and R. Moessner, *Phys. Rev. B* **97**, 024204 (2018).
- [26] R. Chen, D.-H. Xu, and B. Zhou, *Phys. Rev. B* **100**, 115311 (2019).
- [27] Q. Lin, T. Li, L. Xiao, K. Wang, W. Yi, and P. Xue, *Nature Communications* **13** (2022).
- [28] H. Wu and J.-H. An, *Phys. Rev. B* **102**, 041119 (2020).
- [29] X. S. Wang, A. Brataas, and R. E. Troncoso, *Phys. Rev. Lett.* **125**, 217202 (2020).
- [30] G.-Q. Zhang, L.-Z. Tang, L.-F. Zhang, D.-W. Zhang, and S.-L. Zhu, *Phys. Rev. B* **104**, L161118 (2021).
- [31] K. Li, J.-H. Wang, Y.-B. Yang, and Y. Xu, *Phys. Rev. Lett.* **127**, 263004 (2021).
- [32] C.-A. Li, B. Fu, Z.-A. Hu, J. Li, and S.-Q. Shen, *Phys. Rev. Lett.* **125**, 166801 (2020).
- [33] Y.-B. Yang, K. Li, L.-M. Duan, and Y. Xu, *Phys. Rev. B* **103**, 085408 (2021).
- [34] W. Zhang, D. Zou, Q. Pei, W. He, J. Bao, H. Sun, and X. Zhang, *Phys. Rev. Lett.* **126**, 146802 (2021).
- [35] E. J. Meier, F. A. An, A. Dauphin, M. Maffei, P. Massignan, T. L. Hughes, and B. Gadway, *Science* **362**, 929 (2018).
- [36] S. Stützer et al., *Nature* **560**, 461 (2018).
- [37] G.-G. Liu et al., *Phys. Rev. Lett.* **125**, 133603 (2020).
- [38] A. L. C. Hayward, E. Bertok, U. Schneider, and F. Heidrich-Meisner, *Phys. Rev. A* **103**, 043310 (2021).
- [39] S. Nakajima, N. Takei, K. Sakuma, Y. Kuno, P. Marra, and Y. Takahashi, *Nature Physics* **17**, 844 (2021).
- [40] U. Schollwöck, *Annals of Physics* **326**, 96 (2011).
- [41] K. G. Wilson, *Rev. Mod. Phys.* **47**, 773 (1975).
- [42] U. Schollwöck, *Rev. Mod. Phys.* **77**, 259 (2005).
- [43] S. R. White, *Phys. Rev. Lett.* **69**, 2863 (1992).
- [44] X.-L. Qi and S.-C. Zhang, *Rev. Mod. Phys.* **83**, 1057 (2011).
- [45] E. Dennis, A. Kitaev, A. Landahl, and J. Preskill, *Journal of Mathematical Physics* **43**, 4452 (2002).
- [46] D. Pesin and A. H. MacDonald, *Nature Materials* **11**, 409 (2012).
- [47] I. Vobornik et al., *Nano Letters* **11**, 4079 (2011).
- [48] M. Liu et al., *Opt. Lett.* **40**, 4767 (2015).
- [49] J. Alicea, Y. Oreg, G. Refael, F. von Oppen, and M. P. A. Fisher, *Nature Physics* **7**, 412 (2011).
- [50] S. Rachel, *Reports on Progress in Physics* **81**, 116501 (2018).
- [51] T. Senthil, *Annual Review of Condensed Matter Physics* **6**, 299 (2015).
- [52] S. Nascimbène, Y.-A. Chen, M. Atala, M. Aidelsburger, S. Trotzky, B. Paredes, and I. Bloch, *Phys. Rev. Lett.* **108**, 205301 (2012).
- [53] S. Nakajima et al., *Nature Physics* **12**, 296 (2016).
- [54] M. Lohse, C. Schweizer, O. Zilberberg, M. Aidelsburger, and I. Bloch, *Nature Physics* **12**, 350 (2016).
- [55] S. Mukherjee, A. Spracklen, M. Valiente, E. Andersson, P. Öhberg, N. Goldman,

- and R. R. Thomson, *Nature Communications* **8**, 13918 (2017).
- [56] N. Goldman, J. Dalibard, A. Dauphin, F. Gerbier, M. Lewenstein, P. Zoller, and I. B. Spielman, *Proceedings of the National Academy of Sciences* **110**, 6736 (2013).
- [57] F. Cardano et al., *Nature Communications* **8**, 15516 (2017).
- [58] S. de Léséleuc et al., *Science* **365**, 775 (2019).
- [59] P. Sompet et al., (2021).
- [60] T. Mishra, J. Carrasquilla, and M. Rigol, *Phys. Rev. B* **84**, 115135 (2011).
- [61] T. Fukui and Y. Hatsugai, *Journal of the Physical Society of Japan* **84**, 043703 (2015).
- [62] Y. Hatsugai, *Journal of the Physical Society of Japan* **75**, 123601 (2006).
- [63] M. den Nijs and K. Rommelse, *Phys. Rev. B* **40**, 4709 (1989).
- [64] H. Tasaki, *Phys. Rev. Lett.* **66**, 798 (1991).
- [65] K. Hida, *Phys. Rev. B* **45**, 2207 (1992).
- [66] D. J. Thouless, *Phys. Rev. B* **27**, 6083 (1983).
- [67] Y. Kuno and Y. Hatsugai, *Phys. Rev. B* **104**, 125146 (2021).
- [68] Y. Kuno and Y. Hatsugai, *Phys. Rev. Research* **2**, 042024 (2020).
- [69] A. Hayward, C. Schweizer, M. Lohse, M. Aidelsburger, and F. Heidrich-Meisner, *arXiv preprint arXiv:1810.07043* (2018).
- [70] J. K. Asbóth, L. Oroszlány, and A. Pályi, *The Su-Schrieffer-Heeger (SSH) Model*, pages 1–22, Springer International Publishing, Cham, 2016.
- [71] N. Batra and G. Sheet, *Resonance* **25**, 765 (2020).
- [72] M. Nakagawa, T. Yoshida, R. Peters, and N. Kawakami, *arXiv preprint arXiv:1802.09780* (2018).
- [73] F. Grusdt, M. Hönig, and M. Fleischhauer, *Phys. Rev. Lett.* **110**, 260405 (2013).
- [74] D. Wang, S. Xu, Y. Wang, and C. Wu, *Phys. Rev. B* **91**, 115118 (2015).
- [75] L. Barbiero, L. Santos, and N. Goldman, *Phys. Rev. B* **97**, 201115 (2018).
- [76] B. Sbierski and C. Karrasch, *Phys. Rev. B* **98**, 165101 (2018).
- [77] G. Magnifico, D. Vodola, E. Ercolessi, S. P. Kumar, M. Müller, and A. Bermudez, *Phys. Rev. D* **99**, 014503 (2019).
- [78] J. Sirker, M. Maiti, N. P. Konstantinidis, and N. Sedlmayr, *Journal of Statistical Mechanics: Theory and Experiment* **2014**, P10032 (2014).
- [79] T. Jin, P. Ruggiero, and T. Giamarchi, *Phys. Rev. B* **107**, L201111 (2023).
- [80] A. M. Marques and R. G. Dias, *Phys. Rev. B* **95**, 115443 (2017).
- [81] X.-L. Yu, L. Jiang, Y.-M. Quan, T. Wu, Y. Chen, L.-J. Zou, and J. Wu, *Phys. Rev. B* **101**, 045422 (2020).
- [82] M. Yahyavi, L. Saleem, and B. Hetényi, *Journal of Physics: Condensed Matter* **30**, 445602 (2018).
- [83] S. Mondal, A. Padhan, and T. Mishra, *Phys. Rev. B* **106**, L201106 (2022).
- [84] F. D. M. Haldane, *Phys. Rev. Lett.* **50**, 1153 (1983).
- [85] C. Li, S. Lin, G. Zhang, and Z. Song, *Phys. Rev. B* **96**, 125418 (2017).
- [86] S. Cheon, T.-H. Kim, S.-H. Lee, and H. W. Yeom, *Science* **350**, 182 (2015).
- [87] X. Li, E. Zhao, and W. Vincent Liu, *Nature Communications* **4**, 1523 (2013).

BIBLIOGRAPHY

- [88] K. Padavić, S. S. Hegde, W. DeGottardi, and S. Vishveshwara, *Phys. Rev. B* **98**, 024205 (2018).
- [89] S. Santra, A. Agarwala, and S. Bhattacharjee, *Phys. Rev. B* **103**, 195134 (2021).
- [90] D. Bercioux, O. Dutta, and E. Rico, *Annalen der Physik* **529**, 1600262 (2017).
- [91] P. Matveeva, T. Hewitt, D. Liu, K. Reddy, D. Gutman, and S. T. Carr, *Phys. Rev. B* **107**, 075422 (2023).
- [92] K. Qian, D. J. Apigo, K. Padavić, K. H. Ahn, S. Vishveshwara, and C. Prodan, *Phys. Rev. Res.* **5**, L012012 (2023).
- [93] A. A. Nersesyan, *Phys. Rev. B* **102**, 045108 (2020).
- [94] S.-L. Zhang and Q. Zhou, *Phys. Rev. A* **95**, 061601 (2017).
- [95] F. m. c. Crépin, N. Laflorencie, G. Roux, and P. Simon, *Phys. Rev. B* **84**, 054517 (2011).
- [96] D. Thouless, *Phys. Rev. B* **27**, 6083 (1983).
- [97] R. Citro and M. Aidelsburger, *Nature Reviews Physics* **5**, 87 (2023).
- [98] C. Schweizer, M. Lohse, R. Citro, and I. Bloch, *Phys. Rev. Lett.* **117**, 170405 (2016).
- [99] Y. E. Kraus, Y. Lahini, Z. Ringel, M. Verbin, and O. Zeitler, *Phys. Rev. Lett.* **109**, 106402 (2012).
- [100] L. Taddia, E. Cornfeld, D. Rossini, L. Mazza, E. Sela, and R. Fazio, *Phys. Rev. Lett.* **118**, 230402 (2017).
- [101] A.-S. Walter et al., (2022).
- [102] L. Wang, M. Troyer, and X. Dai, *Phys. Rev. Lett.* **111**, 026802 (2013).
- [103] M. Rice and E. Mele, *Phys. Rev. Lett.* **49**, 1455 (1982).
- [104] J. K. Asbóth, L. Oroszlány, and A. Pályi, *Adiabatic Charge Pumping, Rice-Mele Model*, pages 55–68, Springer International Publishing, Cham, 2016.
- [105] S. Mondal, S. Greschner, L. Santos, and T. Mishra, *Phys. Rev. A* **104**, 013315 (2021).
- [106] G. Karakonstantakis, E. Berg, S. R. White, and S. A. Kivelson, *Phys. Rev. B* **83**, 054508 (2011).
- [107] E. Bertok, F. Heidrich-Meisner, and A. A. Aligia, *Phys. Rev. B* **106**, 045141 (2022).
- [108] S. Mondal, E. Bertok, and F. Heidrich-Meisner, *Phys. Rev. B* **106**, 235118 (2022).
- [109] Y.-T. Lin, D. M. Kennes, M. Pletyukhov, C. S. Weber, H. Schoeller, and V. Meden, *Phys. Rev. B* **102**, 085122 (2020).
- [110] Y. Kuno and Y. Hatsugai, *Phys. Rev. Res.* **2**, 042024 (2020).
- [111] S. Roy, T. Mishra, B. Tanatar, and S. Basu, *Phys. Rev. Lett.* **126**, 106803 (2021).
- [112] V. Goblot et al., *Nature Physics* **16**, 832 (2020).
- [113] M. Kohmoto, L. P. Kadanoff, and C. Tang, *Phys. Rev. Lett.* **50**, 1870 (1983).
- [114] S. Ostlund, R. Pandit, D. Rand, H. J. Schellnhuber, and E. D. Siggia, *Phys. Rev. Lett.* **50**, 1873 (1983).
- [115] G. A. Domínguez-Castro and R. Paredes, *European Journal of Physics* **40**, 045403 (2019).
- [116] G. Modugno, *Reports on Progress in Physics* **73**, 102401 (2010).
- [117] X. Li, X. Li, and S. Das Sarma, *Phys. Rev. B* **96**, 085119 (2017).

- [118] Y. Wang, X. Xia, Y. Wang, Z. Zheng, and X.-J. Liu, *Phys. Rev. B* **103**, 174205 (2021).
- [119] H. P. Lüschen et al., *Phys. Rev. Lett.* **120**, 160404 (2018).
- [120] M. Schreiber et al., *Science* **349**, 842 (2015).
- [121] P. Bordia, H. P. Lüschen, S. S. Hodgman, M. Schreiber, I. Bloch, and U. Schneider, *Phys. Rev. Lett.* **116**, 140401 (2016).
- [122] R. Ramakumar, A. Das, and S. Sil, *Physica A: Statistical Mechanics and its Applications* **436**, 814 (2015).
- [123] E. Maciá, *ISRN Condensed Matter Physics* **2014**, 165943 (2014).
- [124] J. Biddle and S. Das Sarma, *Phys. Rev. Lett.* **104**, 070601 (2010).
- [125] S. Ganeshan, J. H. Pixley, and S. Das Sarma, *Phys. Rev. Lett.* **114**, 146601 (2015).
- [126] L. F. Santos and M. Rigol, *Phys. Rev. E* **82**, 031130 (2010).
- [127] L. F. Santos and M. Rigol, *Phys. Rev. E* **81**, 036206 (2010).
- [128] M. Sarkar, R. Ghosh, A. Sen, and K. Sengupta, *Phys. Rev. B* **103**, 184309 (2021).
- [129] D.-L. Deng, S. Ganeshan, X. Li, R. Modak, S. Mukerjee, and J. H. Pixley, *Annalen der Physik* **529**, 1600399 (2017).
- [130] S. Ray, M. Pandey, A. Ghosh, and S. Sinha, *New Journal of Physics* **18**, 013013 (2015).
- [131] X. Deng, S. Ray, S. Sinha, G. V. Shlyapnikov, and L. Santos, *Phys. Rev. Lett.* **123**, 025301 (2019).
- [132] P. M. Preiss et al., *Science* **347**, 1229 (2015).
- [133] E. J. Torres-Herrera, A. M. García-García, and L. F. Santos, *Phys. Rev. B* **97**, 060303 (2018).
- [134] Z. Xu, H. Huangfu, Y. Zhang, and S. Chen, *New Journal of Physics* **22**, 013036 (2020).
- [135] H. Hara, H. Konishi, S. Nakajima, Y. Takasu, and Y. Takahashi, *Journal of the Physical Society of Japan* **83**, 014003 (2014).
- [136] J. Qin and H. Guo, *Physics Letters A* **380**, 2317 (2016).
- [137] A. Cerjan, M. Wang, S. Huang, K. P. Chen, and M. C. Rechtsman, *Light: Science & Applications* **9**, 178 (2020).
- [138] M. M. Wauters, A. Russomanno, R. Citro, G. E. Santoro, and L. Privitera, *Phys. Rev. Lett.* **123**, 266601 (2019).
- [139] Z.-W. Zuo and D. Kang, *Phys. Rev. A* **106**, 013305 (2022).

Curriculum Vitae

Address

Home Address : Kharmunda, Bijepur, Bargarh, Odisha, India, 768032

Phone : +91 8638445581

Email : apadhan@iitg.ac.in

Personal profile

Date of Birth : 22/05/1996

Address : Kharmunda, Bijepur, Bargarh, Odisha, India, 768032

Gender : Male

Marital Status : Unmarried

Nationality : Indian

Language : Sambalpuri, Odia, English, Hindi

Education

B.Sc (2013-2016) : Panchayat College Bargarh, Sambalpur University

M.Sc (2016-2018) : Central University of Punjab Bathinda

Ph.D (Enrolled in 2019) : Indian Institute of Technology Guwahati

Earned the Senior Research Fellowship in 2021 by Indian Institute of Technology Guwahati.

Qualified Graduate Aptitude Test in Engineering (GATE) in 2019.

Qualified National Eligibility Test (NET) in 2019 (UGC Fellow).